Università degli Studi di Roma
"Tor Vergata"

Facoltà di Scienze
Dipartimento di Fisica

Detection of muons in the LHCb experiment: the aging of RPC detectors and the study of $Z^0 \to \mu^+\mu^-$

Doctoral Thesis in Physics

Danilo Domenici

Tutor

Prof. Giovanni Carboni

Coordinator

Prof. Piergiorgio Picozza

Roma, 2003

“Nati non foste per viver come bruti,
ma per seguir virtute e conoscenza”

Dante, Inferno, canto XXVI, vv. 119-120

“Genius is one percent inspiration,
ninety-nine percent perspiration”

Thomas Alva Edison

Abstract

The LHCb experiment will take place at the future LHC accelerator at CERN and will start in 2007. It is a single arm spectrometer dedicated to precision measurements of CP violation and rare decays in the b quark sector. Recent experimental results have shown that CP violation is large in this sector.

LHCb is designed with a robust and flexible trigger, in order to extensively gain access to a wide spread of different physical processes involving the *beauty* particles. This will allow to over-constrain the Standard Model predictions about CP violation, and to discover any possible inconsistency, which would reveal the presence of "New Physics".

The work presented in this thesis has two main parts: the development of the Resistive Plate Chambers, proposed for the detection of muons in LHCb, and the study of the detector performances in the physical channel $Z^0 \rightarrow \mu^+\mu^-$.

The LHCb experiment has finished its R&D at the end of 2002. We have participated in the development of a suitable detector for the outer part of the Muon system. Because of the large surface to cover (more than 200 m^2) and the high time resolution requested for triggering, the Resistive Plate Chambers (RPC) appeared to represent a valid technology, and their industrial implemented production would have allowed to reduce the costs. The efforts have then been concentrated on the aging effects, to verify that the RPC detectors are able to satisfy the LHCb requirements for a period of ten years working. The results of a comprehensive aging test carried through three years are presented in the first part of the thesis. As we shall see the detectors have showed important aging effects and have been abandoned.

The design values of the center-of-mass energy and luminosity at LHC represent new limits, never reached by hadron colliders. As a result, high production cross-sections will be attained and high statistics data samples are foreseen to be collected, for a large variety of processes.

In the second part of the thesis is reported a complete study of the the process $pp \rightarrow Z^0 \rightarrow \mu^+\mu^-$, a marginal channel respect to main LHCb physics program. However it has recently gained interest, since its the theoretical cross-section has been determined with a good accuracy. New physics results can thus arise from the comparison of the predicted value and a precise experimental measurement. A

particular focus has been put on the detection performances of LHCb, and on off-line and on-line event selections. Three possible physics fields of interest have been individuated and discussed: the application as an absolute luminosity monitor, the efficacy in a precise calibration of the LHCb spectrometer, and the study of the proton structure functions.

Contents

Part I

Detector studies

Chapter 1

The LHCb experiment at LHC

1.1 The Large Hadron Collider

The Large Hadron Collider (LHC) is a 27 km circumference high luminosity proton-proton collider with a center-of-mass energy of $\sqrt{s}$= 14 TeV.

The change of technology from LEP to LHC is necessary because energies at the TeV scale cannot be reached by circular e^+e^- colliders because of the high energy loss via synchrotron radiation. A proton collider is thus preferred although the hadronic background environment renders the experiment more difficult. The 27 km ring of LEP accelerator and its injection scheme can be reused with only minor civil engineering modifications, which allows CERN to concentrate all efforts on the instrumentation and the experiments.

The accelerating complex of the SPS is used as injector for the LHC. The proton beams are accelerated in a linear accelerator (*Linac*) up to 50 MeV. Then two circular accelerators boost them to 1 GeV (*Booster*) and 26 GeV (*PS*) before they enter the Super Proton Synchrotron (*SPS*). There they reach the energy of 450 GeV and enter the LHC via two new tunnels (see Figure 1.1). The final energy of 7 TeV is limited by the magnetic field of 8.34 T in the super-conducting magnets.

Five experiments will make use of LHC. The ATLAS and CMS experiments located in new caverns built at IP1 and IP5 are multi-purpose central detectors. Their main (but not unique) task is to find the Higgs boson, using the full LHC potential by running at the very high design luminosity $\mathcal{L} = 10^{34}$ cm^{-2} s^{-1} . The ALICE experiment at IP2 will study the quark-gluon plasma in dedicated runs for heavy ions (Pb-Pb, Ca-Ca) collisions. TOTEM is a very small detector studying very forward QCD processes at IP5. It will measure the total cross-section at LHC, which is very important for the other experiments, for instance to measure absolute luminosity. Finally the LHCb experiment at IP8 is dedicated to b-quark physics and will be described in detail in Section 1.2.

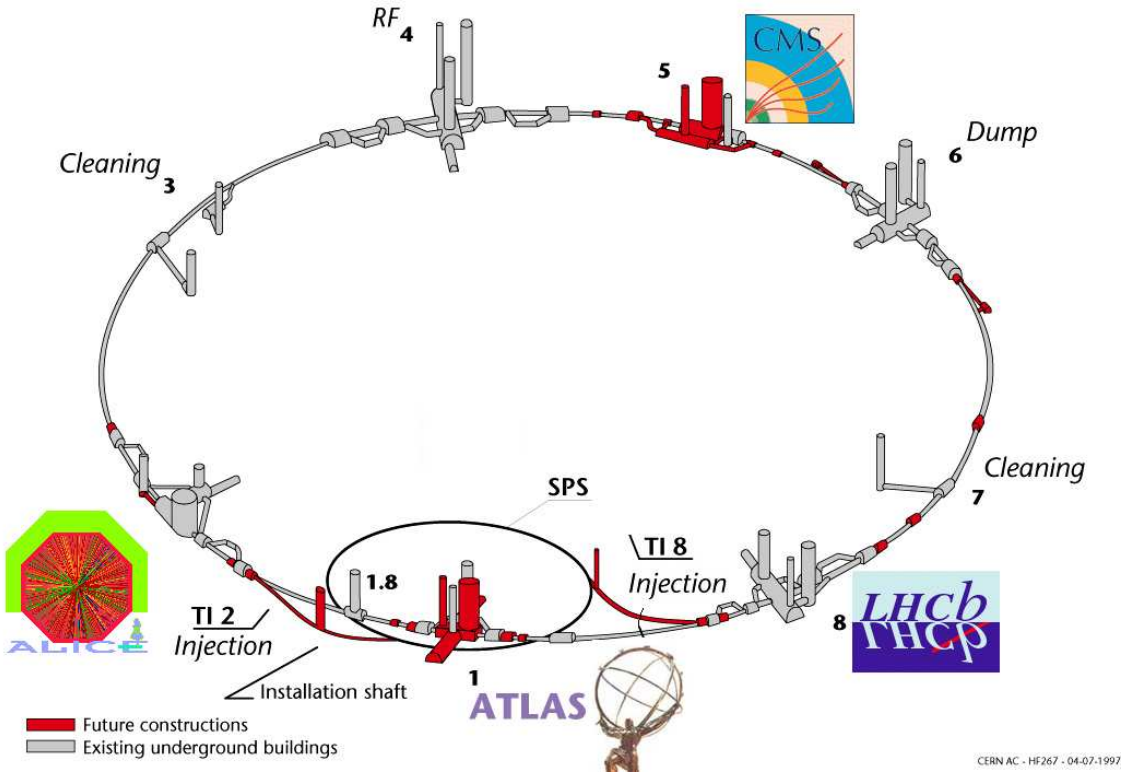

Figure 1.1: The LHC complex.

1.1.1 pp interactions

The relevant cross-sections at LHC are given in Table 1.1. The inelastic cross-section σ_{inel} is extrapolated basing on UA1, CDF and D$\varnothing$ data [1] but affected by large uncertainties. The total inelastic cross-section defines the average number of interactions per bunch crossing

$$\langle N_{pp} \rangle = \frac{\mathcal{L}\sigma_{inel}}{f_{bx}}$$

where $f_{bx} = 40$ MHz is the bunch crossing frequency. The average number of inelastic pp interactions per bunch-crossing ("primary vertices") is 17.4 at the maximal luminosity $\mathcal{L} = 10^{34}$ cm^{-2} s^{-1} and 0.37 for LHCb, that will work at a lower average luminosity $\mathcal{L} = 2 \times 10^{32}$ cm^{-2} s^{-1} , in order to avoid multiple pp interactions in the same event. At this luminosity there are interactions in 30% of the bunch crossings and the effective interaction rate is thus about 12 MHz.

1.1.2 b quark production

The cross-section $\sigma_{b\bar{b}}$ will be between 175 and 950 μb [2] depending on the value of badly known parameters. The value of 500 μb is a mean assumed as a refer-

Table 1.1: Cross-sections at LHC.

Total	σ_{tot}	100 mb
Inelastic	σ_{inel}	55 mb
$c\bar{c}$	$\sigma_{c\bar{c}}$	3.5 mb
$b\bar{b}$	$\sigma_{b\bar{b}}$	500 μb

ence by all LHC experiments. It will be known more precisely after the start of LHC. The dominant $b\bar{b}$ production mechanism in pp collisions is the fusion of two or more gluons radiated from the constituent quarks of the protons. This leads to an approximately flat distribution in rapidity and hence an angular distribution peaked at low polar angles. The directions of the two b hadrons are very correlated, as shown in Figure 1.2. The two peaks correspond to $b\bar{b}$ pairs flying in either directions of the beam axis. Consequently a dedicated b-physics experiment should cover low polar angles.

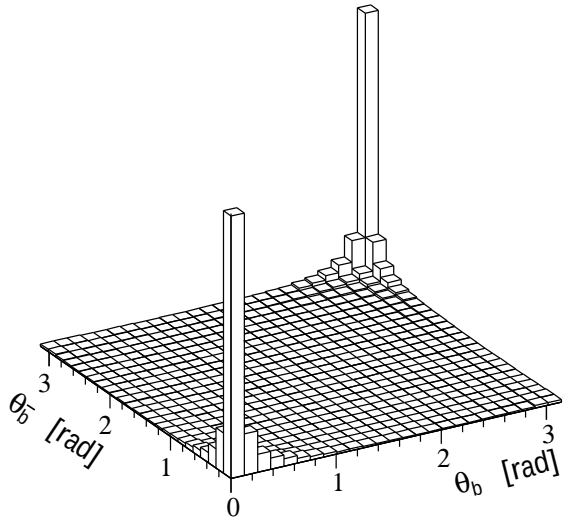

Figure 1.2: Polar angle θ of b and $\bar{b}$ hadron directions.

1.2 The LHCb detector

The LHCb detector [3] is a forward single arm spectrometer dedicated to the study of CP violation and other rare phenomena in the decays of Beauty particles. Its main features are:

- the precise particle identification to render a wide range of multi-particle final states accessible.
- the high-resolution micro-strip vertex detector allowing the identification of secondary vertices and precise proper-time measurements.
- its versatile trigger scheme including a hadron trigger to select hadronic b decays and a vertex trigger to select events with secondary vertices

The LHCb experiment looks like a fixed target experiment (e.g. HERA-B) because of the very forward peaked b-quark distribution at LHC. It will be located at IP8 in the pit where the Delphi experiment used to be. To avoid any civil engineering the detector has to fit in the present cavern, which constrains the total length of the detector to 20 m and requires a displacement of the interaction point by 11 m.

LHCb will study both low and high multiplicity events, like $B^0 \to \pi^+\pi^-$ and $B_s^0 \to D_s\pi$ respectively, hence has to be sensitive to a wide momentum range. The acceptance of the detector, as defined by the aperture of the magnet, is 300 mrad in the horizontal plane (bending plane) and 250 mrad in the vertical plane.

The major difficulty of an experiment looking for rare phenomena is the design of the trigger scheme. B events can be distinguished from other pp events by the presence of tracks with high transverse momentum (p_T) with respect to the beam axis and detached secondary vertices. The design of most sub-detectors is driven by triggering considerations.

The choice of the optimal luminosity is the result of a compromise between the maximization of the probability of having one interaction per bunch crossing and the need to keep the radiation damage low. A piled-up second primary vertex could be mis-identified by the trigger as a detached secondary vertex. At $\mathcal{L} = 2 \times 10^{32}$ cm^{-2} s^{-1} the rate of 0, 1 and more interactions is 27.7, 9.3 and 3.0 MHz respectively. Figure 1.3 shows the latest version of the LHCb detector geometry. One can see from left to right:

- the vertex locator (VELO)
- the upstream Ring-Imaging Cherenkov detector (RICH1)
- the trigger tracker (TT)
- the magnet
- the tracking system (T1 ... T3)

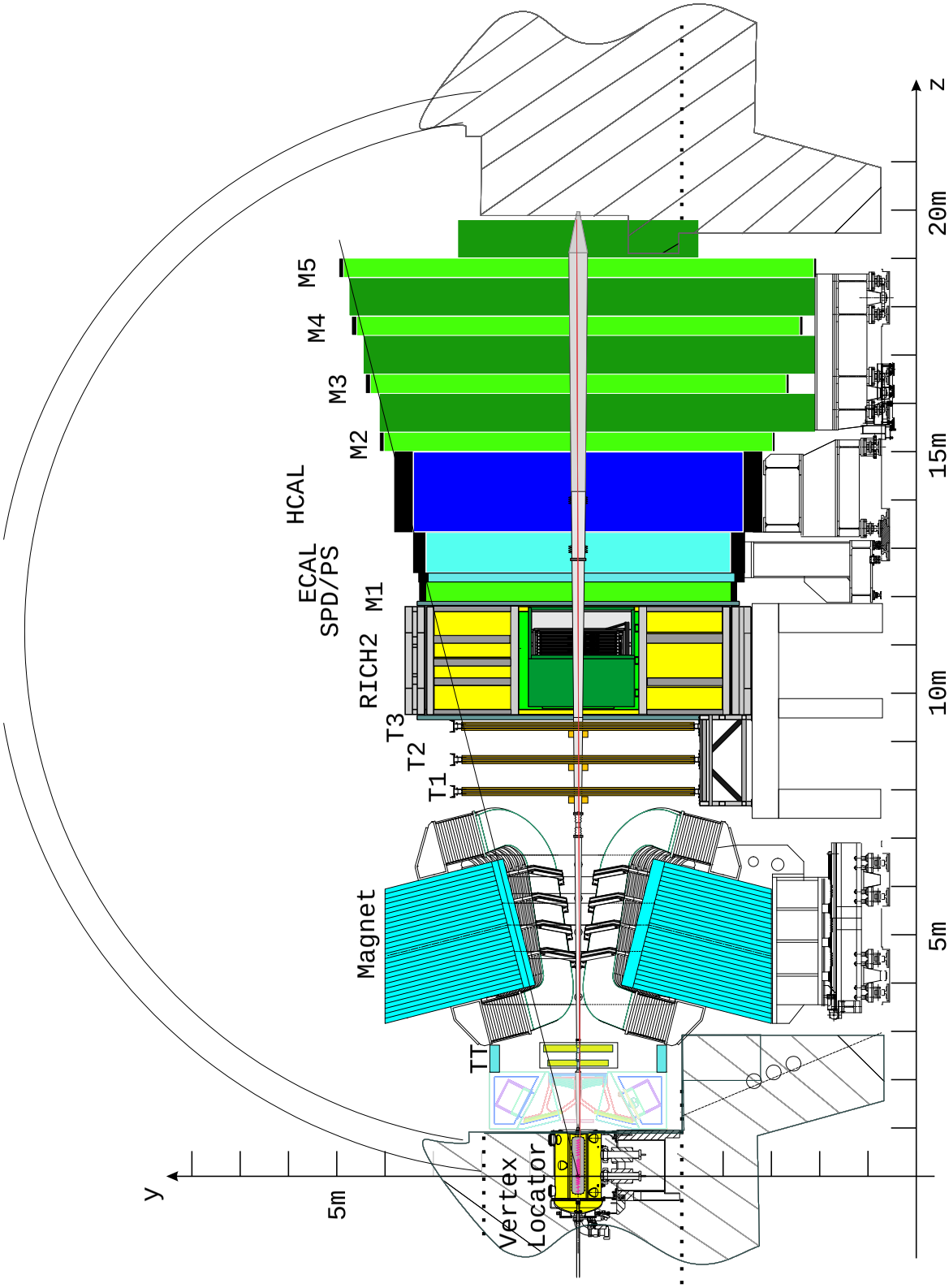

Figure 1.3: The LHCb detector geometry.

- the downstream Ring-Imaging Cherenkov detector (RICH2)
- the preshower (SPD/PS)
- the electromagnetic calorimeter (ECAL)
- the hadronic calorimeter (HCAL)
- the muon system (M1 ... M5)

1.2.1 The VELO

The vertex locator [4] provides precise informations about charged particles close to the interaction point. Its fine segmentation allows for a precise primary vertex reconstruction and a search for detached secondary vertices. As it surrounds the interaction region it also allows some knowledge about the backward side of the event, which helps disentangling multiple primary vertices.

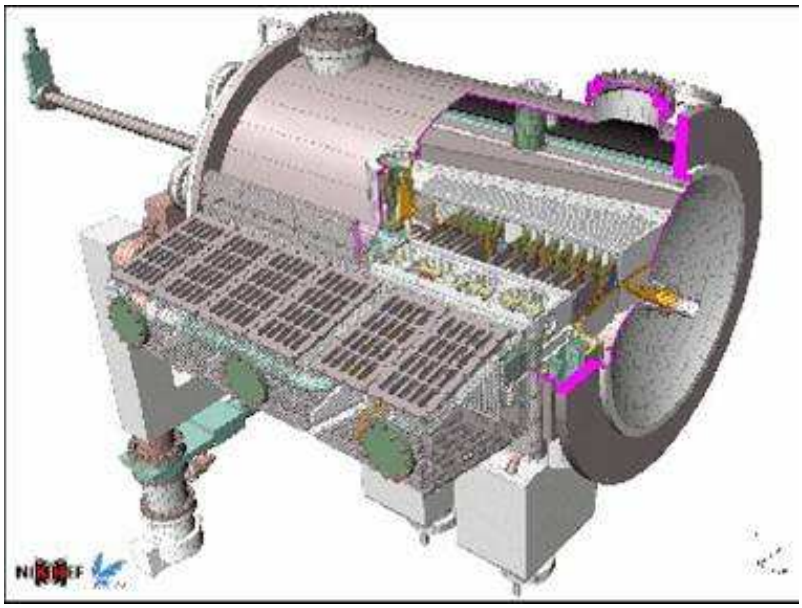

Figure 1.4: A cross-section of the VELO tank.

The detector is composed of 21 parallel disk-shaped silicon strips, with a $r-\phi$ segmentation geometry. The position resolution of the primary vertex is 40 μm in z and 8 μm in x and y. For secondary vertices it varies from 150 and 300 μm (in z) depending on the number of tracks. This corresponds to less than 50 fs resolution on the B proper time of flight. The VELO is used for the Level-1 trigger which enriches the B event content by finding high impact parameter tracks and secondary vertices.

1.2.2 The beam pipe

After the exit wall of the VELO the LHC beam is protected by a beam pipe [5] made of two conical sections. The first section leads through RICH1 and has an opening angle of 25 mrad. It is followed by a second section with an opening angle of 10 mrad. The minimal radius is 2.5 cm (limited by LHC injection requirements) and the final radius of the second section is 13 cm. The main part is made of a 40%-60% Al-Be alloy.

1.2.3 The RICH

The two Ring-Imaging Cherenkov detectors [6] use the Cherenkov effect to identify particles. Their main task is to allow the separation of kaons from pions over the full momentum range accessible from LHCb.

For the K-π separation the benchmark is the distinction between the $\mathrm{B} \to \mathrm{K}\pi$ and the $\mathrm{B}^0 \to \pi^+\pi^-$ channels. The RICH achieves a K-π separation above 3σ for tracks in the range 3-90 GeV. It is also crucial to tag the flavor of the reconstructed B using the kaon from the $\mathrm{b} \to \mathrm{c} \to \mathrm{s}$ decay chain from the other b-hadron.

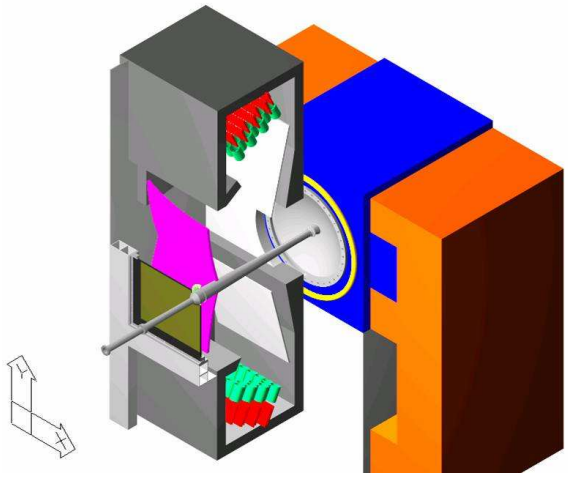

Figure 1.5: A cross-section of RICH1 linked to the VELO tank.

The RICH detects ring images formed by Cherenkov photons around the track of the particle traversing the detector. The photons are detected by cylindrical pixelated Hybrid photodiode (HPD) tubes. These detectors are sensitive to magnetic fields, which imposes that RICH is located outside of the bending area. Because of this requirement and as there is a strong correlation of the momentum and the polar angle of the track ($\theta \simeq 1/P$) it is segmented in two parts:

- the upstream RICH (RICH1) located before the magnet uses silica aerogel (refractive index n=1.03) and $\mathrm{C_4F_{10}}$ (n=1.0014) as radiators. It is designed for low momentum (1-70 GeV) and high angle (30-300 mrad) tracks. The light is reflected by spherical mirrors onto the photo-detector.

- the downstream RICH (RICH2) located after the magnet uses CF_4 (n=1.0005) as radiator. It covers high momentum (12-150 GeV) and low angle tracks (15-120 mrad).

1.2.4 The Trigger Tracker

The Trigger Tracker (TT) is located downstream of RICH1 and in front of the entrance of the LHCb magnet. It is used both in the Level-1 trigger, to assign transverse-momentum information to large impact parameter tracks, and in the off-line analysis, to reconstruct the trajectories of long-lived neutral particles that decay outside of the fiducial volume of the VELO and of low-momentum particles that are bent out of the acceptance of the detector before reaching tracking stations T1-T3.

The active area of the trigger tracker is entirely covered by silicon microstrip detectors with a strip pitch of 198 μm and strip lengths of up to 33 cm.

1.2.5 The Magnet

The dipole magnet [7] is located close to the interaction point to keep it small, but after the iron shielding wall which protect the VELO and RICH1 from the magnetic field. The field is oriented vertically which makes the tracks to bend in the horizontal $x - z$ plane. It has a maximal intensity of 1.1 T and a total integral of 4 Tm on average.

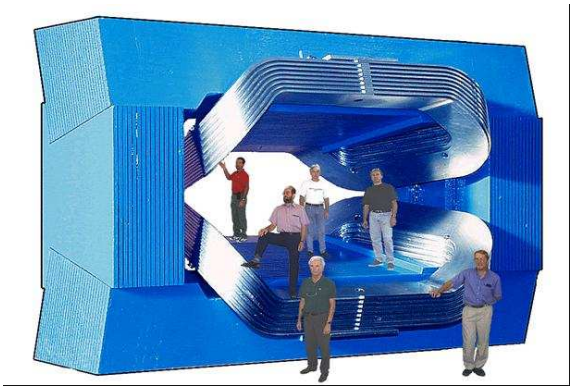

Figure 1.6: The LHCb magnet.

Its aperture is 300 mrad in the bending plane and 250 mrad in the vertical plane. The magnet is made of 50 tons of aluminum conducting wires (9 km in total) and of a 120 kt steel plate yoke. It dissipates 4.2 MW.

To compensate for possible left-right asymmetries in the detector, one has to be able to reverse the polarity of the magnet field. This requirement and a detailed cost analysis have lead to the choice of a warm magnet rather than a superconducting magnet.

1.2.6 The Tracking system

The tracking system [8, 9] provides the momentum measurement of charged particles and links the tracks found in the VELO to the hits in the trigger tracker, in the calorimeters and in the muon detector. It also provides the seeding information for the RICH counters. A mass resolution requirement of 10 MeV in high-multiplicity decays-as $B_s^0 \rightarrow D_s K$ translates to a momentum resolution requirement of $\delta p/p \leq 0.4\%$.

The tracker consists of three stations perpendicular to the beam axis. Every tracking station measures the x coordinate which is in the bending plane and 2 *stereo* coordinates at $x \pm 5$, to have also some information about y and to resolve ambiguities. As the track density at fixed z approximately follows $1/r^2$, the tracking system is segmented in an inner tracker located close to the beam pipe and an outer tracker which covers the remaining 98% of the area.

The Inner Tracker

The inner tracker (IT) covers the innermost part of the tracking stations T1 ... T3. The latest design foresees cross-shaped stations equipped with silicon detectors. The silicon foils are 300 μm thick and have a 230 μm strip pitch. This allows for a resolution of 70 μm . The same read-out scheme as for the VELO is foreseen, except for the interface to the Level-1 trigger which is not needed by the IT.

The Outer Tracker

The outer tracker (OT) extends to the outermost part of the tracking stations. It is made of drift cells called straw tubes. These have a 5 mm diameter and 75 μm thick walls. To reach an average resolution on the momentum of $\delta p/p \leq 0.4\%$ the tracking precision has to be optimal in the $x - z$ magnet bending plane. Therefore most stations have two planes with wires in the vertical direction and two stereo planes with wires in the horizontal direction.

The drift gas is an $Ar/CF_4/COF_2$ mixture which optimizes the drift speed. The total drift, amplification and transmission time is kept slightly below 50 ns, which is the delay between two LHC bunch crossings. Thus it can happen that two events are piled-up in the outer tracker.

1.2.7 The Calorimeters

The calorimetry system [10] identifies photons, electrons and hadrons and measures their position and energy, which are used as input to the Level-0 trigger. As for the VELO, the design is motivated by fast triggering requirements. Thus the detector description is a compromise between a small number of read-out channels and a low occupancy with a reasonable energy and position resolution. Fast binary read-out has been chosen to cope with the Level-0 trigger requirements.

The Electromagnetic Calorimeter and the Preshower

The electromagnetic calorimeter system (ECAL) detects electrons and photons via showers of $\mathrm{e^+e^-}$pairs and photons. Its total radiation length is $25X_0$. It is segmented in two parts:
The preshower consists of 12 mm of lead followed by 15 mm of scintillators. It allows the separation of photons and electrons by the different shapes of the electromagnetic showers induced in the ECAL.
The electromagnetic calorimeter uses the Shashlik technology with lead as absorber material. It is segmented in three resolution zones in order to optimize the π^0 reconstruction.

The Hadronic Calorimeter

The hadronic calorimeter (HCAL) identifies hadrons ($\pi^{\pm}$, $\mathrm{K}^{\pm}$, $\mathrm{K}^0_{\mathrm{L}}$, p, n, Λ) via inelastic interactions with the detector material. The products of the interaction are mainly π which are detected in the scintillators (the π^0 via the electromagnetic shower of the γ).

The HCAL is made of 16 mm thick iron and 4 mm thick scintillating tiles, parallel to the beam. The light is collected at the end of the tile by wavelength shifting fibers (WLS).

1.2.8 The Muon System

The muon detector [11] identifies muons, the only charged particle able to traverse the calorimeters without interacting. As high p_{T} muons are mainly produced in B decays, the muon detector is an essential component of the Level-0 trigger. It is also used in the muon identification which is an basic ingredient of the search for rare semileptonic decays.

The detector consists of a muon shield (composed of the ECAL, the HCAL and four layers of iron) and of 5 stations. It will be described in more detail in Chapter 2.

1.3 The LHCb trigger

The trigger is an vital component of the LHCb experiment and it is its major challenge. Most sub-detectors designs are motivated by triggering considerations. The high interaction rate, the low b cross-section compared to the total cross-section and the high-multiplicity environment make arduous to efficiently select interesting B-decays.

The bunch-crossing frequency is 40 MHz. Every 25 ns a pp event can occur. At $\mathcal{L} = 2 \times 10^{32}$ cm^{-2} s^{-1} an inelastic pp interaction (called minimum bias event) happens at an average rate of 17 MHz. The ratio of the $\mathrm{b\bar{b}}$ and inelastic minimum bias cross-sections is about 100. The $\mathrm{b\bar{b}}$ production rate is thus about 150 kHz.

Essentially rare B^0 decays – $\mathcal{O}(10^{-3})$ or less – are of interest for CP violation studies. Adding up all the physics channels (listed in [5]) one gets 120 physics events per second. Requiring that all tracks are detected one ends with about 10 B events per second which can be used for physics analysis.

For every B event of interest there are thus 10^6 background events. The reduction to 200 events that will be written to storage per second is achieved in a three-level trigger scheme [13]. The steps of the trigger algorithm are described below and summarized in Table1.2.

Table 1.2: Summary of the trigger scheme.

Level	Selects	Input rate	Reduction	Latency
Pile-up system	Single events	13 MHz	1.3	
Level-0	High p_T tracks	10 MHz	10	4 μs
Level-1	Secondary vertices	1 MHz	25	$\approx$ 1.6 ms
HLT	Reconstructed B events	40 kHz	200	
Events are written on tape		200 Hz		

1.3.1 The Level-0 trigger

The Level-0 [1] (L0) exploits the high mass of the B-meson, resulting in decay products with high transverse momentum (p_T). High-p_T photons, electrons, hadrons and muons are reconstructed in the electromagnetic, hadronic calorimeter and the muon system, respectively. The pile-up system, consisting of two VELO disks upstream the interaction region, identifies multiple interactions and is used to suppress events with multiple vertices or with large hit multiplicity. Hence more low-multiplicity events are retained while keeping the same accept rate, and therefore both the average event size and computing time are reduced, with even a slight increase of selection efficiency. The pile-up information, together with the highest-p_T photon, electron and hadron, and the two highest-p_T muons, are passed to the L0 decision unit, which forms the final decision.

The fully synchronous L0-trigger has a fixed latency of 4 μs and is implemented in custom boards. The rate at the L0 output is reduced to 1 MHz. Efficiencies of approximately 90%, 70% and 50% are achieved for events with muons, hadrons and photons respectively.

The relative weight of each trigger can be tuned by changing the single cuts, depending on the type of physics one wants to favor. The optimization of the cuts for the precise measurements of CP-violating parameters leads to a bandwidth of 60% for the hadron trigger, 10% for the electron trigger, 10% for the photon trigger and 20% for the muon trigger.

[1] The trigger levels are numbered from 0 for historical reasons. The other experiments number starting from 1

1.3.2 The Level-1 trigger

The Level-1 trigger (L1) reduces the rate further to 40 kHz, using information from the VELO and the TT station [2]. The algorithm will be implemented on a commodity processor farm, that will be shared with the High Level Trigger (HLT) and the off-line reconstruction. The available time at L1 is on average $\sim$ 1 ms, with a maximum latency of 52.4 ms given by the L1 buffer size.

Large impact parameter tracks are reconstructed and matched to clusters in the TT station. The fringe field between the VELO and the TT is sufficient to obtain momentum information with a precision of $\sim$ 30%. In addition the tracks are matched to muon candidates from L0, enhancing the performance for channels containing muons. Using two high impact parameter tracks with the highest p_{T} , efficiencies between 50% and 70% are achieved.

1.3.3 The High Level Trigger

The full detector information is available at the High Level Trigger (HLT). The tracking stations (T1-T3) provide more precise momentum information, with which the L1 decision can be confirmed within 4 ms, reducing the rate by a factor 2, while retaining signal efficiency above 95%. The remaining time ($\sim$ 14 ms) is used to select the individual channels with an output rate of $\sim$ 10 Hz per channel.

1.4 Simulating LHCb

The software applications of LHCb are based on an object oriented (OO) C++ framework called Gaudi [14]. The simulation package GAUSS [15], based on GEANT 4 [16] is not yet completely debugged and presently it is still used the Fortran package SICBMC [17], based on GEANT 3 [18] for the detector description and PYTHIA 6 [19] and QQ [20] for the physics event generation. The other packages are BOOLE [21] for the digitization of the event, BRUNEL [22] for the reconstruction, and DAVINCI [23] for the analysis.

The single packages will be described in detail in the chapter 4

1.5 Physics performance of the LHCb experiment

The current $\mathrm{e^+e^-}$B-factories have measured CP violation in the B-system with very high accuracy [24], $\sin 2\beta = 0.731 \pm 0.055$, and in excellent agreement with the indirect measurement of $|V_{ub}|/|V_{cb}|$ and Δm_d from semi-leptonic $\mathrm{B^0}$-decays and $\mathrm{B^0}$-$\overline{\mathrm{B}}$ oscillations [25], $\sin 2\beta = 0.695 \pm 0.055$.

After one year of nominal operation of LHC the data sample collected by LHCb will be sufficient to determine β with similar accuracy as is foreseen by the B-factories. The Standard Model analysis predicts a value of the CKM angle γ of

[2] T1 ... T3 and M2 ... M5 can be included in L1

$64.5^{\circ} \pm 7^{\circ}$. The direct measurement of γ is one of the main purposes of LHCb. The high $\mathrm{b\bar{b}}$ cross-section and luminosity will provide an unprecedented large sample of $\mathrm{B_s^0}$-mesons, with which this can be achieved.

In addition, basic parameters like the mass difference Δm_s and the lifetime difference $\Delta\Gamma_s$ of the two $\mathrm{B_s^0}$mass-eigenstates will be determined with high precision [26]. Moreover, any new particle present in the loop diagrams could significantly enhance the branching ratios of channels with very low branching ratios in the Standard Model, such as $\mathrm{B^0}\rightarrow \mathrm{K^{*0}}\gamma$, or the experimentally very clean decays containing muons, $\mathrm{B^0}\rightarrow \mu^+\mu^-\mathrm{K^{*0}}$, $\mathrm{B_s^0}\rightarrow \mu^+\mu^-$ and $\mathrm{B^0}\rightarrow \mu^+\mu^-$, whose estimated Standard Model branching ratios are 8×10^{-7}, 4×10^{-9} and 10^{-10} respectively.

Table 1.5 lists the performance of the LHCb experiment for the most promising decay channels to construct the unitarity triangle. The numbers are given for one year of data taking, which corresponds to 10^7 seconds of running at $\mathcal{L} = 2\times10^{32}$ cm^{-2} s^{-1} , hence an integrated luminosity of 2 fb^{-1}.

Table 1.3: Performance of the LHCb experiment after one year of data taking for selected benchmark channels and related CKM parameters. The annual yields include both the indicated decays and their charge conjugates, but not the tagging efficiency.

Decay Channel	Annual Yield	Physics Performance
$\mathrm{B^0}\rightarrow \mathrm{J/\psi K_S}$	240k	$\sigma(\sin2\beta) = 0.02$
$\mathrm{B^0}\rightarrow \rho\pi$	4.4k	$2.5^{\circ} < \sigma(\alpha) < 5.0^{\circ}$
$\mathrm{B^0}\rightarrow \mathrm{D^{*-}}\pi^+$	206k	$\sigma(\gamma) = \mathcal{O}(10^{\circ})$
$\mathrm{B_s^0}\rightarrow \mathrm{J/\psi}\phi$	120k	$\sigma(\delta\gamma) \approx 2^{\circ}$
$\mathrm{B_s^0}\rightarrow \mathrm{D_S^-}\pi^+$	80k	$\sigma(\Delta m_s) \approx 0.01\mathrm{ps}^{-1}$
$\mathrm{B^0}\rightarrow \pi^+\pi^-$	26k	
$\mathrm{B^0}\rightarrow \mathrm{K^+}\pi^-$	135k	
$\mathrm{B_s^0}\rightarrow \pi^+\mathrm{K^-}$	5.3k	
$\mathrm{B_s^0}\rightarrow \mathrm{K^+K^-}$	37k	

To conclude the physics capability of LHCb, we want to stress that an extensive and peculiar study of high-energy hadron physics is obtainable, in addition to CP-violation program. For instance the extreme forwardness of LHCb, with a rapidity coverage up to 8, turns out to be very useful for the determination of the proton structure functions at very low parton fractional momenta. A comprehensive case study will be treated in the second part of the thesis.

Chapter 2

The Muon System

2.1 Introduction

Muon triggering and off-line muon identification are fundamental requirements of the LHCb experiment. Muons are present in the final states of many CP sensitive B decays, in particular the two "gold-plated" decays, $B^0 \to J/\psi(\mu\mu)K^0_S$ and $B^0_s \to J/\psi(\mu\mu)\phi$. Moreover, muons from semi-leptonic b decays provide a tag of the initial state flavor of accompanying neutral B mesons. In addition, the study of rare B decays such as the Flavor Changing Neutral Current decay, $B^0_s \to \mu\mu$, may reveal new physics beyond the Standard Model.

The LHCb muon detector uses the penetrative power of muons to provide a robust muon trigger. The heavy flavor content of triggered events is enhanced by requiring the candidate muons to have high transverse momentum, p_T . The same unique properties are utilized off-line, to accurately identify muons reconstructed in the tracking system and to provide a powerful B meson flavor tag.

2.2 Physics requirements

The main requirement for the muon detector is to provide a high p_T muon trigger at the earliest trigger level (Level-0). The effective LHCb Level-0 input rate is about 15 MHz on average at $\mathcal{L} = 2 \times 10^{32}$ cm^{-2} s^{-1} , assuming a non-diffractive p-p interaction cross-section of 55 mb. This input rate must be reduced to 1 MHz within a latency of 4.0 μs , while retaining good efficiency for events containing interesting B decays. The muon trigger provides between 10% and 30% of this trigger rate. In addition, the muon trigger must unambiguously identify the parent bunch crossing, requiring a time resolution better than 25 ns.

The muon system must also provide off-line muon identification. Muons reconstructed in the high precision tracking detectors with momenta down to 3 GeV/c must be correctly identified with an efficiency of about 95% while keeping the hadron misidentification rate below 1%. Efficient muon identification with low

contamination is required both for tagging and the clean reconstruction of muonic final state B decays.

The muon trigger is based on a muon track reconstruction and p_{T} measurement with a resolution of 20%. Hits in the first two stations are used to calculate the p_{T} of the candidate muon.

2.3 General detector structure

The muon detector consists of five muon tracking stations placed along the beam axis. The first station (M1) is placed in front of the calorimeter preshower, at 12.1 m from the interaction point, and is important for the transverse-momentum measurement of the muon track used in the Level-0 muon trigger. The remaining four stations are embedded within the muon shield at mean positions of 15.2 m (M2), 16.4 m (M3), 17.6 m (M4) and 18.8 m (M5). The shield is comprised of the electromagnetic and hadronic calorimeters and three iron filters and has a total absorption-length of 20 nuclear interaction-lengths. The minimum momentum requested to a muon to traverse the 5 stations is 5 GeV/c. The positions of the muon stations can be seen in Figure 2.1, which shows a side view.

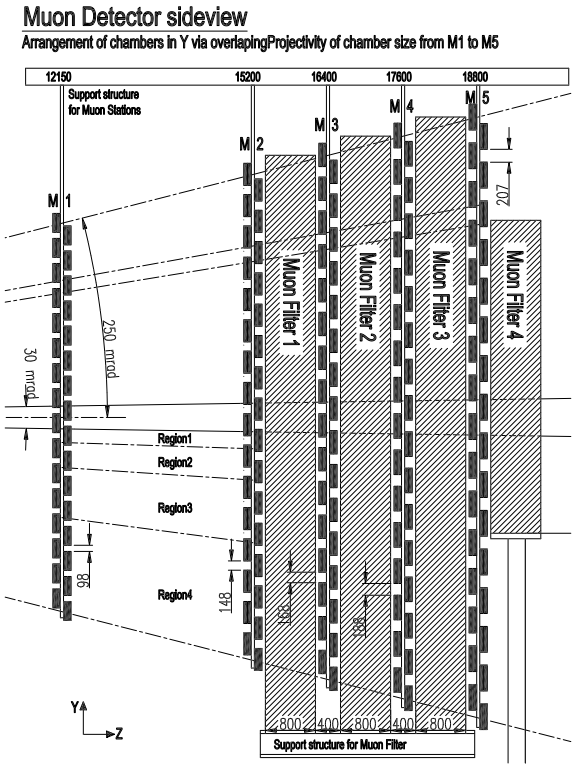

Figure 2.1: Side view of the muon system.

The chambers within the filter are allocated about 40 cm of space and are separated by three shields of 80 cm thickness. The inner and outer angular acceptances

of the muon system are 20 (16) mrad and 306 (258) mrad in the bending (non-bending) plane, similar to that of the tracking system. This provides a geometrical acceptance of about 20 % for muons from b decays relative to the full solid angle. The total detector area is about 435 m^2 .

2.4 Logical layout

The Muon system provides a digital information about the $x-y$ spatial coordinates of the muon tracks. The spatial resolution is given by the dimension of a logical pad, whose structure across the detector represents the logical layout. The logical layout describes the x and y granularity in each region of each muon station, as seen by both the muon trigger and the off-line reconstruction.

Since the polar angle and the momentum of the particles are correlated, high momentum tracks tend to be closer to the beam axis. Therefore multiple scattering in the absorber increases with the distance from the beam axis, limiting the spatial resolution of the detector. The granularity of the logical pads varies accordingly, and have been chosen such that its contribution to the p_{T} resolution is approximately equal to the multiple-scattering contribution. The various contributions to the p_{T} resolution are shown in Figure 2.2.

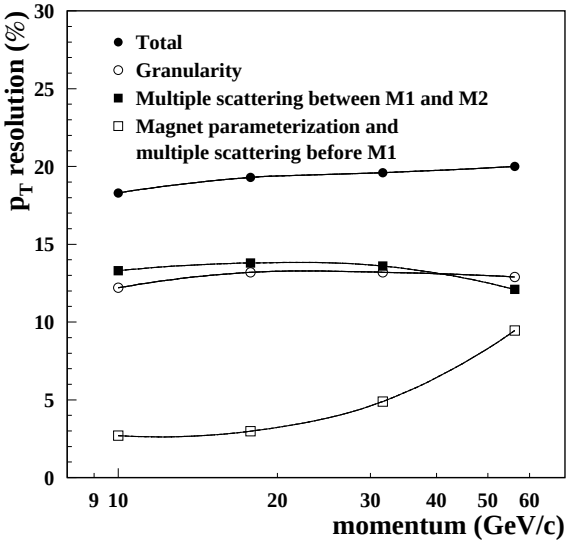

Figure 2.2: Contributions to the transverse momentum resolution of the muon system as a function of the muon momentum averaged over the full acceptance. The p_{T} resolution is defined as $(p_{\mathrm{T}}^{rec} - p_{\mathrm{T}}^{true})/p_{\mathrm{T}}^{true}$, and is shown for muons from semi-leptonic b decay having a reconstructed p_{T} close to the trigger threshold, between 1 and 2 GeV/c.

Given the different granularity requirements and the large variation in particle flux in passing from the central part, close to the beam axis, to the detector border,

each station is subdivided into four regions with different logical-pad dimensions Region and pad sizes scale by a factor two from one region to the next.

In the y plane all the tracks appear to straight lines, as they are not bent by the magnet, thus the required granularity is broader, and the logical pads are wide, as appear in Figure 2.3.

Otherwise the x dimensions of the logical pads are determined primarily by the precision required to obtain good muon p_{T} resolution for the Level-0 trigger. The resulting y/x aspect ratios are 2.5 in station M1 and 5 for stations M2 and M3. Stations M4 and M5, which are used to confirm the presence of penetrating muons, have aspect ratios of 1.25. The total number of logical pads in the muon system is 55,296.

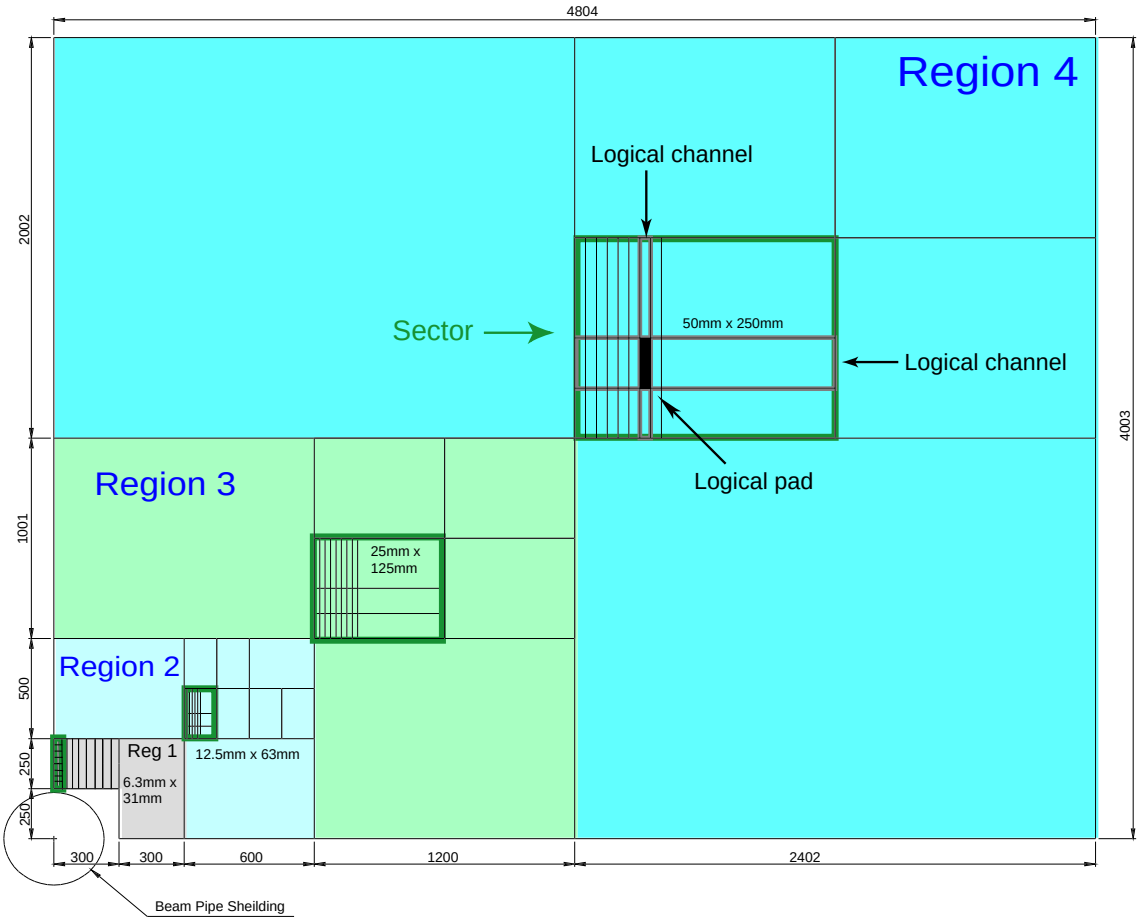

Figure 2.3: Front view of one quadrant of muon station 2, showing the dimensions of the regions. Inside each region is shown a sector, defined by the size of the horizontal and vertical strips. The intersection of the horizontal and vertical strips, corresponding to the logical channels, are logical pads. The region and channel dimensions scale by a factor two from one region to the next.

Each logical pad may group one or more physical pads, whose dimensions are limited by occupancy and capacitance considerations, according to the detector

technology. The Muon system has been designed in a flexible way, such that the required logical layout can be achieved in several ways and is independent from the detectors used (see Figure 2.4).

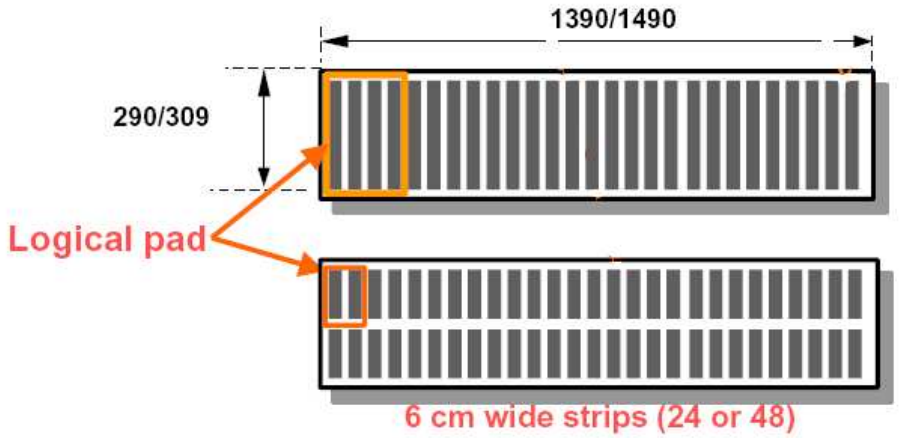

Figure 2.4: Logical pads and physical pads in Region 4 (top) and Region 3 (bottom) for Stations M4 and M5. In the former case the x dimension is that of 4 chamber strips and the y dimension is the same of the chamber itself. In the latter case more granularity is required and both x and y have half dimensions.

2.5 Detector Requirements and Specifications

The basic function of the LHCb Muon system is to identify and trigger on muons produced in the decay of b hadrons. The trigger logic is designed in such a way that information from all five muon stations is required. Thus the trigger efficiency is highly affected by the single station efficiency, as

$$\epsilon_{trigger} = (\epsilon_{station})^5$$

As a result, in order to achieve a muon trigger efficiency of at least 95%, the single-station efficiency has to be higher than 99%. This is ensured by having more than one independent detector layers per station and taking the logical OR.

The detector efficiency is mainly limited by the intense flux of charged and neutral particles in the angular coverage of the LHCb experiment. These flux levels exceed those experienced by the ATLAS [27] and CMS [28] muon spectrometers and pose a different challenge.

2.5.1 Background environment

High particle fluxes in the muon system impose stringent requirements on the instrumentation. These requirements include the rate capability of the chambers,

the aging characteristics of the detector and redundancy of the trigger instrumentation. The high hit rates in the chamber also effect the muon transverse momentum resolution due to incorrect hit association. Four classes of backgrounds relevant to the $B \to \mu X$ detection can be distinguished:

1. *Decay muons:* The large number of π/K mesons produced in the p-p collisions contribute mainly to the background in the muon system through decays in flight. Such decay muons form the main background for the L0 muon trigger.

2. *Shower particles:* Photons from π^0 decays can interact in the area around the beam pipe and generate electromagnetic showers penetrating into the muon system. Hadrons emerging from the primary collision can interact late in the calorimeters and contribute to the background in the muon system through shower muons or hadron punch-through.

3. *Low-energy background:* Another important background is associated with low-energy neutrons produced in hadronic cascades in the calorimeters, the muon shield or in accelerator components. They create low-energy radiative electrons via nuclear n-γ processes and subsequent Compton-scattering or via the photo-electric effect in the detector material of the muon chambers. The photons have a probability of a few per mil to generate detectable electrons via these effects, which are in general only affecting a single detector layer. Moreover, the hits due to the low energy background occur up to a few 100 ns after the primary collision.

4. *Beam halo muons:* The charged-particle flux associated with the beam halo in the accelerator tunnel contains muons of a rather wide energy spectrum and the largest flux at small radii. In particular those halo muons traversing the detector in the same direction as particles from the interaction point can cause a L0 muon trigger.

Background caused by real muons traversing the detector is well simulated with the available Monte Carlo packages [29, 30]. An estimate for the rate in the various regions of the muon system has been obtained from a detailed study [31, 32] whose results are summarized in Table 2.1.

The nominal rates are calculated for a luminosity of $\mathcal{L} = 5 \times 10^{32}$ cm^{-2} s^{-1}, at which the LHCb experiment should be able to operate for short periods. The maximal rates are then obtained applying a safety factor of 5 in the stations M2-M5 and a safety factor of 2 in the station M1, which is positioned in front of the calorimeters and therefore is less affected by the uncertainties in the showering processes in the absorber material. The rate rises from a few hundred Hz/cm^2 in the outer regions of stations M4 and M5 to a few hundred kHz/cm^2 in the innermost part of station M1.

2.5.2 Muon system technologies

The combination of physics goals and background conditions determines the choice of detector technologies for the various stations and regions. The following param-

Table 2.1: Particle rates in the muon system. The first row gives the maximal particle rate in each region and station per interaction as obtained from the simulation; the second gives the calculated rate at a luminosity of $\mathcal{L} = 5 \times 10^{32}$ cm^{-2} s^{-1} assuming a total $\mathrm{p}-\mathrm{p}$ cross-section of σ=102.4 mb; and the last row the rate including the safety factors.

	Region 1	Region 2	Region 3	Region 4
Station 1	8.3×10^{-3}/cm^2 230 kHz/cm^2 460 kHz/cm^2	3.3×10^{-3}/cm^2 93 kHz/cm^2 186 kHz/cm^2	1.4×10^{-3}/cm^2 40 kHz/cm^2 80 kHz/cm^2	4.5×10^{-4} /cm^2 12.5 kHz/cm^2 25 kHz/cm^2
Station 2	2.7×10^{-4}/cm^2 7.5 kHz/cm^2 37.5 kHz/cm^2	1.9×10^{-4}/cm^2 5.3 kHz/cm^2 26.5 kHz/cm^2	4.7×10^{-5}/cm^2 1.3 kHz/cm^2 6.5 kHz/cm^2	8.3×10^{-6}/cm^2 230 Hz/cm^2 1.2 kHz/cm^2
Station 3	7.2×10^{-5}/cm^2 2 kHz/cm^2 10 kHz/cm^2	2.3×10^{-5}/cm^2 650 Hz/cm^2 3.3 kHz/cm^2	7.3×10^{-6}/cm^2 200 Hz/cm^2 1.0 kHz/cm^2	3.0×10^{-6}/cm^2 83 Hz/cm^2 415 Hz/cm^2
Station 4	4.7×10^{-5}/cm^2 2.3 kHz/cm^2 6.5 kHz/cm^2	1.6×10^{-5}/cm^2 430 Hz/cm^2 2.2 kHz/cm^2	5.4×10^{-6}/cm^2 150 Hz/cm^2 750 Hz/cm^2	1.8×10^{-6}/cm^2 50 Hz/cm^2 250 Hz/cm^2
Station 5	3.2×10^{-5}/cm^2 880 Hz/cm^2 4.4 kHz/cm^2	1.3×10^{-5}/cm^2 350 Hz/cm^2 1.8 kHz/cm^2	4.7×10^{-6}/cm^2 130 Hz/cm^2 650 Hz/cm^2	1.7×10^{-6}/cm^2 45 Hz/cm^2 225 Hz/cm^2

eters particularly affects the technology choice:

1. *Rate capability:* The selected technologies must provide single layer efficiencies of more than 95% at the expected rates.

2. *Ageing:* The materials of the detectors should have good ageing properties, allowing 10 years of operations. Moreover, the detector itself should tolerate the total integrated charge accumulated in that period.

3. *Time resolution:* The muon system must provide unambiguous bunch crossing identification with high efficiency. The requirement is at least 95% efficiency within a 20 ns window for each of the two layers in the station.

4. *Spatial resolution:* The spatial resolution must allow the determination of the p_{T} of triggering muons with a resolution of 20%. This requires a granularity varying from few mm in the innermost region of stations M1 and M2, to few tens of cm in station M5. To minimize the deterioration of the intrinsic detector resolution, cross talk between readout channels should be limited below 10%.

Based on the above considerations, three different detector technologies have been proposed to cover the 435 m^2 of the Muon system.

Multiwire Proportional Chambers (MWPC) represent a well known and robust technology, adopted as the base type of detector, in all the regions where the expected particles rates are between 1 kHz/cm^2 and 200 kHz/cm^2 . In order to provide the necessary efficiency and time resolution, one chamber is formed by 4 wire planes, and the signal are ORed.

In the innermost region of the Muon system (station M1, region R1) the rate of almost 500 kHz/cm^2 might not allow to use MWPC because of ageing. Since an exhaustive test has not been possible, the Gap Electron Multiplier (GEM) detector has been suggested as a possible and safer alternative for this part of the Muon system, which is however rather small, being about few m^2 .

2.6 The Resistive Plate Chambers

In regions R3 and R4 of stations M4 and M5 the expected rate is below 1 kHz/cm^2 , and the requirements on spatial resolution are rather modest due to the large size of logical pads. The Resistive Plate Chambers (RPC) [34] were originally proposed for this part of the Muon system, representing the 48% of the total surface.

Figure 2.5: RPC detector during the assembling. The front-end boards are visible.

In last few years considerable R&D on this type of detectors had led to the design of a particular configuration, consisted in two Single-gap RPCs whose signals are independently read out by two strip planes, and then ORed (Figure 2.6).

Figure 2.7 shows a typical time spectrum for a Single-gap RPC. The sigma of the Gaussian fit gives an excellent time resolution of $\sim$ 1.1 ns, with the full efficiency reached already in a 10 ns time window, well within the LHC bunch

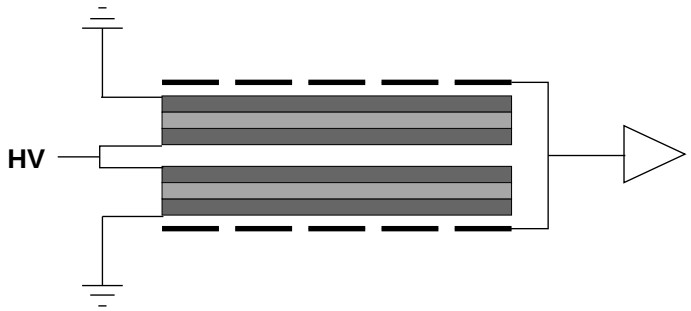

Figure 2.6: Sketch of the RPC configuration which were proposed for LHCb. It is composed by two Single-gaps in OR.

crossing distance (25 ns), even considering any possible jitter introduced by the electronic chain. Moreover the performance of two gaps in OR is supposed to be even improved.

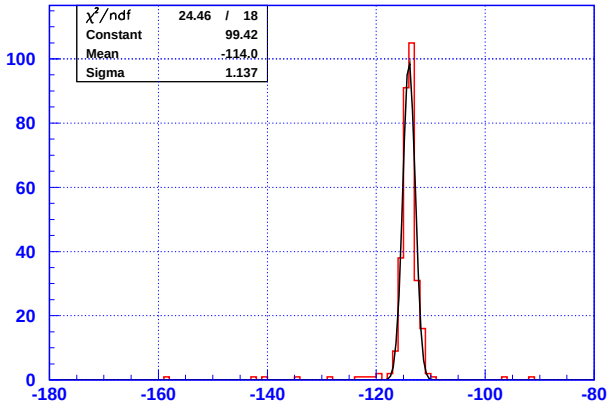

Figure 2.7: Time resolution of a RPC. The x scale is in ns.

The efficiency curve is reported in Figure 2.8. The OR of the two planes reaches 99.5%, and is consistent with the theoretical efficiency computed by multiplying the inefficiencies of the Single-gaps, according to the relation

$$\epsilon_{A+B} = 1 - (1 - \epsilon_A)(1 - \epsilon_B)$$

The little discrepancy is due to some correlation in the efficiencies of the two gaps.

The cluster size is also plotted in Figure 2.8, with the relative scale on the right side. The cluster size is the average number of adjacent physical strips around the particle track giving a signal over threshold. It measures the cross-talk, that is the spacial resolution of the detector. Because in the Muon system regions supposed to be covered by RPCs one logical pad is at least formed by two physical strips,

a cluster size less than 2 was the requirement to not deteriorate the momentum resolution of the Muon system. This requirement was met by the RPC prototype.

These detectors had proved that the Muon system requirements may thus be fulfilled, concerning the efficiency, the spatial resolution and the time resolutions (see for example [33]).

Once the intrinsic performances of the detector has been proved to completely fulfill the efficiency, the spatial resolution and the time resolution needs of the Muon system, the successive step has been the verification of the rate capability and especially of the ageing properties of the RPCs. An extensive aging test has then been performed, whose details will be broadly discussed in the next chapter. As we shall see, the results of the test have not been affirmative, as the RPCs have unambiguously shown to suffer aging, exhibiting an increase of the electrode resistivity, leading to a degeneration of the rate capability.

The technology has then been abandoned, and the RPC part of the Muon system is going to be covered by Multiwire Proportional Chambers, which already were used for the innermost regions. The flexible design of the Muon system has allowed to substitute the technology without major efforts, since the RPCs had already been planned with the same dimensions and the same physical pad layout of the MWPC.

The work of this thesis represents a sort of summary about the aging research on the Resistive Plate Chambers for LHCb.

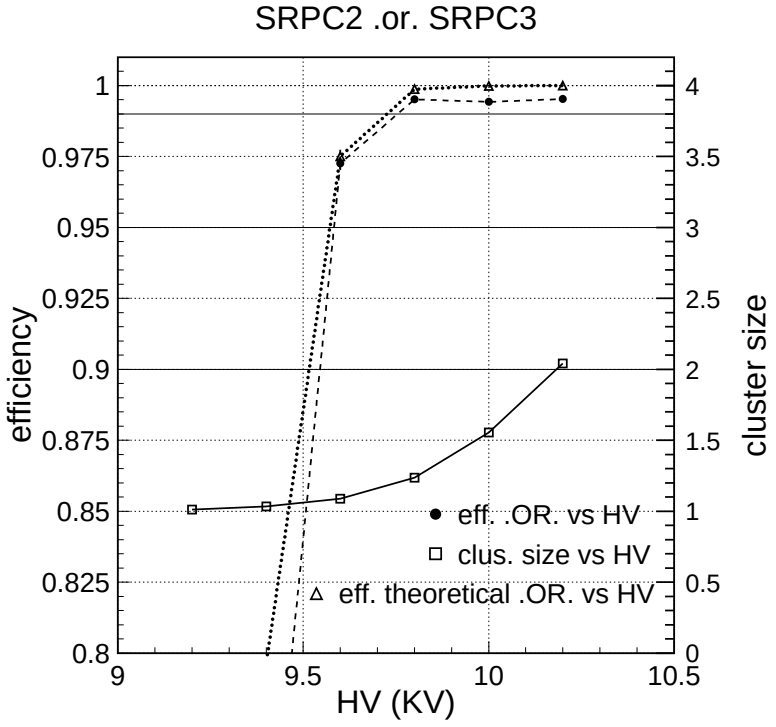

Figure 2.8: Efficiency and cluster size for the OR of two single-gap RPC.

Chapter 3

Aging characteristics of the Resistive Plate Chambers

3.1 Introduction

The forthcoming LHC experiments represent a hard challenge for all the detector technologies, including Resistive Plate Chambers. RPCs are widely used in high energy physics experiments, in particular for the muon triggering, which requires fast time response and large coverage area, for which RPCs represent a very suited solution. In order to get these detectors standing the very large particle flux density of a hadron collider (up to few kHz/cm^2), in the last decade many efforts have been done to improve their rate capability (see [35, 36, 37]). This has been partially achieved by operating in avalanche mode, rather than streamer mode, since the reduction of the gas gain leads to a faster recharge time. The other important parameter affecting the rate capability is the volume resistivity of the electrodes. Materials like glasses, with typical resistivity around 10^{12} Ωcm, result in small rate capabilities. Phenolic bakelite electrodes, which can be produced with resistivity as low as 10^9 Ωcm, are used in detectors working at high rate [38, 39, 40].

In LHCb the rate capability requirement is even more stringent respect to the other experiments. In particular the particle rates expected in the Muon System (see Table 2.1) are significantly larger than those expected in the corresponding sub-detectors in ATLAS and CMS.

The rate capability of a RPC is determined by the volume resistivity ρ of the electrodes and scales roughly as $1/\rho$, as we shall see in section 3.3. Variations of the electrode resistivity affect directly the rate capability of the RPC: it is therefore very important to be able to monitor this parameter during the chamber operation. Possible variations can be due to changes in environmental parameters like temperature and humidity[41, 42] or to aging effects.

In this chapter the performances of two RPC detectors under high radiation conditions will be reported as they have been measured along their whole life, from the building in 1999 to the end of the aging test in spring 2003. Some pecu-

liar characteristics exhibited in such environment will be remarked and explained within a simple model.

3.2 Detector characteristics

Two identical chambers had been built in 1999 to study the response of RPCs in the high background conditions foreseen at LHCb, and to verify their aging properties. The detectors are two Single-gap RPCs, with 2 mm gas gap and 2

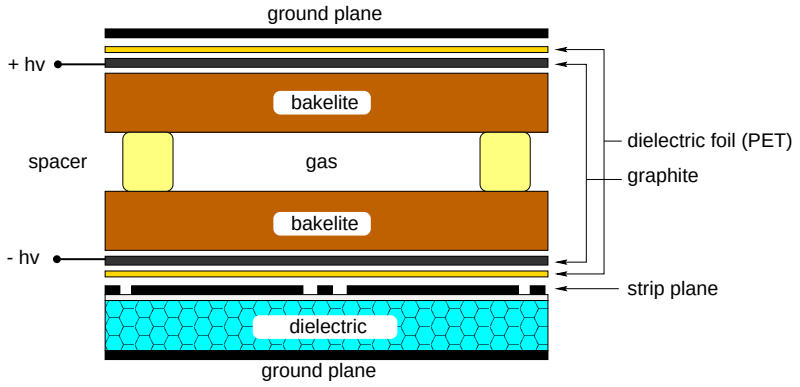

Figure 3.1: Layout of a RPC detector.

mm thick electrodes plates, made of phenolic bakelite (Figure 3.1). The nominal nominal bakelite resistivity was $\sim 10^{10}$ Ωcm. It was opportunely chosen not too high (typical values are $10^{11} - 10^{12}$) in order to achieve high rate capability.

The internal surface of the electrodes is treated with linseed oil, to smooth any possible disuniformity which would distort the electric field. The high voltage is applied to the external surface of the electrodes through a painted graphite film, with a superficial resistance of $\sim$ 200 k$\Omega/\Box$, dielectrically isolated by a 200 μm PET foil from the environment. The distance between electrodes is maintained by polycarbonate spacers, 1 cm diameter, dislocated on an square array with 10 cm pitch. All around the detector the gap is closed by a polycarbonate frame, glued on the electrodes.

The sensitive area of both chambers is 50×50 cm^2 . The detectors operated in avalanche mode with a 95% $C_2H_2F_4$, 4% i-C_4H_{10} and 1% SF_6 gas mixture, usually fluxed at a rate of about 1 l/h. The signals are inductively readout by an external copper plane, segmented in 3 cm wide strips. On one detector (called in the following RPC A) the strip plane has been cut in two along its length, so that the final strip size is 3×25 cm^2 , while on the other detector (RPC B) it was 3×50 cm^2 . The electronics consisted in fast voltage amplifiers with gain of 300, directly coupled to the strips.

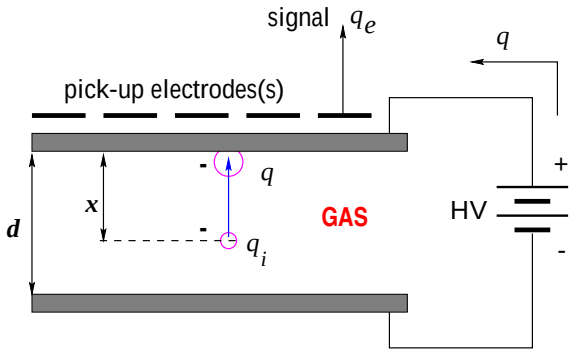

Figure 3.2: Principle of signal formation in a RPC.

3.2.1 Operating principle of the RPC

When a charged particle ionizes the gas of the RPC, an avalanche is formed by multiplication in the gas if the electric field is sufficiently high (see Figure 3.2) . The avalanche charge q, is collected by the anode and produces an inducted charge q_e on the external readout electrode, representing the prompt singal of the RPC.

The avalanche charge q, is related to the ionization charge q_i, via the gain:

$$q = Gq_i$$

G depends strongly on the electric field and on the distance of the primary ionization cluster from the anode x.

It shows a double-regime behavior respect to some threshold voltage V_T: if the potential V_{gap} across the gas gap is below V_T, G tends rapidly to unity, and no multiplication occurs; if otherwise $V_{\text{gap}} > V_T$, G increases rapidly with voltage, entering in the avalanche regime. The value of V_T depends on several variables, either constructive or environmental, like the gap width, the gas composition, and the gas temperature and pressure.

It is known that in order to operate in avalanche mode G should not exceed the limit value $G_{max} \approx 10^7$. Anyway space-charge effects can limit the growth of the avalanche charge to a saturation value [43] increasing linearly with V_{gap}, so that

$$q \propto V_{\text{gap}} - V_T$$

This effect is more evident in gas mixtures containing quenching gases with high electron affinity that suppress the streamer formation [44], such as SF_6 in our case.

3.3 Rate Capability

The rate capability represents a fundamental parameter for all the detectors employed on accelerator beam experiments. It determines the intensity of the radiation background that a given detector can stand, still reaching full efficiency in the

particle detection. As already said in section 2.5 the LHCb Muon system is particularly sensible to even small variations of the chamber efficiency ϵ_{cham}, because the trigger uses all the five stations, so that its efficiency results to be $\epsilon_{trig} = (\epsilon_{cham})^5$. For that reason a single chamber is constituted by 2 sensible planes in the case of RPCs and 4 in the case of MWPC.

The use of resistive electrodes in RPCs, on one hand assures that the surface discharged by the avalanche remains limited, in order to achieve a good spacial resolution, but on the other hand it increases the recharge time, leaving that part of the electrode blind and decreasing the rate capability.

A simple model [33] which schematizes the RPC as a series of three plane capacitors gives a formula relating the electrode resistivity to the maximum particle flux a RPC can stand:

$$\Phi_{max} = \left(1 + \frac{2}{\epsilon_r}\right)^{-2} \frac{E}{\epsilon_r q \rho}$$

where ϵ_r is the electrode relative dielectric constant ($\sim$ 5 in the case of phenolic bakelite), E is the electric field inside the gas gap (typically of the order of 5 kV/mm), q is the avalanche charge (30 pC may be considered a reasonable value for low energy ionizing particles) and ρ is the electrode resistivity. Plugging all the numbers in the formula one finds a maximal rate capability of about 15 kHz/cm^2 , to be considered as limit for the operation of the RPC.

Since the rate capability and the electrode resistivity are so closely related, if we want to test the efficiency performances of the detectors at high particle rates, we have to monitor the bakelite resistivity.

3.4 Experimental setup at GIF

All the tests presented in this chapter have been performed at the *Gamma Irradiation Facility* (GIF) [45], the experimental area provided by CERN, used to test the LHC detectors under very high background conditions, by means of an intense photon flux. The conditions of the GIF are likely to be very similar to those that will be encountered in the experiment on the beam, with a diffuse and low energy photon gas. The photons of the GIF are produced by a ^{137}Cs radioactive source (662 keV nuclear dis-excitation; 30.2 y half-life; 740 GBq at March 1997) and are collimated by lead filters within a solid angle of $74^o \times 74^o$. Further remote-controlled lead planes allow to tune the photon flux within a four orders of magnitude range. A total of 17 values can be set for the absorption factor, from Abs=1 to Abs=10000 (Abs=∞ means source off). The filters also make the flux uniform on a plane surface parallel to the source.

To perform efficiency measurements the GIF area is reached by a low-energy muon beam arising from the dump of the X5 proton beam of the SPS (see Figure 3.3).

The experimental setup is schematically shown in Figure 3.4. The position 1 is the main irradiation position, very close to the source ($\sim$ 55 cm), where

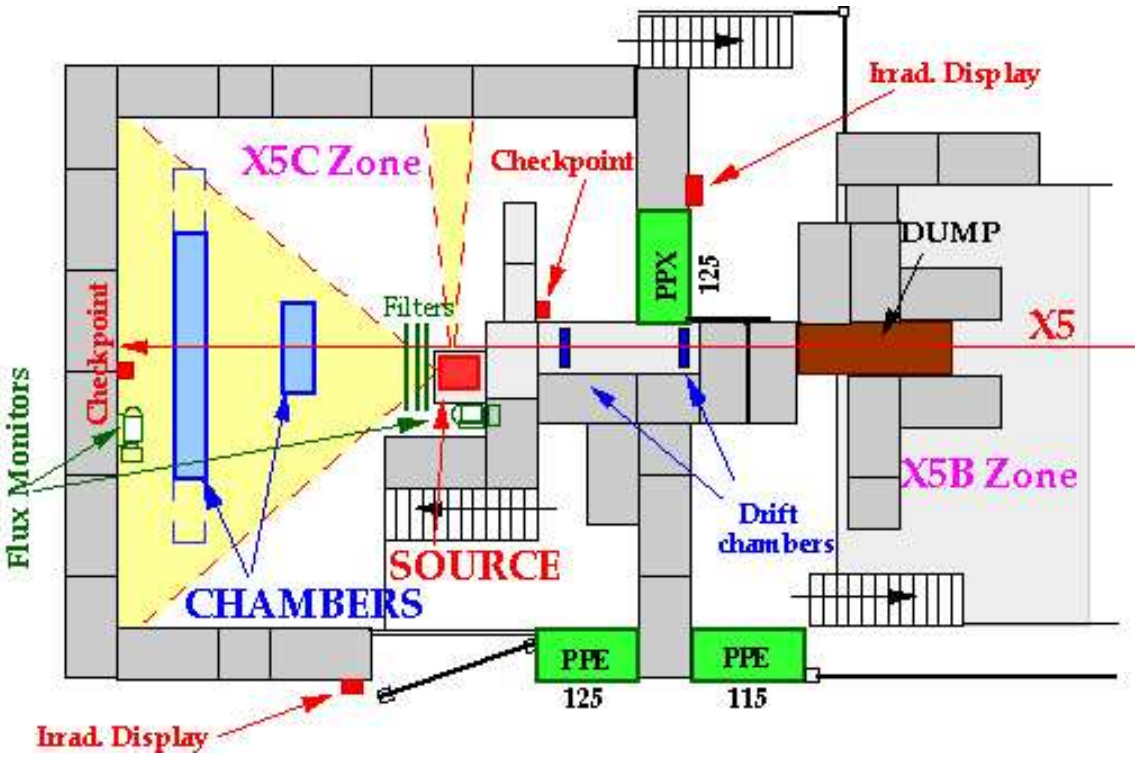

Figure 3.3: Schema of the GIF. The X5 proton beam coming from SPS is dumped, and the surviving low energy muons reach the irradiated area ($\sim$ 150 m^2).

the detectors were placed in order to be continuously exposed to a large flux of radiation.

In particular here the two chambers prepared for the aging test (RPC A and RPC B) have been installed for about two years. Only during the first part of the aging test the RPC B was used as a reference chamber, and was fixed on the side concrete wall (position 2), outside the photon cone. Later this detector too was moved just behind the other in the high-radiation position. Position 3 is the test-beam position. The X5 muon beam passes aside of the source, hence in order to be hit the detectors had to be placed in this position, a little farther from the source, though still remaining inside the radiation acceptance.

In Figure 3.4 are also shown the telescope of scintillators counters, providing the trigger, and the hodoscope, measuring the particle position ($x - y$) with an accuracy better than 1 cm, used to perform efficiency measurements.

3.4.1 Photon spectrum and filter calibration

The total photon spectrum of GIF source is composed by a direct component at 662 keV and an indirect component, due to scattering with the lead filters ($E_\gamma >$ 180 keV), the albedo from the concrete walls ($E_\gamma <$ 400 keV) and Pb induced fluorescence ($E_\gamma = 85$ keV) (see Figure 3.5).

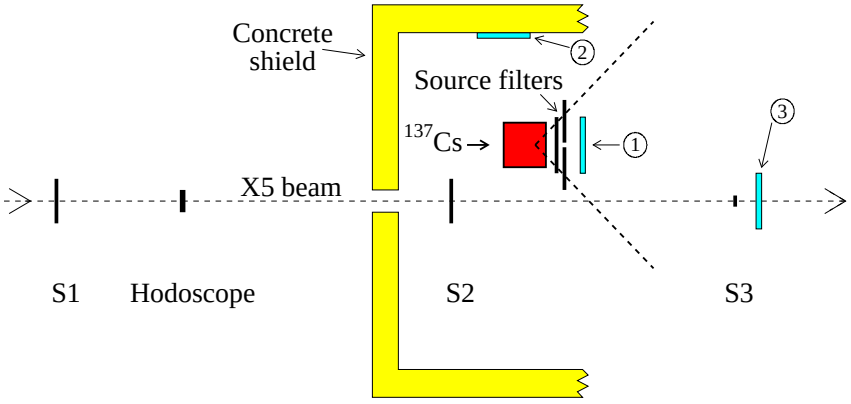

Figure 3.4: Schematic view of the test setup. The positions of the RPCs corresponding to the various measurements are indicated (1-3). The scintillator counters (S1-S3 and the Hodoscope) were used for measuring the RPC efficiency with the particle beam.

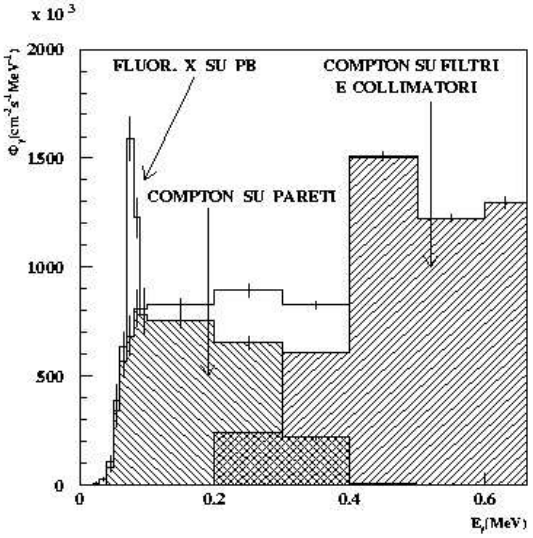

Figure 3.5: Simulation results of the photon spectrum for a distance of 155 cm from the source and an absorption factor Abs=1[46].

Table 3.1: Photon flux for different source distances at Abs=1[46].

Distance (cm)	Direct radiation flux (Hz/cm^2)	Total radiation flux (Hz/cm^2)
50	0.79×10^7 ($\pm$ 0.2%)	0.12×10^8 ($\pm$ 0.2%)
155	0.80×10^6 ($\pm$ 0.6%)	0.14×10^7 ($\pm$ 0.5%)
300	0.22×10^6 ($\pm$ 0.6%)	0.45×10^6 ($\pm$ 0.5%)
400	0.12×10^6 ($\pm$ 0.4%)	0.28×10^6 ($\pm$ 0.5%)

The maximum (Abs=1) photon flux at different distances is reported in Table 3.4.1, for direct radiation (E_γ = 662 keV) and for total radiation ($E_\gamma \leq$ 662 keV). The intensity scales quadratically with the distance.

In comparing the model with the data it is very important to accurately know the relative absorption factors (Abs) of the various GIF filters. Only the direct radiation depends linearly to 1/Abs, while the total radiation (direct plus diffuse) rather follows a power law of the kind $\Phi_\gamma \propto (1/\text{Abs})^{-\beta}$. Since the exponent could depend on the effective energy spectrum of the photons for the detector under study, we calibrated the filters directly measuring the hit rate of a RPC.

The particle rate is measured as a function of the high voltage (see Figure 3.6) and the plateau value is taken as the reference value for the given absorption factor. The rate has been corrected taking into account the contribution to the cluster-size due to the photons, which has been disentangled from that due to the beam thanks to time considerations [47].

Table 3.2 reports the particle rates for each of the GIF nominal absorption factors, measured at $\sim$ 80 cm from the source, during the 2002 test-beam.

Table 3.2: Measured particle rates for each GIF Absorption factor, for a RPC set at $\sim$ 80 cm from the source (see Figure 3.23).

Absorption factor	250	100	50	20	10	5	2	1
Rate (Hz/cm^2)	50	125	210	390	520	980	1850	3000

An older measurement is shown in Figure 3.7, used to exctract the β coefficient from the fit. It gives the value $\beta = 0.71 \pm 0.01$.

Note that the detector count rates are several orders of magnitude lower than the photon rates shown in Table 3.4.1. This is because the RPC is able to detect only a small fraction of photons, namely those which convert in charged particle capable to ionize the gas.

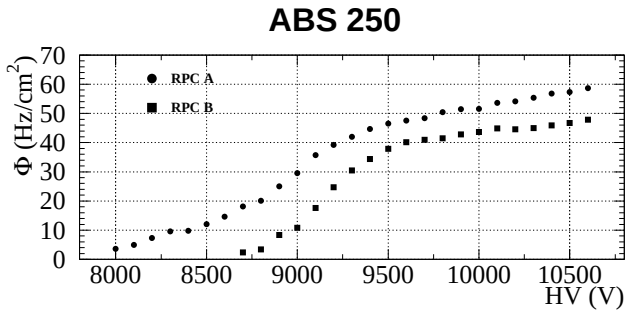

Figure 3.6: Particle flux as a function of high voltage for a source absorption factor 250.

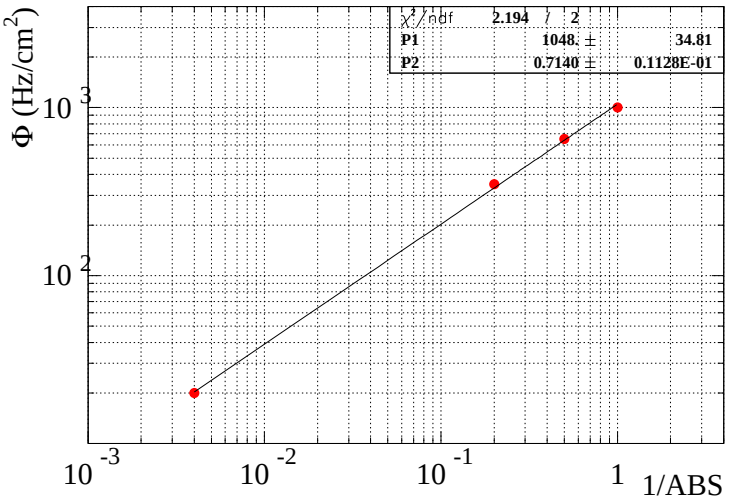

Figure 3.7: Particle flux as a function of the inverse nominal source absorption factor. The fit gives $\beta = 0.71 \pm 0.01$.

To better understand how the conversion happens in a RPC, consider that at the typical GIF energies the most probable interaction process for photons is the Compton scattering. If $h\nu$ is the photon energy, the scattered electron will have a maximum energy of

$$T_{max} = h\nu \left(\frac{2\gamma}{1+2\gamma} \right)$$

where

$$\gamma = \frac{h\nu}{m_e c^2}$$

Hence, a 662 keV photon will extract an electron with a maximum energy of 478 keV. The range of this electron in bakelite being only 1.5 mm [48], it is clear

how only the photons converting inside the resistive electrode (2 mm thick) will produce electrons able to reach the gas gap and ionize the gas. We can estimate the conversion effciency of the RPCs for the GIF photons through the equation:

$$\epsilon_\gamma = \frac{\Phi}{\Phi_\gamma \cdot \omega_{src}} = \frac{3 \text{ kHz/cm}^2}{0.47 \times 10^7 \text{ Hz/cm}^2 \cdot 0.91} = 0.7 \times 10^{-3}$$

where Φ_γ is the source photon flux, Φ is the measured particle rate, and ω_{src} is a factor to scale the source activity from 1997 (when the data were computed) to 2001. The found value is in agreement with previous estimations [49].

3.5 Performance of RPCs before aging

The first test-beam at the GIF was held in October 1999. In this test there were the RPC A and another Double-gap RPC, of whom RPC B constituted one of the two active layers. In Figure 3.8 are shown the results. The efficiencies are plotted as a function of the high voltage for different values of the absorption factors, corresponding to measured particle rates of 2 kHz/cm^2 , 5 kHz/cm^2 and 10 kHz/cm^2 .

The Single-gap (RPC A) begins to suffer the particle rate at the largest value of 10 kHz/cm^2 , where a smoothing of the plateau is visible. The Double-gap, on the other hand does not present any change up the maximal rate.

After this test the Double-gap was dismounted and only one gap kept to make the Single-gap RPC B. These two detectors have been installed permanentely at the GIF from the beginning of 2001. All the results will refer to them in the following.

3.6 Behavior of RPCs at the GIF

During the irradiation test at the GIF has been observed that the current drawn by a RPC detector subject to a high particle flux, presents some peculiar characteristics:

- it depends linearly on the applied voltage, above a certain threshold;
- it saturates with increasing flux values;
- it depends exponentially from the temperature for a fixed applied voltage.

We have tried to explain these features with a phenomenological model based on few simple physics assumptions. The most important result of the model is to furnish a method to measure the resistivity of electrodes [50].

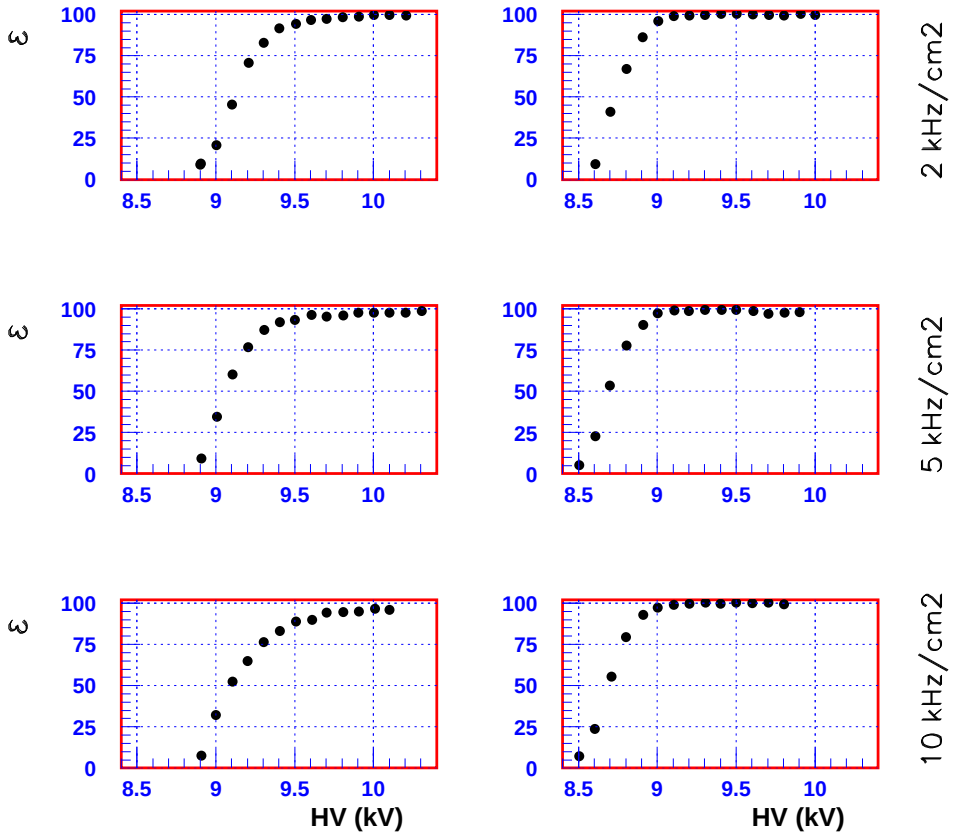

Figure 3.8: The efficiency as a function of HV for Singe-gap RPC (left) and a Double-gap RPC (right) measured in October 1999 at the GIF, with background rates up to 10 KHz/cm^2 .

3.7 The model

The current drawn by a RPC exposed to a particle flux Φ (particles/s) can be achieved from the avalanche charge:

$$I = \Phi\ q = \Phi\ G\ q_i \tag{3.1}$$

Of course if Φ refers to neutral particles one must take into account their detection efficiency, i.e. the probability of releasing one or more electrons in the gas (of the order 10^{-3} for RPC exposed to GIF photons).

The basilar hypothesis the model is based upon, is that all the physical properties of the detector must depend on the effective voltage across the gas gap $V_{\rm gap}$ (see Figure 3.9). This results to be the external voltage V_0 provided by the power supply, minus the voltage drop inside the resistive plates, which can be argued by

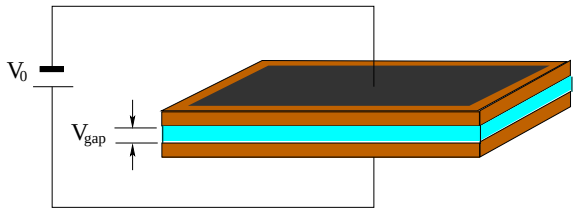

Figure 3.9: V_{gap} is the voltage drop on the gas gap, while V_0 is the external applied voltage.

means of the Ohm's law:

$$V_{\text{gap}} = V_0 - I\,R \tag{3.2}$$

where I is the steady current flowing in the electrodes and R their total resistance.

For a typical RPC the main contribution to this resistance is the bulk resistivity ρ of the phenolic bakelite, to which it is related by the second Ohm's law:

$$R = \rho\,\frac{d}{S}$$

where d is the global thickness of the plates an S their surface. In fact the graphite film on one side and the oil on the other are too thin to appreciably contribute to the volume resistivity.

The drop inside highly resistive electrodes can be quite important if the current flowing through the RPC is large enough, so that V_{gap} is not directly measurable.

Figure 3.10 shows the avalanche charge measured in a RPC as a function of the applied voltage V_0. In this case the measurement has been done with cosmic rays, so that the particle flux is very low, the voltage drop across the electrodes is negligible and $V_{\text{gap}} \approx V_0$. On the same plot the current has been superimposed, to show the proportionality with the charge, expected from Equation 3.1. It is seen that above the knee of the curve, representing the threshold value V_T, both the charge and the current grow linearly with V_{gap}, which is an indication of the saturation effect.

Note that also below the knee the current increases almost linearly with a much gentler slope. This is the dark current contribution, due mainly to leak through the spacers and the frame, and has not been considered in the model.

The particular double-regime behavior of the $I - V_{\text{gap}}$ curve can be modeled at a first order of approximation by a linear function with a discontinuity of the derivative in the threshold value V_T (θ is the unit step function):

$$I(V_{\text{gap}}) = a\;\theta(V_{\text{gap}} - V_T)(V_{\text{gap}} - V_T) \tag{3.3}$$

where a is a normalization factor proportional to the particle flux.

To turn into a more realistic description we can think that the value of V_T, which depends for example on the thickness of the gas gap, slightly varies in different points of the detector, because of some local disuniformities. So the expression

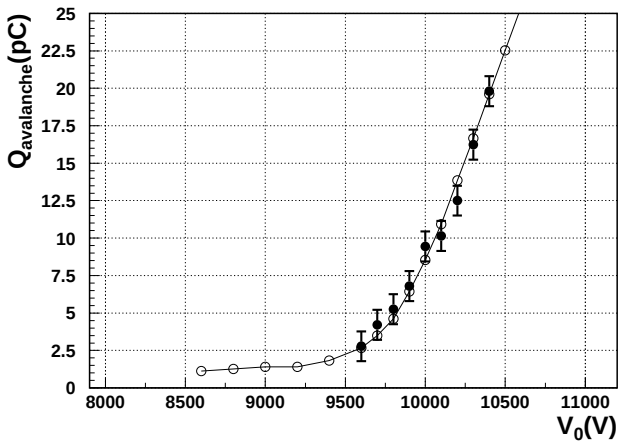

Figure 3.10: Solid circles: avalanche charge vs. V_0, measured with cosmic rays. Open circles: current (arbitrary scale) measured with low particle flux. In both cases $V_{\rm gap} \approx V_0$. RPC operated with $C_2H_2F_4$, i-C_4H_{10} and SF_6 mixture in 95:4:1 proportion.

(3.3) can be folded with a Gaussian distribution of V_T:

$$I(V_{\rm gap}) = a \left\{ \frac{\sigma_T}{\sqrt{2\pi}}\, e^{-\frac{(V_{\rm gap}-\overline{V}_T)^2}{2\sigma_T^2}} + \frac{1}{2}(V_{\rm gap}-\overline{V}_T)\left[1+\mathrm{erf}\left(\frac{V_{\rm gap}-\overline{V}_T}{\sqrt{2}\sigma_T}\right)\right]\right\} \qquad (3.4)$$

where $\overline{V}_T$ is the average value and σ_T the rms spread of V_T.

For $V_{\rm gap} \gg \overline{V}_T$ this function becomes simply $I = a(V_{\rm gap} - \overline{V}_T)$. A fit of Equation (3.4) to the data is presented in Figure 3.11, showing an excellent agreement. The relative spread $\sigma_T/\overline{V}_T$ is typically 3% to 4% in the detectors tested. The fact that it varies, though slightly, from detector to detector, confirms that geometric effects could also contribute to the spread.

3.7.1 Limit case

Consider now a detector exposed to a large and uniform particle flux, as the flux of photons from GIF. When the current drawn by the detector increases, the voltage drop in the plates is relevant and the condition $V_{\rm gap} \approx V_0$ is no more valid, as $V_{\rm gap}$ begins to displace from V_0. Considering 15 pC as a typical value for the avalanche charge (from Figure 3.10) and assuming 2 mm thick electrodes with 10^{11} Ωcm resistivity, we can compute from Eq. (3.2) that for particle flux densities of 170 Hz/cm^2 there is 100 V difference between $V_{\rm gap}$ and V_0.

The more the flux increases the more $V_{\rm gap}$ shifts from V_0, towards the minimum threshold value V_T. In the limit of infinite flux the avalanche charge must becomes very small in order to keep the current finite; in other words the gap voltage decreases to the minimum value at which no multiplication occurs and the RPC is

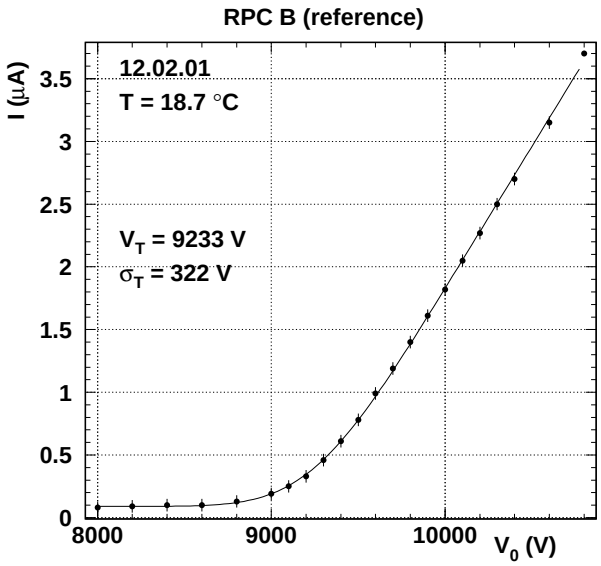

Figure 3.11: RPC current vs. V_0 measured with low particle flux ($V_{\text{gap}} \approx V_0$) and fitted with the function (3.4).

"turn off". We have

$$V_{\text{gap}} \to V_T \qquad \text{for} \qquad \Phi \to \infty$$

In this limit we can derive from Eq. (3.2) the value of the current:

$$I = I_{\text{max}} = \frac{V_0 - V_T}{R} \tag{3.5}$$

This represents the central equation of the model, showing how under high flux condition the RPC current depends linearly on the applied voltage V_0 and saturates to a maximum value I_{max} independent from the flux Φ. Note that the saturation is a consequence of a negative feedback effect on the current: the more the current increases the more the electrode resistance rises, so that the effective voltage across the gap drops, reducing the gas gain and the current itself.

It is remarkable that the linear coefficient between the current I and the applied voltage V_0 is the inverse of the electrode resistance R. Since the properties of the gas mixture and the gap width only enter via V_T, they do not affect the slope of the $I - V_0$ curve. Hence from the measurement of the $I - V_0$ characteristic curve in high radiation conditions one can extract R and can easily monitor its variations.

We stress here that the linearity of Eq. (3.5) is based only on the general assumption of the presence of a sharp threshold effect in the avalanche evolution. In particular, it has no relation with the linear dependence of the avalanche charge on V_{gap} (Figure 3.10), and also holds in a regime of non saturated avalanche.

3.7.2 General case

Eq. (3.5) can be generalized for arbitrary flux values: using Eq. (3.2) and Eq. (3.3), one has for $V_0 > V_T$:

$$I = \left(\frac{aR}{1+aR}\right)\ \frac{V_0 - V_T}{R} = \left(\frac{X}{1+X}\right)\ \frac{V_0 - V_T}{R} = \frac{V_0 - V_T}{R_{\text{eff}}} \tag{3.6}$$

where an effective resistance R_{eff} has been defined:

$$R_{\text{eff}} = R\ \left(\frac{1+X}{X}\right)$$

The parameter $X = aR$ controls the deviations from the simple proportionality between the current and the flux. Since $a \propto \Phi$, this causes the current to saturate at I_{max} for large values of the flux, when X becomes large. The saturation is most readily achieved for detectors of large resistance, where the internal voltage drop IR may attain values of hundreds of volts at relatively small flux. By including in Eq. (3.6) the spread in V_T we obtain

$$I(V_0) = \frac{1}{R_{\text{eff}}}\left\{\frac{\sigma_T}{\sqrt{2\pi}}\ e^{-\frac{(V_0-\overline{V}_T)^2}{2\sigma_T^2}} + \frac{1}{2}(V_0 - \overline{V}_T)\left[1 + \text{erf}\left(\frac{V_0 - \overline{V}_T}{\sqrt{2}\sigma_T}\right)\right]\right\} \tag{3.7}$$

This formula represents the operational method furnished by the model to measure the bakelite resistance of the RPC. It will be used in the following to fit the $I - V_0$ curve, and in particular to extract R_{eff} from its slope.

To compute the true resistance R from R_{eff}, the value of X is also necessary. If X is *a priori* known to be large, the correction can be neglected. Otherwise, X must be obtained by fitting the current at different values of the flux.

It is important to underline that due to the factor $X/(1+X)$, if X is large, a simple estimate can be sufficient: the correction introduces in fact only a very small uncertainty on R. So the method works better under high-flux conditions and for large resistance values, since in this case $X \gg 1$.

We have seen how the Eq. (3.2) and its generalized version Eq. (3.6) account for the first two characteristics of a RPC under high flux conditions, enumerated in Section 3.6. Nevertheless the same relations also make an explicit prediction about the dependence of the current on the temperature. Since we expect that the variation of V_T with temperature would be negligible, the dominant effect on I comes from the exponential dependence of the phenolic plates resistivity on the temperature. Hence the model gives a simple way to correct experimental data for temperature effects.

Finally we want to remark that this method allows to measure the resistivity of a RPC in a non-destructive way, during chamber operation. It only requires the detector to be exposed to high radiation environment. Thus it turns out to be very useful for the periodical monitoring of the bakelite properties required by the aging test.

3.8 Comparison with data

3.8.1 Current versus photon flux

The study of the current dependence upon flux has been performed by placing the detectors close to the source, in position 1. Figure 3.12 shows the current of RPC A, measured at several filter absorption factors, for two different values of the applied voltage V_0 (10000 and 10800 V) well above the threshold voltage V_T. The nominal filter absorption of the source was varied between 1 and 10^4. Saturation is evident already at low flux values (Abs$^{-1} \approx 10^{-3}$).

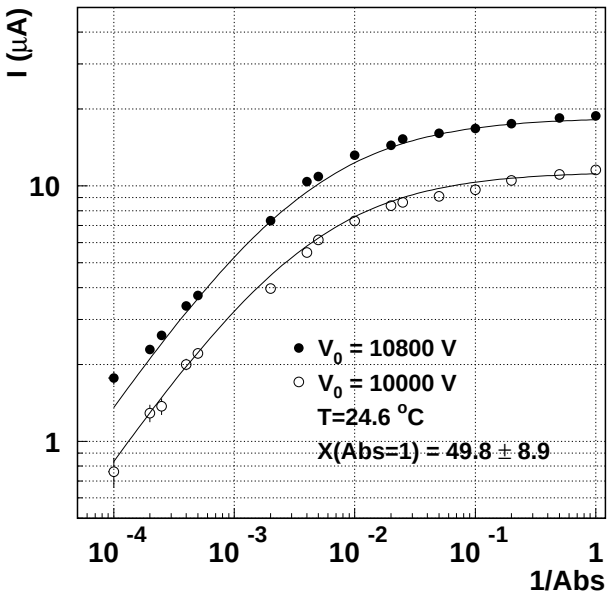

Figure 3.12: RPC current measured at fixed V_0 (10800 V, solid circles; 10000 V, open circles), plotted against the inverse of the nominal source absorption factor. The curves are the predictions of the model.

Considering that the dependence of the flux from the source absorption factor is $\Phi(\text{Abs}) = \Phi(1)^{-\beta}$, and that $X \propto \Phi$, from Eq. (3.6) one has

$$I(\text{Abs}) = I(1)\frac{1 + X(1)}{\text{Abs}^{\beta} + X(1)} \tag{3.8}$$

This relationship was used to fit the data of the current versus the inverse of the absorption factor, using the value of $\beta = 0.7$ obtained from Figure 3.7, and $X(\text{Abs}{=}1)$ as a free parameter. We obtained

$$X(1) = 49.8 \pm 8.9$$

leading to a saturation of 98%. This implies only a minor correction to the resistance value, so that one can consider $R_{\text{eff}} \approx R$.

As expected, X was smaller at larger distances from the source, since it decreases proportionally to the flux. Going from ~ 55 cm to ~ 140 cm the saturation corrections became as low as 75%. For that reason, the resistivity measurements were normally taken at the minimum possible distance, about 55 cm.

Note that the data of Figure 3.12 are in very good agreement with the model over almost three orders of magnitude on the flux.

3.8.2 Resistance measurements

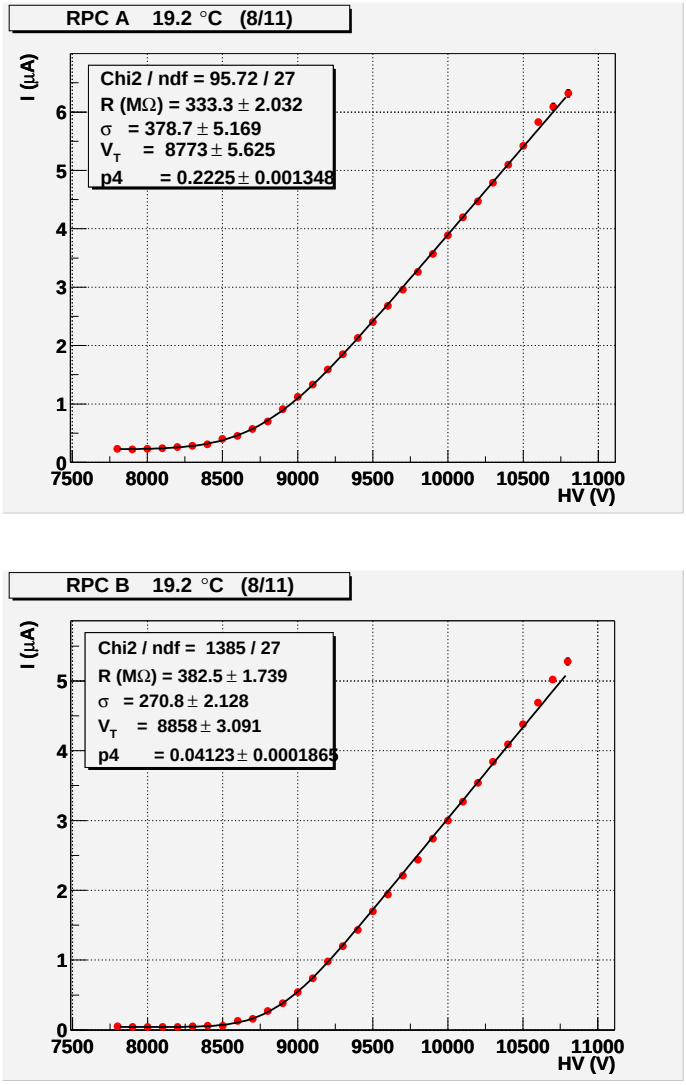

Figure 3.13: Current vs. V_0 for RPC A (top) and RPC (bottom) for source nominal absorption factor 1. The fitting function is Eq. (3.7).

Typical $I - V_0$ curves taken for minimum GIF absorption factors (Abs=1) are

shown in Figure 3.13 for the two detectors under test. A perfect linearity is observed above a certain threshold voltage. The curves are fitted by Eq. (3.7) and the resistance R_{eff}, the average threshold voltage $\overline{V}_T$ and its rms σ_T are extracted. Note that the resistance can be simply obtained by the slope of the linear part of the curve

$$(R_{\text{eff}})^{-1} = \frac{\Delta I}{\Delta V_0}$$

In this particular example, referring to the end of the aging test, the two detectors have large resistance of few hundreds of MΩ, conducing to resistivity around $4 \cdot 10^{12}$ Ωcm. Due to this large resistance and to the high radiation flux, the saturation value was very close to 1, so that the computed R_{eff} can be safely approximated with the real R.

We want to recall here that since the main contribution to the resistivity of the electrodes is given by the phenolic resin, the resistance measured can be considered as the bakelite bulk resistance.

3.8.3 Efficiency measurements

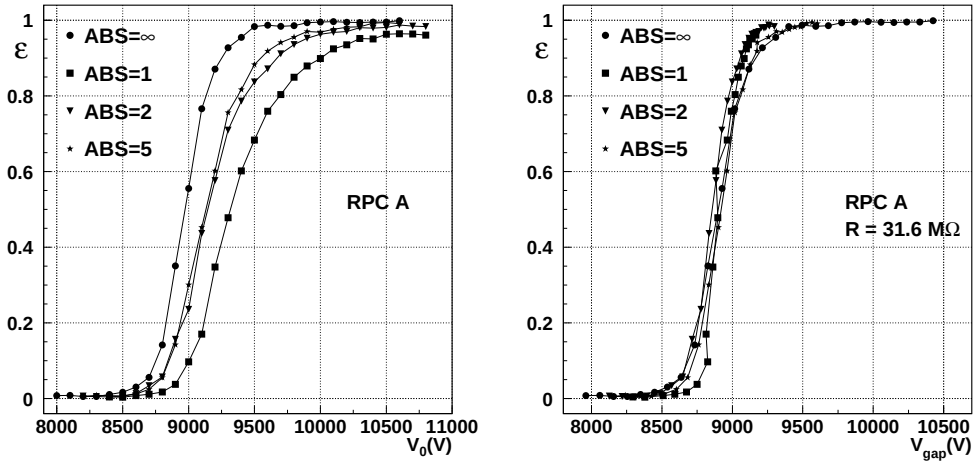

Figure 3.14: Efficiency of RPC A for different absorption factors. On the left the data are plotted vs. V_0. On the right they are plotted vs. $V_{\text{gap}} = V_0 - IR$ using the value of R determined by the model.

The model is based on the hypothesis that all the physical properties of a RPC depend on V_{gap}, including the detection efficiency of the detector. This guess had already been used elsewhere to extract R from efficiency curves [51, 52, 53]. Now we want to interpret the efficiency curves of RPCs for minimum ionizing particles (MIPs) using the values of R obtained by the method presented, in order to get a further validation.

Measuring the MIP efficiency as a function of V_0 in presence of a large photon background rate from the GIF, several curves for different absorption factors are

obtained (Figure 3.14, left). On the other hand, when the efficiency is plotted as a function of $V_{\text{gap}} = V_0 - IR$, using the value of R determined by our model, the curves join as expected (Figure 3.14, right).

This represents a strong cross-check which further validate the model, since the resistance found by the $I - V_0$ curve and that found by making the efficiency independent from the flux are two uncorrelated measurements.

3.8.4 Argon based measurements

We want now to remark that the presence of a high background radiation is not mandatory for the validity of the model. The only condition needed is that the current flowing through the electrodes is large enough to create a sensible voltage drop and to originates the negative feedback effect. This can be produced either by an intense external radiation source, or by a particularly ionizable gas. As a prove a test has been made by fluxing a RPC with pure argon, and measuring the current as a function of the high voltage, with no radiation present. The curve is plotted in Figure 3.15, showing a perfect linearity above the threshold.

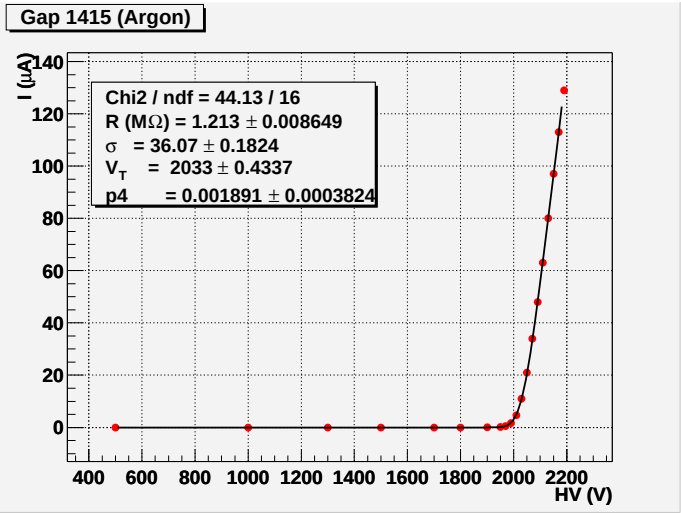

Figure 3.15: I-V curve for a 150×30 cm^2 RPC fluxed with pure argon. The fitting function is Eq. (3.7).

The data are well fitted by Eq. (3.7), the function predicted by the model. The comparison with standard curves of Figure 3.13 exhibits a much lower threshold voltage (2033 V for argon against 8800 V) and a much sharper transition to avalanche regime ($\sigma/V_T = 1.8\%$ for argon against $\sigma/V_T = 4\%$ for standard mixture). Considering that the dimension of the detector in this case were 150×30 cm^2 , the resistivity is computed to be $\rho = \ 1.35 \times 10^{10}$ Ωcm, a value in agreement with the building specification.

3.8.5 Temperature effects

Under the assumption that the RPC plates resistance is due to the bakelite, the temperature dependence of the RPC resistivity should be the same as for bakelite bulk resistivity, i.e. it should have the form:

$$R \approx R_{20} \exp\left[\alpha(\theta_{20} - \theta)\right] \tag{3.9}$$

where θ is the temperature in $^{\circ}\mathrm{C}$ and $\theta_{20} = 20\ ^{\circ}\mathrm{C}$ is the reference temperature. Measuring directly the bulk resistivity on three different bakelite samples we obtained $\alpha = 0.12 \pm 0.01$

In Figure 3.16, the measurements of the resistance of RPC A and B are shown as a function of the temperature. An exponential fit of these data gives a temperature coefficient

$$\langle\alpha\rangle = 0.126 \pm 0.008$$

in nice agreement with that of the bakelite itself. This represents another clear hint that we are really measuring the volume resistivity of the bakelite.

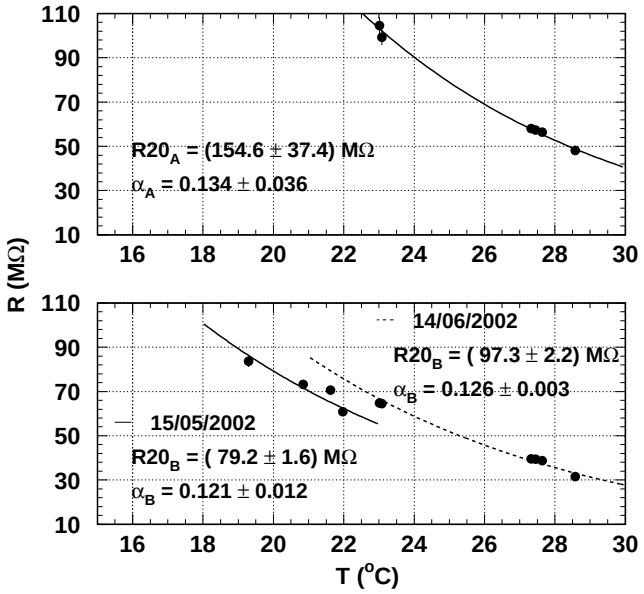

Figure 3.16: Resistances of RPC A and B plotted versus temperature. The temperature coefficient α is fitted using the exponential function.

As observed above, Eq. (3.6) allows to correct the RPC current measurements for temperature effects, that are introduced through R, allowing an unambiguous normalization of the current itself, for example at 20 $^{\circ}\mathrm{C}$. This is shown in Figure 3.17, where the effect of 24-h temperature oscillations is almost completely corrected.

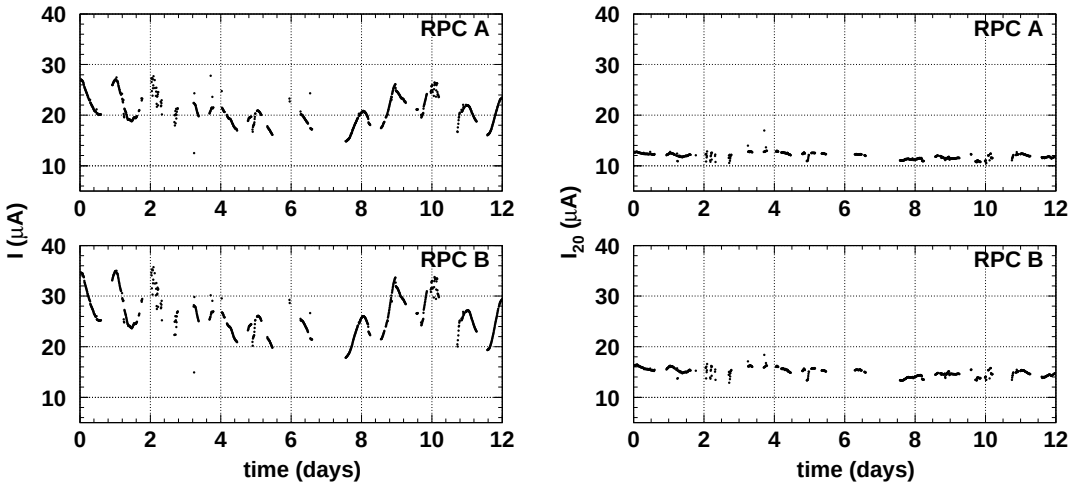

Figure 3.17: Time evolution of currents for RPC A and B under GIF irradiation. Raw currents are on the left, showing typical daily oscillations. The corrected currents at 20 °C are on the right.

3.9 Current versus time

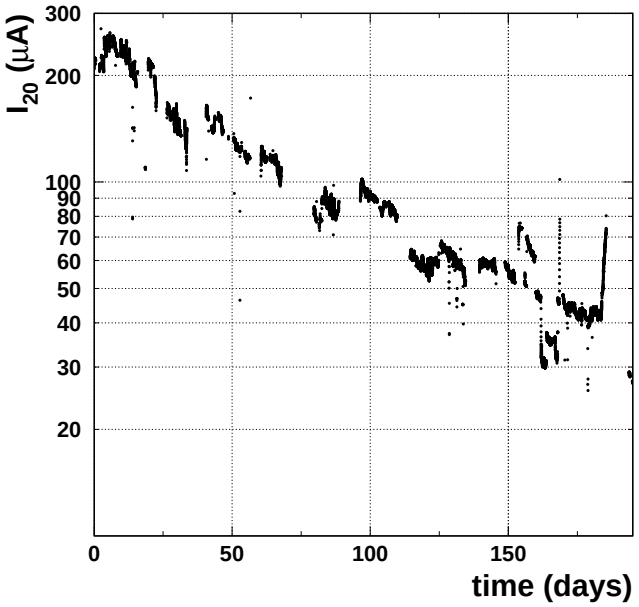

Figure 3.18: Current of RPC A corrected for temperature plotted versus time for the first year of aging test.

Figure 3.18 presents the corrected current (normalized at 20^{o}C) of RPC A as measured during the first year of irradiation test. Apart from some jumps, related to occasional changes in the high voltage, changes in the gas composition and to the insertion or removal of other detectors between the GIF and the RPC, a steady exponential decrease of the current is clearly observed, of almost one order of magnitude. These data have provoked a great astonishment, as a probable hint of an aging affect. The current decrease has been attributed to a corresponding increase of the detector resistivity, which seems to be the main effect of RPC aging.

3.10 Accumulated charge

In 2000 we irradiated in steady conditions three samples of bakelite with different resistivity by means of a very intense ^{6}0Co photon source [33]. The material demonstrated that its conductivity properties were not altered up to huge radiation doses, as high as 20 kGy, corresponding to few thousands years of LHCb.

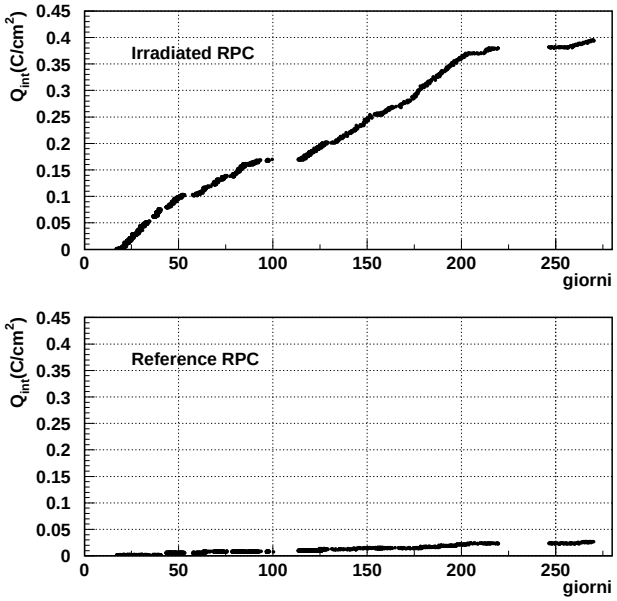

Figure 3.19: Accumulated charge density for RPC A (top) and RPC B (bottom) as a function of time.

Now we want to test the material when it is assembled inside a complete detector, and is traversed by a current flux. The parameter used to measure the amount of current flowing in a detector is the accumulated charge per surface unit, and it is commonly used to also measure the aging.

In wire chambers for example, the corresponding parameter the accumulated charge density per wire length. The LHCb MWPC are going to integrate up to

1 C/cm in ten of working. In a similar way we can evaluate the total charge density that will be accumulated in ten years of LHCb by the RPCs. The average expected flux in the Muon system is 375 Hz/cm^2 , corresponding to half the maximum flux expected in station 4 region 3 (see Table 2.1). The average avalanche charge produced by a low energy photon, supposed to be the main contribution to the background in LHCb, is 30 pC, twice the charge from a minimum ionizing particle. Then the current density flowing in the electrodes is 11.25 nA/cm^2 , corresponding in ten years (10^8 s) to 1.1 C/cm^2 . In order to accumulate such amount of charge in a reasonable time, the detectors were placed as close as possible to source, to increase the background rate, and were operated at a voltage of 10.8-11 kV, corresponding to the end of the efficiency plateau, to increase the current flow.

Figure 3.19 shows the accumulate charge density for the two detectors as function of time. Because of a not very steady GIF duty cycle, at the end of the first year the irradiated RPC could reach the value of 0.4 C/cm^2 , corresponding to 6 LHCb-years in the innermost region (M4-R3) and a little less than 2 LHCb-years in the outermost region (M5-R4).

After the reported period the chambers have not been able to accumulate much more charge, because their resistivity increased, even that of the reference RPC, so that the currents drawn were tiny, as viewed in the previous section.

3.11 Resistivity versus time

A systematic set of measurements of RPC electrode resistivity was regularly performed using the method described in section 3.7 starting from January 2001. In order to compare measurements taken at different temperatures, all the temperature-depending quantities have been rescaled to the reference temperature of 20 $^{\circ}$C .

The values of ρ_{20} for the first years are reported in Table 3.3 for RPC A, with the accumulated charge density.

Table 3.3: The time evolution of the accumulated charge density and the resistivity for RPC A and RPC B from 1999 to 2001.

	RPC A		RPC B	
Date	Q_{acc}(C/cm^2)	$\rho_{20}(10^{10}\ \Omega$cm)	Q_{acc}(C/cm^2)	$\rho_{20}(10^{10}\ \Omega$cm)
Oct 99	0	< 2	0	~ 4
Jan 01	0.076	6.6 ± 0.5	-	-
Mar 01	0.110	8.5 ± 0.7	-	-
Jul 01	0.361	26 ± 2.3	-	-
Aug 01	0.42	39 ± 4	0.05	13 ± 1.2
Dec 01	0.42	69 ± 6	-	-

Since the method used to measure the resistivity has been developed in 2001,

we have had to recover old data in order to estimate the RPC resistivity in 1999. The Figure 3.20 represents the measurement of the current as a function of the GIF flux intensity, the analogous of the Figure 3.12. It is clear that saturation was not at all reached in 1999, so that the resistivity could not be directly extracted by fitting the $I - V_0$ curve.

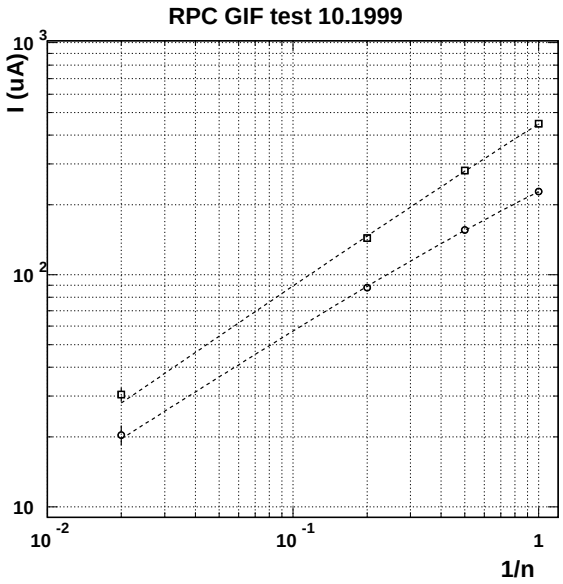

Figure 3.20: The current of RPC A (top) and RPC B (bottom) at fixed HV (10200 V) plotted against the inverse of the GIF absorption filter. The data were taken in October 1999. Comparing with Figure 3.12 the saturation effect is here very small, or absent, due to the small resistance of the RPCs.

The X term is in fact very small. By fitting the currents with Eq. (3.8) one has $X = 0.3 \pm 0.16$ for RPC B, and $X < 0.15$ at 95% CL for RPC A. This fact suggests that the initial resistivity of the RPCs was much lower than in 2001, at the beginning of the aging test. Although the value of R can not be extracted for such a low saturation value, an alternative indirect method is possible to evaluate the resistance of the detectors.

Recalling that $X = aR$, and knowing that a did not change from 1999 and 2001 (same distance from the source and roughly same activity) we can scale R according to X, and conclude that the RPC A resistivity in 1999 was less than 1.1×10^{10} Ωcm. The resistivity of RPC B was a factor 2 larger, namely 2.2×10^{10} Ωcm.

Since temperature was not monitored in 1999 an estimation have been done to obtain the reference values at 20 $^{\circ}$C . Basing on meteorological archives, the average temperature in the test area has been evaluated in 23 $^{\circ}$C , meaning a correction factor of 1.8. The corrected resistivities are then $\rho_{20} < 2 \times 10^{10}$ Ωcm for RPC A and $\rho_{20} = 4 \times 10^{10}$ Ωcm for RPC B, in fair agreement with the nominal building value.

After this period the detectors were stored for a year (2000). At the beginning

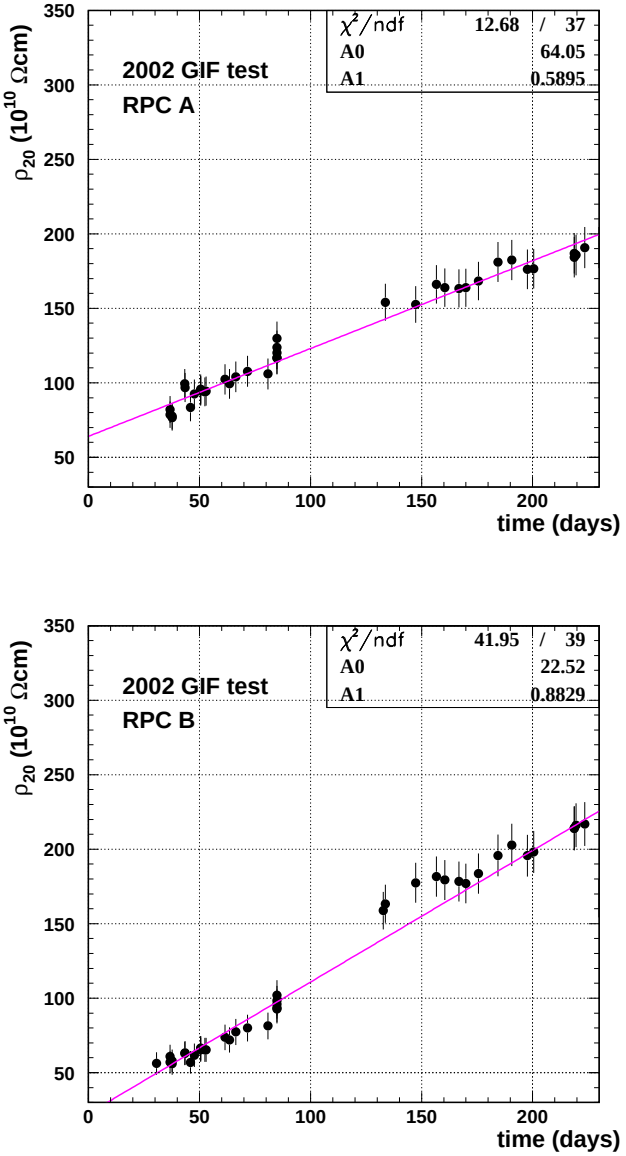

Figure 3.21: The resistivity for RPC A (top) and B (bottom) during 2002. The linear fit gives a slight steeper slope for RPC B.

of the aging test (January 2001) we found that the resistivity of RPC A had already increased by a factor 3. It increased another factor 6 during the irradiation period (January-August), when 0.42 C/cm^2 of charge density were accumulated. The increase continued even after August, when irradiation was stopped, confirming a clear contribution not related to irradiation. This is confirmed by the reference RPC, whose resistivity was measured again in August 2001, which increased from $\sim 3 \times 10^{10}$ Ωcm to $\sim 13 \times 10^{10}$ Ωcm, in spite of the low charge density accumulated (0.05 C/cm^2), mainly due to scattered photons or discharge currents.

From 2002 the detectors were both installed in front of the source and the resistivity was measured as frequently as possible. The results are plotted in Figure 3.21.

In the first 225 days the resistivity of both chambers continued increasing, even though, because of the high value reached, the currents drawn were tiny (about 5 nA/cm^2), so that negligible charge was accumulated during this period. The trend is rather linear, with RPC B showing a slightly steeper slope than RPC A. In fact this chamber, although never irradiated before, soon reaches resistivity values similar to the other, ending up the period with even a higher resistivity. These results suggest that a pure "temporal" effect also contributes to the RPC aging, and that this would be the main aging effect over 10 years of operation in LHCb.

3.11.1 Humid gas flow

The phenomenon of the increase in bakelite resistivity is thought to be related to a decrease of the water content in the bakelite plates. While water evaporation from the plates is always present, it is probably enhanced both by the current flowing in the electrodes and by the flux of dry gas in the chamber. It is already known, on the other hand, that humidity plays a crucial role in the conductivity process of the bakelite [42]. To verify this interpretation, and to check if the effect could be reversed, during 2003 we started a series of measurements flushing our RPCs with a humid gas mixture.

1.2% of vapor water was added to the usual gas mixture, by bubbling it through a tank containing water at 7 ^{o}C . The high voltage was turned on only for few minutes, during the measurements, in order to avoid the dangerous formation of fluoridric acid in the gap, consequently to a molecule breaking caused by the discharge. The results are shown in Figure 3.22.

In RPC A the effect was limited, while in RPC B the resistivity immediately is seen to decrease, and dropped a factor 2 in 20 days. When dry gas flow was restored the resistivity rapidly increased in both detectors, resuming the old values. Stopping the flow of dry gas also resulted in a less rapid decrease of the resistivity. The different behavior between the two detectors has to be probably ascribed to building differences.

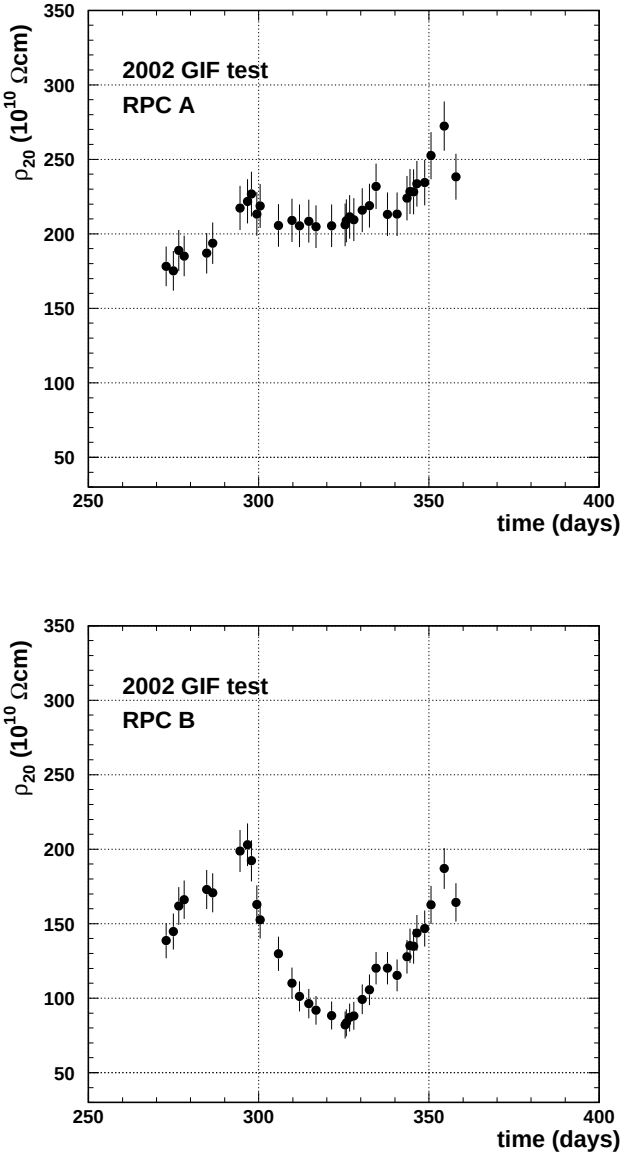

Figure 3.22: The resistivity for RPC A (top) and B (bottom) during 2003, when humid gas was flowed.

3.12 Rate capability measurements

Since the rate capability is inversely proportional to the electrode bulk resistivity, the study of the former is basically equivalent to the study of the latter. Furthermore is rather important to check how the increase of the resistivity observed affects the performances of the detectors under high rates. Whilst the resistivity of a material is a well defined physical quantity, this is not the case for the rate capability, that could depend on several variables, e.g. the readout electronics characteristics. Moreover it is defined by the specific requirements of the experiment.

Hence, in order to study quantitatively the effect, a rate capability definition suited for RPC detectors must be provided: *the rate capability Φ_{max} for a given RPC detector is the maximum rate the RPC can stand providing 95% efficiency, at the maximum voltage of 10.6 kV*.

This guarantees the 99% efficiency demanded by the trigger of LHCb for the AND of two chambers, and an operational plateau of about 400 V below 11 kV, considered the threshold of the streamer regime.

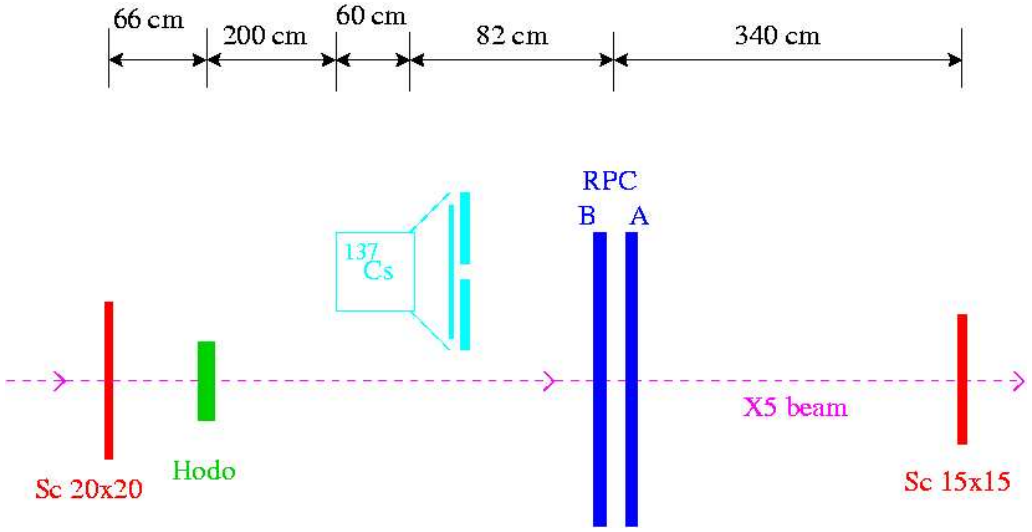

Figure 3.23: The experimental setup at GIF during test-beam with X5 muon beam.

To understand how the aging would affect the detector performances the RPC efficiency was measured in two test-beams. The tests have been performed in the same GIF area used for irradiation, by means of the X5 muon beam coming from the dump of a proton beam extracted from the CERN SPS. Muons comes to GIF in bunches every SPS cycle, during 14.4 s. A single bunch has a frontal section of about 10×10 cm^2 and contains 10^4 particles with an average momentum of 100 GeV/c.

Two scintillators at the very ends of the room provided the trigger, and a hodoscope measured the position of the particle with an accuracy of 1 cm. The detectors were placed centered with respect to the beam and aside with respect to

the source, though uniformly irradiated by it. The Figure 3.23 shows the setup.

3.12.1 2001 test

As previously seen after one year of aging test the irradiated RPC (A) showed a serious increase of the bakelite resistivity, which prevented the detector to accumulate a higher value of charge than 0.42 C/cm^2 . In the same period also the reference RPC (B) accumulated a little amount of charge, 0.05 C/cm^2 , mainly due to albedo particles. Thus in August 2001 another test-beam was performed to check the performances of the detectors.

In Figure 3.24 is plotted the efficiency of the RPC A as a function of the background rate for 5 different values of high voltage. The efficiency is normalized over the value at source off.

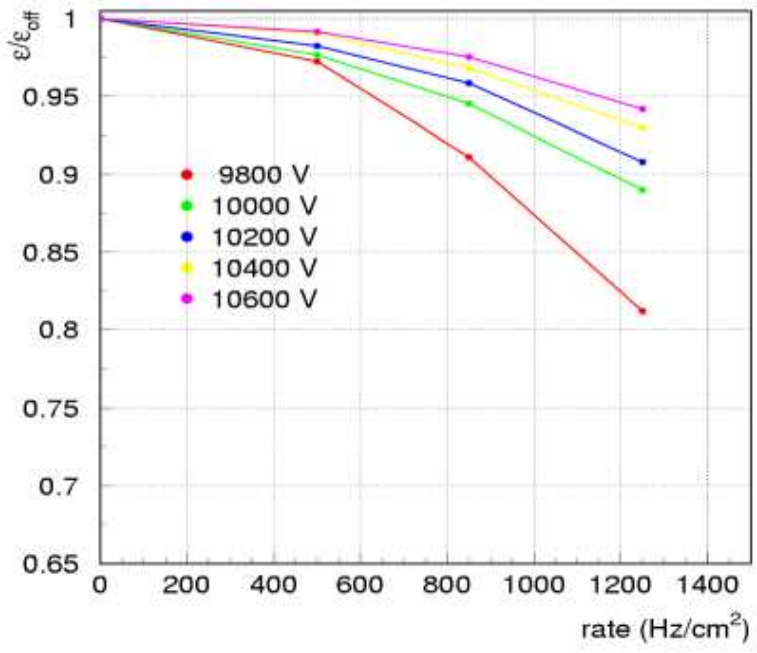

Figure 3.24: The relative efficiency of RPC A as a function of the background rate for various HV values measured in August 2001 at the GIF. The measurements have been taken with a temperature of 25.1°C .

It is seen that the rate capability for this detector, as it has been defined in Section 3.3, is about 1.15 kHz/cm^2 . Since the rate capability is inversely proportional to the resistivity of the electrodes, this value must be rescaled to the reference temperature of 20°C by means of the Equation 3.9, in order to be compared with similar measurements. Considering that the average temperature of the test was 25.1°C it is straightforward to find that the rate capability of RPC A at the reference temperature was 640 Hz/cm^2 .

Also the resistivity of the RPC A was measured during this test, finding the value of 20×10^{10} Ωcm, which reported to the reference temperature becomes 39×10^{10} Ωcm (see Table 3.3).

Hence, after one year of test and 0.42 C/cm^2 accumulated charge the resistivity of the RPC increased and subsequently a degradation of the rate capability performance is found.

3.12.2 2002 test

In the summer of 2002 another comprehensive test was performed, in order to better quantitatively characterize the effects of aging in RPCs. Figure 3.25 shows the various efficiency curves for different source absorption factors as a function of applied voltage for the two RPCs under test. The detectors exhibit very similar performances, as one could have argued from the fact that the resistivity were measured to be comparable, even if there is a factor of 8 in the accumulated charges.

The normalized efficiency as a function of the particle rate (Figure 3.26) shows that the rate capability of the detectors has decreased down to about 350 Hz/cm^2 for both RPCs. This means about 200 Hz/cm^2 at the reference temperature of 20^{o}C .

3.13 Conclusions

We have been extensively studying aging effects on bakelite RPCs for three years, applying a properly developed method which allows to measure the electrode resistivity during the chamber operation. The results of the three different beam tests performed over a period of three years are summarized in Table 3.4.

Table 3.4: Resistivity ρ and rate capability Φ_{max} for RPC A in three different beam tests at GIF. (* RPC B).

Test	ρ (10^{10} Ωcm)	Φ_{max} (Hz/cm^2)	T (^{o}C)	ρ @ 20 ^{o}C (10^{10} Ωcm)	Φ_{max} @ 20 ^{o}C (Hz/cm^2)
Oct 99	< 1	~ 5000	23	< 2	~ 3500
Aug 01	20	1150	25.1	35	650
Jul 02	65	350	24.5	110	200
Jul 02*	45	380	24.5	75	220

The value of the resistivity of the first test is affected by large uncertainties, being evaluated indirectly by "historical" values, properly rescaled according to the model. The rate capability too has to be considered not so accurate, because a comprehensive study of the efficiency dependence from rate was not done. Taking into account this, all the values of Φ_{max} result in good agreement with the $1/\rho$

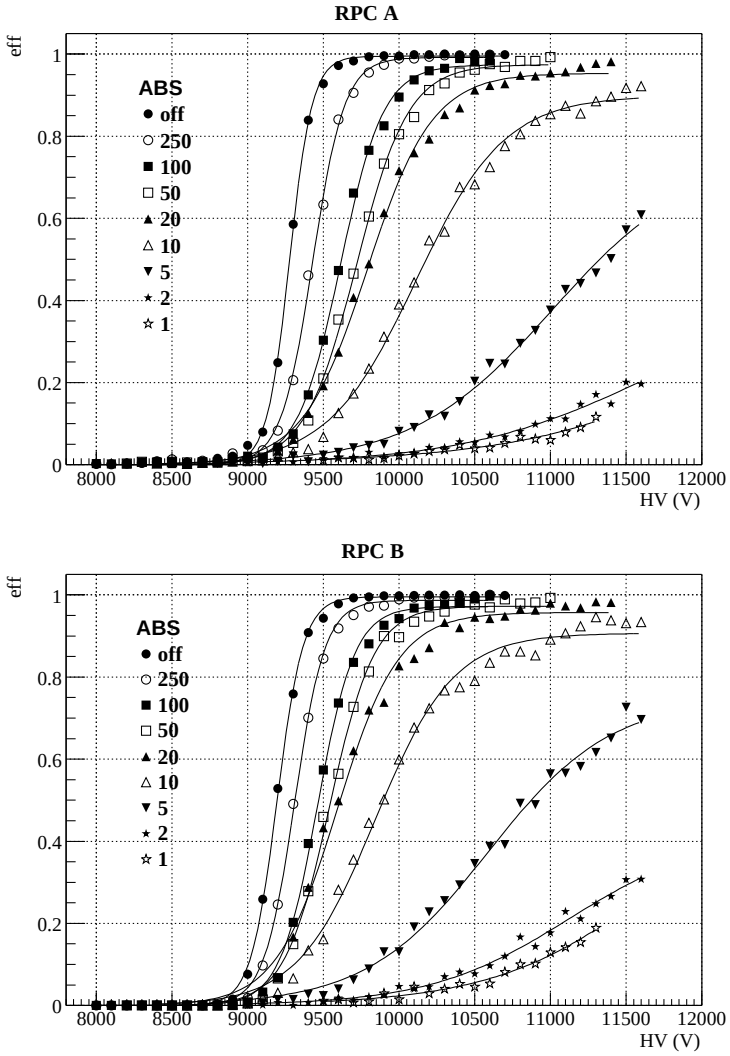

Figure 3.25: Efficiency of RPC A (top) and RPC B (bottom) plotted against the chamber HV, for different source absorption factors.

dependence, in particular the 2001 and 2002 data, presenting a constant product of $\rho\,\Phi_{max}$.

At the end of the test the resistivity of the RPC plates shows an increase of two orders of magnitude, from 10^{10} Ωcm to 10^{12} Ωcm. Although irradiation may contribute, the effect seems mainly to be spontaneous, induced by the drying up of the bakelite. Humid gas has been flowed with different response: one detector rapidly decreased its resistivity while the other was much less affected. Restoring dry gas flow has resulted again in fast resistivity increase for both, making the method not very useful to recover the detector performances.

As expected the resistivity rise caused a drop in the rate capability, from few kHz/cm^2 to about 200 Hz/cm^2 . We can estimate how much the Muon system performances would have been deteriorated by such a decrease of the rate capability.

The combined efficiency of the two stations, each one is covered by a double layer of RPC detectors is

$$\epsilon_{M4\&M5} = (1 - (1 - \epsilon_{RPC})^2)^2$$

In Region 3 the average rate is 700 Hz/cm^2 . From Figure 3.26 is seen that the single RPC efficiency, corresponding to such a rate, for a reasonable value of HV, is about 65%. The consequent M4&M5 efficiency would be 77%, reducing to 75% when the whole Muon detector is considered. This would result in an unaffordable degradation of the trigger performances.

After the results of this comprehensive aging test the LHCb collaboration has decided to switch to the safer MWPC technology to cover also the outermost regions of the muon detector.

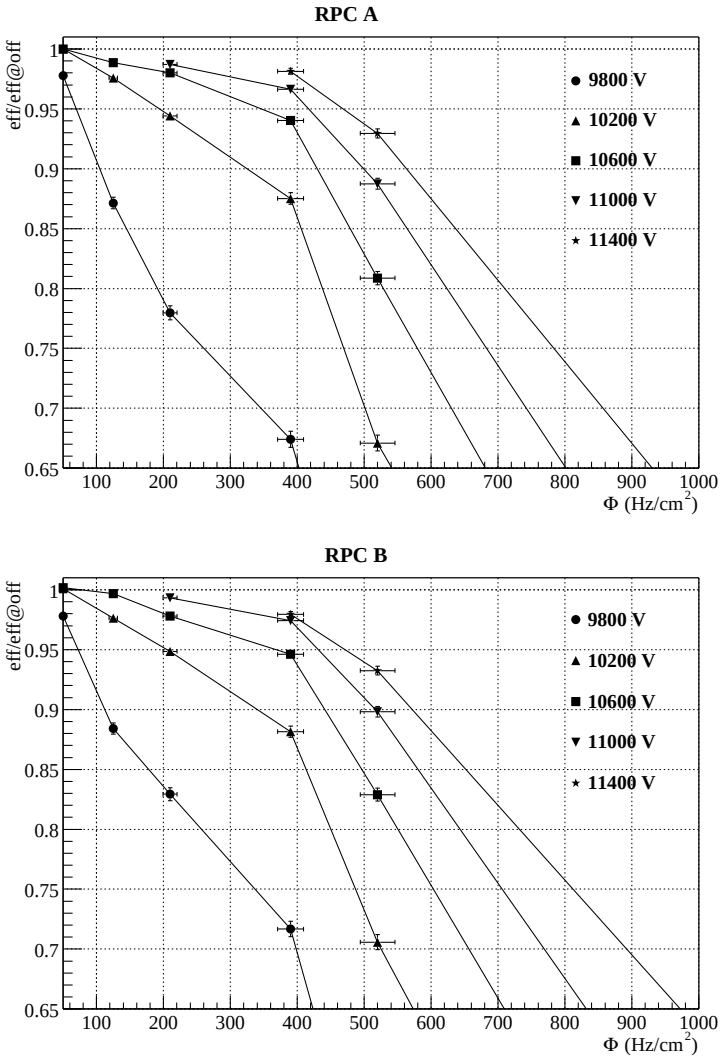

Figure 3.26: Efficiency of RPC A (top) and RPC B (bottom) plotted against the particle flux, for different value of high voltage. The measured has been taken in August 2002 at a temperature of 24.5°C .

Part II

Physics studies

Chapter 4

Study of $pp \to \mathrm{Z}^0 \to \mu^+\mu^-$ process at LHCb

4.1 Introduction

The Z^0 boson is the "massive photon" responsible for the weak neutral current interactions. It was predicted within the electroweak theory and was firstly produced in a proton-antiproton collision at 540 GeV center-of-mass energy, with its charged companions W^+ and W^-, at the CERN $\mathrm{Sp\bar{p}S}$. Then its characteristics were precisely measured at LEP, where e^+ and e^- beams were tuned just at the Z^0 resonance energy, to get the highest production cross-section.

The heavy mass ($\sim$ 91 GeV/c^2) makes the detection of this particle rather easy. An interesting signature is represented by a couple of leptons with opposite charges and high transverse momenta. This and the large invariant mass of the particles provide a clear selection strategy and ensures a good efficiency in the rejection of the combinatorial background, practically negligible at such high values of p_{T} .

Although the Z^0 detection does not enter the main LHCb B-physics program, its features make this channel very useful for calibration and alignment purposes, and for absolute luminosity measurement. Moreover the particular shape of LHCb, designed to cover low polar angles, turns out to be decisively in the study of peculiar proton structure functions, selecting quasi-free partons.

In this chapter the process $pp \to \mathrm{Z}^0 \to \mu^+\mu^-$will be studied, exploiting the characteristics of the LHCb detector, in particular the precise muon identification and the good momentum resolution. The aim of the study is to demonstrate that in spite of the limited angular acceptance and the optimization for a different kind of physics, the number of Z^0 detected at LHCb is sufficient to make profitable physics. Three possible applications have been individuated and discussed: the calibration of the spectrometer, the absolute luminosity measurement and the calculation of the proton structure functions.

4.2 Hadronic production of Z^0 boson

In the framework of the parton model the hadronic production of a Z^0 boson $pp \to Z^0 \to \mu^+\mu^-$ is described as a particular case of the general Drell-Yan process $pp \to \mu^+\mu^- X$, schematized in Figure 4.1. If p_A and p_B are the two incoming beam

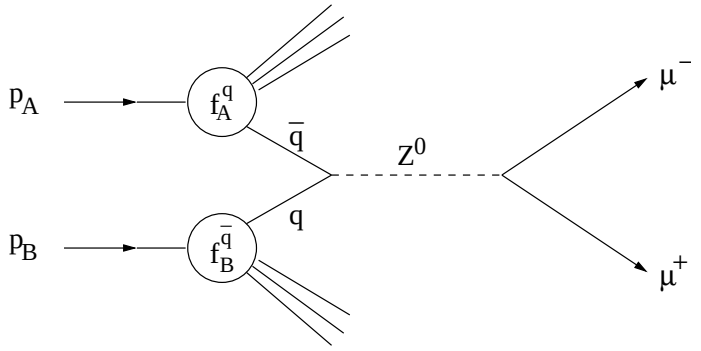

Figure 4.1: The basic $q\bar{q} \to Z^0 \to \mu^+\mu^-$ parton model interaction.

protons in their center-of-mass frame, each with energy E_{beam}, the total squared center-of-mass energy is then $s = 4E_{beam}^2$. The two partons $q\bar{q}$ (as well as qg) that enter the hard interaction carry fractions x_1 and x_2 of the total beam momentum, i.e. they have four-momenta

$$p_1 = E_{beam}(x_1; 0, 0, x_1)$$
$$p_2 = E_{beam}(x_2; 0, 0, -x_2)$$

The squared invariant mass of the two partons is defined as

$$\hat{s} = (p_1 + p_2)^2 = x_1\, x_2\, s$$

The QCD tree level diagrams for the point-like parton process are drawn in Figure 4.2. The most probable process is the quark-antiquark annihilation ($q\bar{q} \to Z^0$), which may be combined with a gluon ($q\bar{q} \to Z^0 g$) or a photon ($q\bar{q} \to Z^0\gamma$) radiation. Note that differently from the proton-antiproton machines, at LHC the antiquarks must come from the sea, because only protons are colliding. The other possible process is the Compton scattering between a quark and a gluon ($qg \to qZ^0$). An example of a possible one loop correction diagram for such a process is also sketched in Figure 4.3.

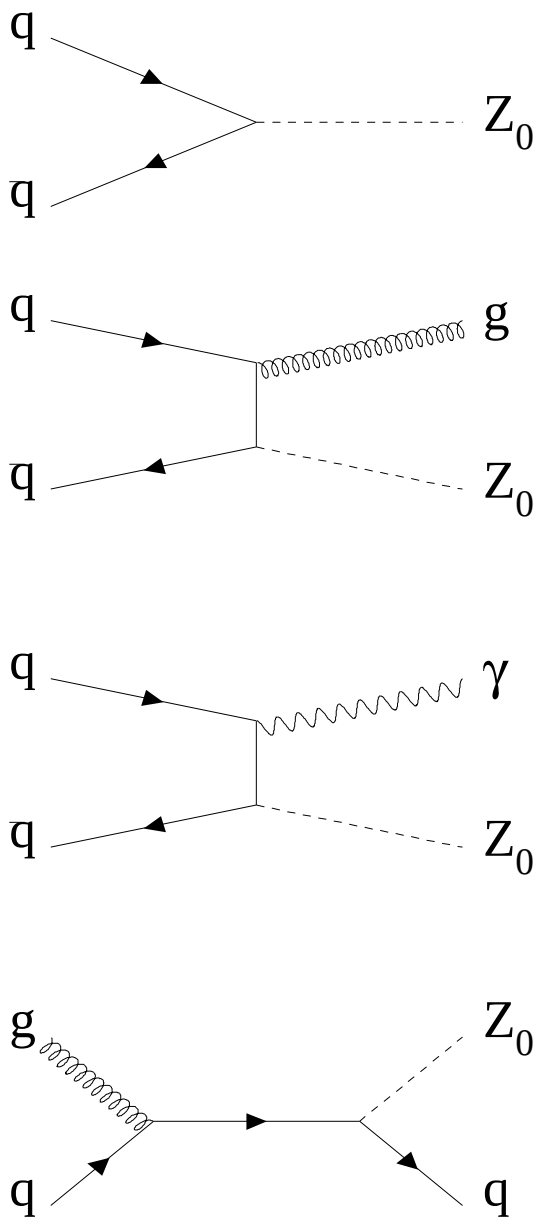

Figure 4.2: Tree level diagrams for Z^0 production in a proton-proton collision. From top to bottom there are the quark-antiquark annihilation, the same process with a gluon or photon radiation, and the quark-gluon Compton scattering.

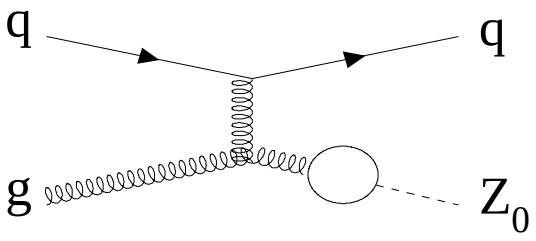

Figure 4.3: One loop correction to the quark-gluon scattering diagram.

Instead of x_1 and x_2 it is often customary to use the related variables τ and y

$$\tau = x_1\, x_2 = \frac{\hat{s}}{s}$$
$$y = \frac{1}{2}\ln\frac{x_1}{x_2}$$

the first relation thus fixes the product of $x_1\, x_2$ at LHC ($\sqrt{s}$ = 14 TeV) to $\tau \approx 4 \times 10^{-5}$. It is effortless to demonstrate that the variable y is the rapidity of the Z^0 boson, so that the single fractional momenta of the quarks and antiquarks are directly related to the rapidity distribution of the weak boson

$$x_1 = \sqrt{\frac{M_Z^2}{s}}\, e^{y} \qquad x_2 = \sqrt{\frac{M_Z^2}{s}}\, e^{-y}$$

For momenta much larger than the Z^0 mass ($p \gg M_Z$), y can be safely approximated by the pseudorapidity

$$y \approx \eta = -\ln\, \tan(\theta/2)$$

As a consequence the x distributions of the partons can be argued from the observable pseudorapidity distributions of the muons from the Z^0 decay. In Figures 4.4 and 4.5 are shown the x distributions for the selected $Z^0 \to \mu^+\mu^-$ events in LHCb.

4.2.1 Cross-section

The cross-section for the Drell-Yan process in the parton model at first order of approximation for $q\bar{q}$ fusion is [54]

$$\frac{d\sigma}{dm^2}(p_A p_B \to \mu^+\mu^- X) = \left(\frac{4\pi\alpha^2}{3m^2}\right)\frac{1}{3}\sum_q e_q^2 \int_0^1 dx_1 \int_0^1 dx_2 \left[f_A^q(x_1) f_B^{\bar{q}}(x_2) + f_A^{\bar{q}}(x_1) f_B^q(x_2)\right] \delta(m^2 - \hat{s}) \quad (4.1)$$

with $\hat{s} = M_Z^2$ in the case of the Z^0 production The first factor in brackets is the high energy QED cross-section for $e^+e^- \to \mu^+\mu^-$, since $q\bar{q} \to \mu^+\mu^-$ is the same

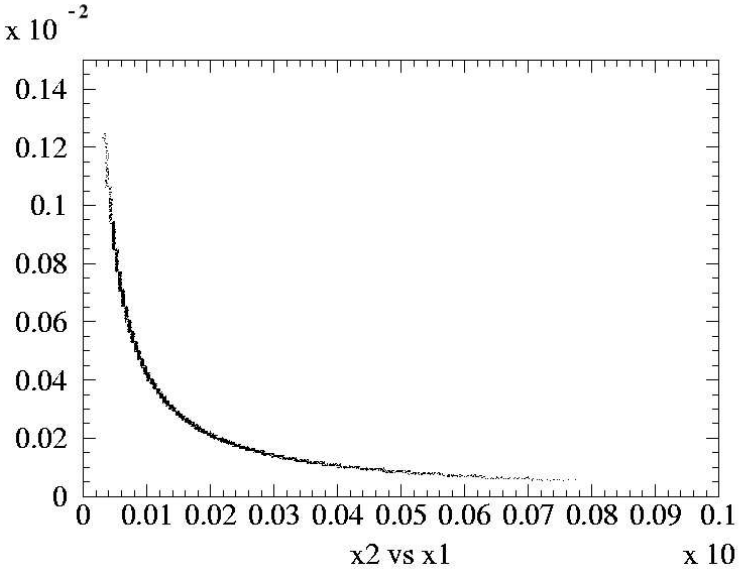

Figure 4.4: Fractional momentum of the upstream parton plotted against the fractional momentum of the downstream parton. Their product is a constant.

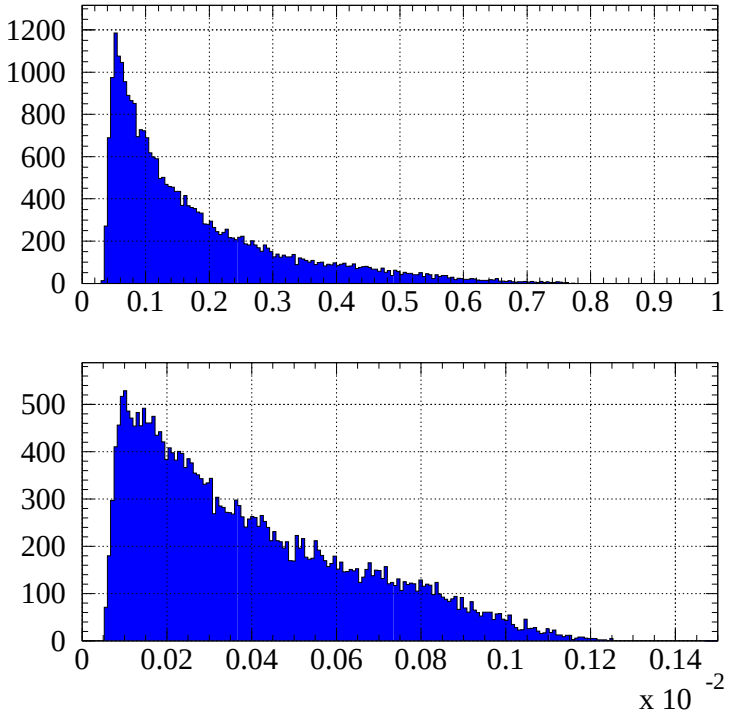

Figure 4.5: Fractional momentum distributions of the downstream parton (top) and upstream parton (bottom).

apart from the quark charge. The extra factor 1/3 accounts for the fact that all three colors of q and $\bar{q}$ occur with equal probability, but only a q and $\bar{q}$ of the same color can annihilate to form a colorless boson. The $f^q(x)$ are the quark structure functions, which must be known at different values of fractional momenta x, in order to evaluate the integral.

The production cross-section of Z^0 boson has been recently measured at the Tevatron collider, the proton-antiproton machine with $\sqrt{s}$ = 1.96 TeV (see Figure 4.6). The last updated results for the $Z^0 \to \mu^+\mu^-$ cross-sections are $\sigma_Z B(Z \to \mu\mu)$ = 246 ± 6(stat.) ± 12(syst.) ± 15(lum.) pb and $\sigma_Z B(Z \to \mu\mu)$ = 263.8 ± 6.6(stat.) ± 17.3(syst.) ± 26.4(lum.) pb, for CDF and DØ experiments respectively [55]. Both measurements are consistent with the Next-to-Next-to-Leading-Order (NNLO) theoretical calculation of 250.5 ± 3.8 pb [56]. All the values already include the branching ratio for the $\mu\mu$ decay mode, which is (3.367 ± 0.008)%.

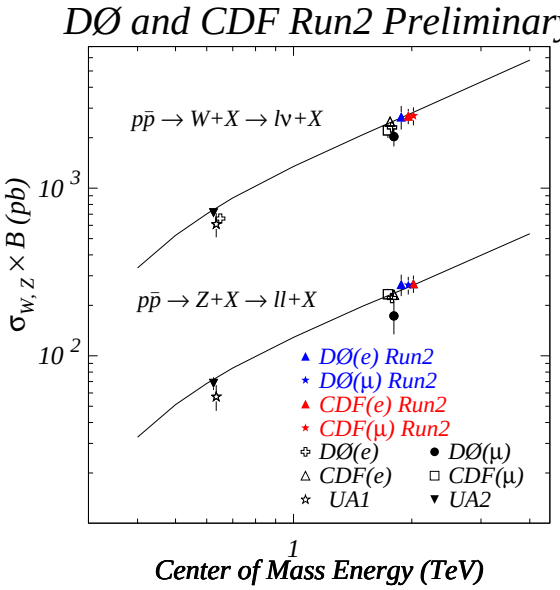

Figure 4.6: $W \to l\nu$ and $Z^0 \to ll$ cross-section measured by CDF and DØ at $\sqrt{s}$ = 1.96 TeV. The data match with the theoretical NNLO calculation represented by the solid lines.

Recently a NNLO estimation of the Z^0 production cross-section has been done for the LHC energy of 14 TeV as well [57]. At such a higher energy the cross-section is foreseen to be almost an order of magnitude larger, as high as $\sigma_Z B(Z \to \mu\mu)$ = 1.86 ± 0.07 nb (see Figure 4.7).

4.3 Luminosity monitor

LHCb will have a great potential to make various precision measurements in the B physics sector and to discover New Physics. It is designed to provide high statistics

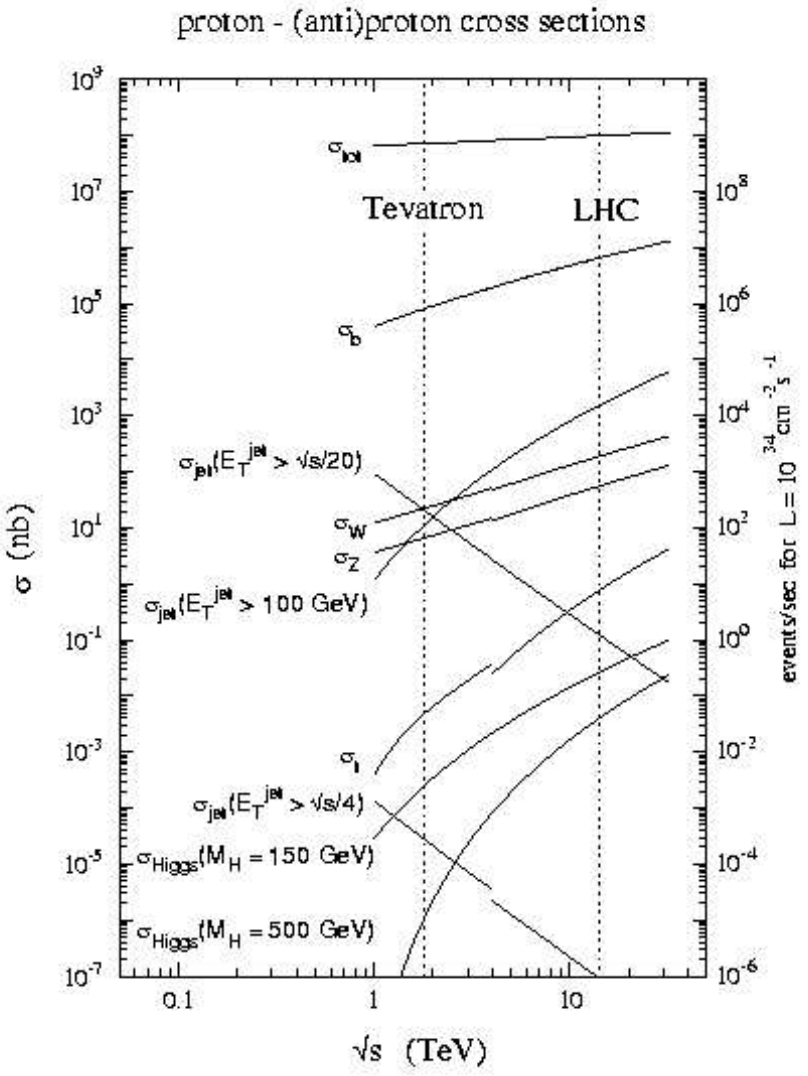

Figure 4.7: Total proton-(anti)proton cross-sections as a function of $\sqrt{s}$. The relative values for Tevatron and LHC are marked. The figure is taken from [58].

B related data samples, and the accuracy of the precision measurements will be limited by systematics effects and, in some case, by the uncertainty in the measurement of the luminosity $\mathcal{L}$. Although a mere relative luminosity knowledge, simply achievable by counting the total event multiplicity, is sufficient to determine given quantities (e.g. branching ratios), the absolute luminosity value is needed to compute the cross-sections.

In general there are two possibilities to determine the luminosity. Either to measure a pair of cross-sections which are connected quadratically with each other, or to measure a cross-section whose value is well known or which may be calculated with good accuracy. The well-known example of the first possibility is the measurement of the total and differential forward elastic cross-sections which are related by the optical theorem. This method requires dedicated detectors placed as close as possible to the beam, and is used at LHC by the TOTEM experiment [59].

Several types of processes stand out as examples of the second possibility to measure the luminosity. One is the exclusive lepton-pair production via photon-photon fusion

$$pp \to pp\, l^+ l^-$$

Luminometers for LHC based on such a process, measuring either $\mu^+\mu^-$ pairs [60] or e^+e^- pairs [61] have been proposed.

Recently attention has also focused on W and Z^0 production as a possible luminosity monitor. The reason is that the signal is clean, and the production cross-sections are large and can now be calculated with considerable theoretical accuracy [57].

A Next-to-Next-to-Leading-Order (NNLO) calculation at the LHC center-of-mass energy is reported in Figure 4.8, for both the weak bosons. The figure shows the

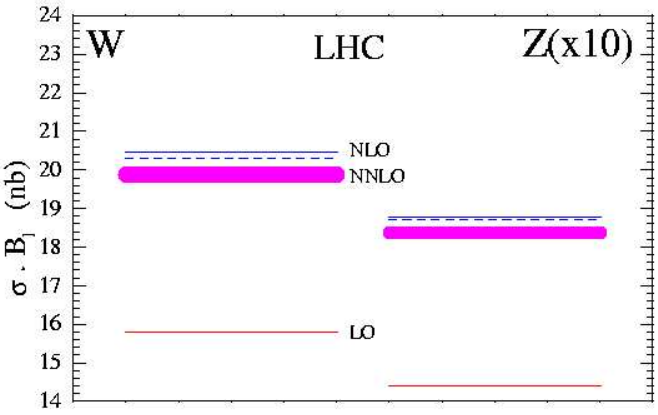

Figure 4.8: The prediction of the cross-sections for W and Z^0 production and leptonic decay at LHC obtained from global analysis of the same data set MRST00 [62].The band of the NNLO predictions takes into account the ambiguity in the corresponding splitting functions [63].

successive approximations starting to Leading-Order (LO). The final result has an error band, accounting for uncertainties in some deep inelastic coefficient function and in $\alpha_S(M_Z^2)$, of about 1%. However the uncertainties in the input of the quark density functions mean that the error could, conservatively, be as large as $\pm$ 4% (see Figure 4.9).

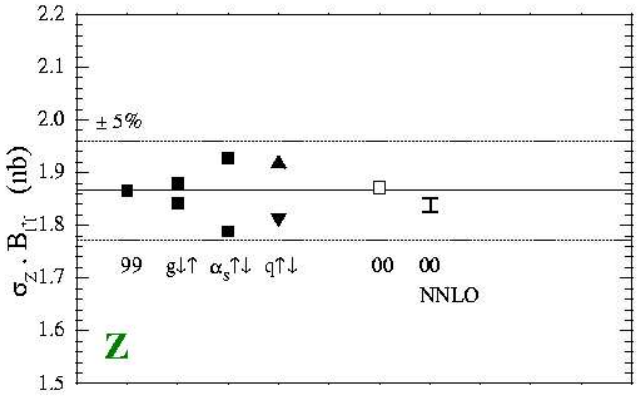

Figure 4.9: The predictions of the cross-section for Z^0 production and leptonic decay at LHC obtained using various NLO and NNLO sets from MRST99 [64] and MRST00 [62].

As seen from Figure 4.8, the cross-section for the charged W bosons is more than an order of magnitude larger respect to the neutral Z^0 . This would suggest the use of W$\rightarrow \mu\nu$ events, to measure the luminosity. Although this channel keeps all the characteristics of $Z^0 \rightarrow \mu^+\mu^-$concerning the very low background, the presence of the undetected neutrino causes a more complicated reconstruction, especially in a non hermetic detector like LHCb. Hence for the purpose of this thesis only the $Z^0 \rightarrow \mu^+\mu^-$process has been considered, with the proposal of studying W$\rightarrow \mu\nu$ in the future.

Once the cross-section is known the luminosity can be calculated by the relation:

$$\mathcal{L} = \frac{N_{Z\rightarrow\mu\mu}}{\sigma_{Z^0} \times B_{\mu\mu} \times \epsilon_{tot}}$$

where $N_{Z\rightarrow\mu\mu}$ is the event yield observed, σ_{Z^0} is the cross-section, $B_{\mu\mu}$ is the branching ratio for the relevant channel, and ϵ_{tot} is the total efficiency of the detector.

Note that in order to limit the statistical uncertainty below the 4% of the theoretical error, about 10^3 events must be collected.

4.4 Spectrometer calibration

One of the hardest difficulties encountered in a very complicated experiment like LHCb is to study and to control the systematics. An exact alignment of the sub-

detectors and a precise calibration of the spectrometer are needed to perform an accurate physics analysis.

A by-product of selecting the channel $Z^0 \to \mu^+\mu^-$ is to store tracks with huge momentum value. The decaying muons momentum range can be evaluated by the relation

$$\frac{M_Z}{\Delta\theta_{max}} < p_\mu < \frac{M_Z}{\Delta\theta_{min}}$$

where $\Delta\theta$ is the opening angle between the two muons. Considering 40 mrad and 700 mrad respectively as the minimum and maximum possible angle one gets that the muon momentum is comprised between 130 GeV/c and 2275 GeV/c.

These tracks are very little affected by the multiple scattering in the material, and can be used off-line to precisely align the various detectors downstream to the magnet.

Another possible applications of the collected data sample of $Z^0 \to \mu^+\mu^-$ is the calibration of the LHCb spectrometer. The Z^0 boson mass is known with an accuracy $\Delta M/M \sim 10^{-5}$. This can be used to correct any systematic effect in the measurement of the particle momentum. Furthermore the very high momenta of the decaying muons allow to calibrate the resolution of the spectrometer up to few TeV/c region.

4.5 Study of quark distribution functions

We have seen in Section 4.3 how decisively the quark density affects the cross-section. They enter the theoretical calculation through the parton distribution functions (or structure functions) $f_i(x, Q^2)$, which parameterize the probability to find a parton i with a fraction x of the beam energy ($x = p_{parton}/E_{beam}$) when the beam particle is probed by a hard scattering at the scale Q^2.

If $\hat{\sigma}$ is the parton cross-section for a given process, then the hadron cross-section may be written as

$$\sigma = \int dx_1 dx_2 f_1(x_1, Q^2) f_2(x_2, Q^2)\ \hat{\sigma} \tag{4.2}$$

The relevant types of partons in the case of the proton are the valence and sea quarks (or antiquarks) and the gluons. Many different sets of parton distributions exists in literature for the proton [65]. These are usually determined from experimental observables in lepton-hadron deep inelastic scattering (from fixed target and HERA experiments) and Drell-Yan lepton pair production processes at hadron colliders [66]. The experimental data are fitted with the constrain that the Q^2 dependence is in accordance with the standard QCD evolution equations. An example of proton structure functions taken by the CTEQ 4L data set [67] is shown in Figure 4.10. The momentum-weighted combination $xf_i(x, Q^2)$, for which the normalization condition $\sum_i \int dx x f_i(x, Q^2) = 1$ normally applies, is drawn for up and $down$ valence quarks and for sea quarks, as a function of x at $Q^2 = M_Z^2$.

Whilst the x distributions of the valence quarks are now well constrained, uncertainties for the x distributions of sea quarks and antiquarks and gluons remain

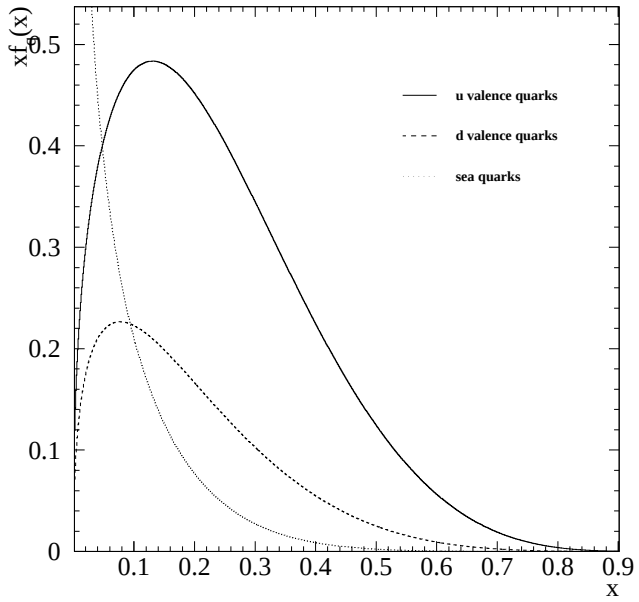

Figure 4.10: Momentum-weighted proton structure functions for up and $down$ valence quarks and for sea quarks-antiquarks, plotted against the fractional momentum x for a fixed $Q^2 = M_Z^2$. The data set is CTEQ 4L, the standard PYTHIA generator input.

important. As a result the total cross-section prediction of Z^0 boson production is much more inaccurate than the point-like QCD calculation would allow.

Thus precisely measuring the Z^0 production cross-section, and assuming that the parton cross-section $\hat{\sigma}$ is known with good accuracy, from Eq. (4.2) the parton distribution functions $f(x, Q^2)$ can be determined at $Q^2 = M_Z^2$ for different x. Note that at LHC, in contrast to proton-antiproton colliders like Tevatron, the antiquarks entering the process have to come from the sea. Hence the possibility to highly improve the accuracy of the poorest known distribution functions is realized.

4.6 $pp \to Z^0 \to \mu^+\mu^-$simulation

In order to study the $pp \to Z^0 \to \mu^+\mu^-$process, 50000 events have been generated and the complete response of the LHCb detector has been simulated. The whole analysis work was centrally realized at CERN, on the Linux cluster LXPLUS/LXBATCH [68], a farm of about 1000 machines providing computing power to CERN users.

4.6.1 Event generation

The generation of the data sample is performed using the FORTRAN program SICBMC, which embeds different packages to implement different tasks.

The proton-proton interactions are generated using PYTHIA 6.2, the standard event generator in high-energy physics, continuously tuned to reproduce the latest experimental results. All the tree level processes described in the previous section are included in the simulation of the Z^0 production. Elastic proton-proton scattering ($pp \to pp$), single diffraction ($pp \to pX$), and double diffraction ($pp \to XY$) processes are considered as well, in order to simulate the underlying event. Being interested only in real Z^0 bosons, the Z^0 /γ^* interference structure has been not considered, just including the Z^0 matrix elements, so that only "on mass-shell" Z^0 are generated.

The decay of unstable particles is performed by the QQ program. In order to save CPU time and increase the event generation efficiency, the Z^0 is forced to decay to $\mu^+\mu^-$, which are required both to have a polar angle less than 400 mrad, representing the limit angle a track may have to leave hits in at least three VELO stations. To save further generation time the Monte Carlo always try to change the sign of the z component of the momentum before rejecting a track as outside the acceptance.

The tracking of the decay products through LHCb is performed by the GEANT package. The detector geometry and material are described in detail, including the active detector components and their front-end electronics, passive materials, such as the beam-pipe, infrastructural supports, and so on. Low-energy particles, mainly produced in secondary interactions inside the detector, are also traced applying a cut-off of 10 MeV for hadrons and 1 MeV for electrons and photons.

The whole SICBMC program is to be replaced by its C++ counterpart, called GAUSS, which makes use of GEANT4.

4.6.2 Detector response

The digitization and the reconstruction of the event is performed by the C++ program BRUNEL. The response of various sub-detectors is simulated, introducing the detection efficiency, the spacial resolution and the electronic noise.

Then the reconstruction algorithms elaborate the different hits producing tracks, vertices and particles with determined properties, prompt for the analysis.

Recently the digitization phase has been split from BRUNEL and performed by a dedicated package called BOOLE. BRUNEL is now ready to receive as its input either simulated hits or real detector response.

4.6.3 Physics analysis

Finally the events are analysed with the C++ program DAVINCI, in order to select the interesting physics and reduce background. All the Monte Carlo information

is available in the analysis ("MC Truth"), though it is absolutely hidden in the reconstruction phase.

Unlike what is going to happen during real data taking, the trigger filter is also applied in DAVINCI. The L0 and L1 algorithms however, just flag the triggered events, providing the complete on-line and off-line selection for any kind of study.

4.7 Event selection

In Figure 4.11 is schematized a generic $\mu\mu$ event, with some of the properties of the reconstructed tracks used in the event selection. Every track has its own impact parameter (IP) respect to the primary vertex, i.e. to the primary interaction point. In the case of a Z^0 production this should be the only vertex present in the event, as it coincides with the secondary vertex, i.e. the common muons decay vertex. To identify muons originating from the interaction point from those arising from

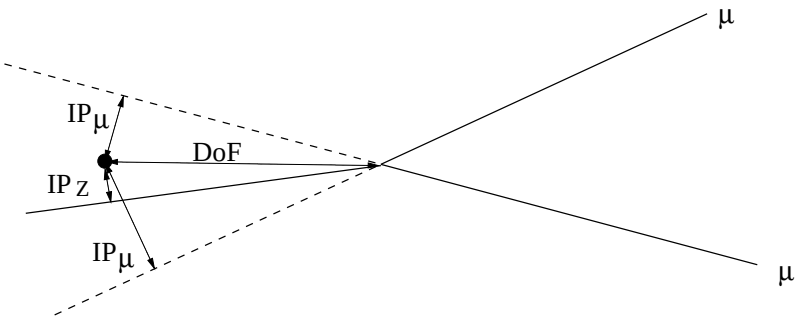

Figure 4.11: Schematic representation of a reconstructed $Z^0 \to \mu^+\mu^-$event. Some of the track parameters used for the selection are indicated. IP is the impact parameter respect to the primary vertex and Dof is the distance of flight.

long-lived particles (e.g. from semileptonic decay of B mesons) a small impact parameter is requested.

In the figure are also drawn the impact parameter of the Z^0 and its distance of flight (DoF). Having the Z^0 a $c\tau = 0.08$ fm, it does not fly at all, so that both these quantities must be compatible with zero, within the reconstruction error.

Hence the topology of the channel is very simple, with two muons with opposite charge coming directly from the interaction point whose invariant mass is near the Z^0 boson mass. The event reconstruction thus requires to look for muons with very low impact parameter and Z^0 with small impact parameter and distance of flight.

The selection algorithm starts with the reconstruction of the primary vertex, i.e. the determination of the z coordinate of the primary collision. The interaction region has a Gaussian distribution with $\sigma = 5$ cm around the nominal interaction point. All the tracks reconstructed in the VELO are used to identify the primary vertex, in order to get the best resolution. The analysis is performed only for single

interaction events, and in case more than one primary vertex is found, the event is skipped.

Then the reconstructed tracks identified as muons are selected. The particle identification algorithm combines the informations from different sub-detectors: the RICH system, the ECAL and HCAL calorimeters, and the Muon system, of course, which provides discrimination between hadrons, electrons and muons. For the $Z^0 \to \mu^+\mu^-$channel the most relevant source of misidentification is represented by the pions that succeed in traversing the muon filter (*punch-through*). The Table 4.1 reports the muon identification efficiency and the misidentification probabilities for b$\to \mu$X events. Although the momentum range for the muons de-

Table 4.1: Muon identification efficiency (%) and particle misidentification probabilities (%) for b$\to \mu$X.

	Nominal background	Maximal background
ϵ^{μ}	94.0 $\pm$ 0.3	94.3 $\pm$ 0.3
$\mathcal{M}^{e}$	0.78 $\pm$ 0.09	3.5 $\pm$ 0.2
$\mathcal{M}^{\pi}$	1.50 $\pm$ 0.03	4.00 $\pm$ 0.05
$\mathcal{M}^{\mathrm{K}}$	1.65 $\pm$ 0.09	3.8 $\pm$ 0.1
$\mathcal{M}^{\mathrm{p}}$	0.36 $\pm$ 0.05	2.3 $\pm$ 0.1

caying from b quarks is rather lower respect to the Z^0 muons, the reported values may give an idea of the performances of the LHCb detector.

The next step is to make all the possible $\mu^+\mu^-$combinations. For each of them an unconstrained vertex fit is performed and the single impact parameters respect to the primary vertex are calculated. If a di-muon is likely to come from a same decaying particle, the invariant mass is calculated and a Z^0 boson candidate is created. The impact parameter and the distance of flight of the Z^0 are then evaluated. Very rarely ($< 0.1\%$) the algorithm finds more than one Z^0 candidate, in which case the whole event is skipped.

4.7.1 Definition of selection cuts

Ten different selections parameters are used to isolate the signal decays of interest. They are described in the following (see also Figure 4.11). In order to optimize the selection, every couple of muons is divided accordingly to the largest and the smallest of each parameter, and separate cuts are applied. Pairs of tracks identified as muons with opposite charge are formed requiring:

- the track with the smallest momentum p to have $p > 60$ GeV/c;
- the track with the largest momentum p to have $p > 100$ GeV/c;

- the track with the smallest transverse momentum p_{T} to have $p_{\mathrm{T}} > 10$ GeV/c;
- the track with the largest transverse momentum p_{T} to have $p_{\mathrm{T}} > 20$ GeV/c;
- the track with the smallest impact parameter significance respect to the primary vertex $\mathrm{IP}/\sigma_{\mathrm{IP}}$ to have $\mathrm{IP}/\sigma_{\mathrm{IP}} < 3$
- the track with the largest impact parameter significance respect to the primary vertex $\mathrm{IP}/\sigma_{\mathrm{IP}}$ to have $\mathrm{IP}/\sigma_{\mathrm{IP}} < 5$

Each pair surviving these conditions is fitted to a common vertex and used to form a Z^0 candidate. The Z^0 candidates are created requiring:

- the di-muon vertex fit to have a chi-square $\chi^2 < 5$;
- the di-muon invariant mass to lie within a $\pm$ 25 GeV/c^2 window centered on the nominal Z^0 boson mass;
- the Z^0 candidate to have an impact parameter significance respect to the primary vertex $\mathrm{IP}/\sigma_{\mathrm{IP}} < 5$;
- the Z^0 candidate to have a distance of flight significance $\mathrm{DoF}/\sigma_{\mathrm{DoF}} < 5$;

For a Gaussian error the significance indicates the displacement of a certain quantity from zero in units of standard deviations, and is therefore the most meaningful statistical variable. Requiring an impact parameter significance $\mathrm{IP}/\sigma_{\mathrm{IP}} < 5$ means that the impact parameter must be compatible with zero within 5 standard deviations. This is no more true if the error is not Gaussian, which could happen in case of a bad reconstruction.

4.7.2 Trigger selection

Events surviving the off-line selection are then passed through the L0 and L1 trigger simulation algorithms. The complete off-line and on-line performance of the detector can then be studied.

As seen in Section 1.3 the LHCb trigger project includes a third level, commonly referred to as High Level Trigger (HLT), still under development. Anyway preliminary considerations suggest that because of the high signal to background ratio of the $\mathrm{Z}^0 \to \mu^+\mu^-$channel, a minimal bandwidth can be achievable in the HLT without a further reduction of the event rate, that is maintaining an efficiency of the order of 100%.

4.8 Selection efficiencies

The total signal efficiency is calculated as the fraction of signal events that are triggered (by L0 and L1), reconstructed and selected with off-line selection cuts. It can be factorized as

$$\epsilon_{tot} = \epsilon_{gen} \times \epsilon_{rec'ble} \times \epsilon_{rec'ted} \times \epsilon_{sel} \times \epsilon_{trig}$$

The different efficiencies for $Z^0 \to \mu^+\mu^-$ are summarized in Table 4.2 and are discussed below.

Table 4.2: Summary of signal efficiencies for $Z^0 \to \mu^+\mu^-$. The error is statistical. The number of processed events are reported as well.

	Event number	Efficiency (in %)
Generated in 4π	110766	
Generated in 400 mrad	49734	$\epsilon_{gen} = 44.9 \pm 0.2$
Reconstructible	16205	$\epsilon_{rec'ble} = 32.6 \pm 0.2$
Reconstructed	15460	$\epsilon_{rec'ted} = 95.4 \pm 0.2$
Selected	14359	$\epsilon_{sel} = 92.9 \pm 0.2$
L0 passed	13955	$\epsilon_{L0} = 97.2 \pm 0.1$
L1 passed	8711	$\epsilon_{L1} = 62.4 \pm 0.4$
Total efficiency		$\epsilon_{tot} = 7.9 \pm 0.1$

- *generation efficiency* (ϵ_{gen}). This is the efficiency to generate events with the required cut at 400 mrad. This ratio is much greater than the corresponding solid angles ratio $0.4/\pi = 13\%$ because at the LHC energy the muons decaying from Z^0 are considerably forward boosted at low polar angles, in spite of their large transverse momentum, as can be seen from Figure 4.12, showing the theta distributions of the two decaying muons. It is also evident how the polar angles of the two opposite charge muons are highly correlated.

- *reconstructible efficiency* ($\epsilon_{rec'ble}$). It is not an easy task to precisely determine the geometrical acceptance of a such complicated detector as LHCb is. The reconstructibility notion helps in the determination of whether a certain track is likely to be effectively reconstructed by the apparatus, including the geometrical acceptance and any possible material effects in the detector. A Monte Carlo event to be reconstructible implies that all the final state particles are reconstructible. A stable charged MC particle can be reconstructible in one of the following categories:

  Long track: the particle has $3r+3\phi$ VELO clusters and $1x+1stereo$ clusters in each of the 3 Tracking stations.
  Upstream track: the particle has $1x+1stereo$ clusters in each of the 3 Tracking stations and 3 Trigger Tracker clusters.
  VeloTT track: the particle has $3r+3\phi$ VELO clusters and 3 Trigger Tracker clusters.

  The most of the muons decaying from Z^0 are reconstructible as Long tracks.

- *reconstructed efficiency* ($\epsilon_{rec'ted}$). A decay to be effectively reconstructed implies that all the final state particles are reconstructed, meaning that an as-

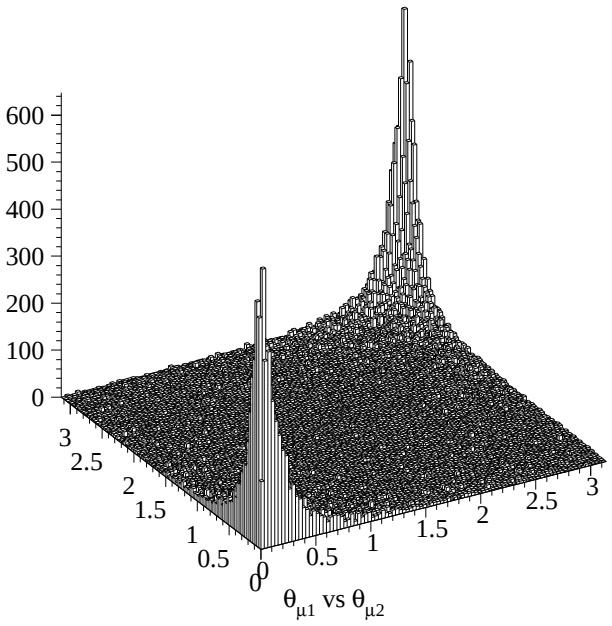

Figure 4.12: Polar angles of the two muons decaying from Z^0 boson in 4π.

sociation has been found between the real reconstructed track and a corresponding reconstructible MC track. This association is done if:

Long tracks share at least 70% of the clusters in the VELO and 70% in the Tracking stations.
Upstream tracks share at least 70% of the clusters in the Tracking stations and have no more than 1 different cluster in Trigger Tracker out of those used.
VeloTT tracks share at least 70% of the clusters in the VELO and have no more than 1 different cluster in Trigger Tracker out of those used.

The reconstruction efficiency is well above 90%, as expected for muons with such a high momentum. The value in is fair agreement with the muon identification efficiency for b events (see Table 4.1), which result to be practically independent from the momentum above 10 GeV/c.

- *selection efficiency* (ϵ_{sel}). Basically no background process exists for the channel $Z^0 \to \mu^+\mu^-$with similar production rates. The selection cuts can then be smooth, and consequently the selection efficiency is high, above 90%.

- *L0 trigger efficiency* (ϵ_{L0}). The L0 algorithm select the 8 highest p_{T} muons, 2 for each Muon station quadrant. It is hence straightforward for a $Z^0 \to \mu^+\mu^-$event to pass the L0 trigger filter, as denoted by the very high efficiency.

- *L1 trigger efficiency* (ϵ_{L1}). The matter is well different for the L1 trigger, which in fact has a much lower efficiency. Its algorithm looks for a detached

secondary vertex, being optimized for B-physics, and tends to refuse the $Z^0 \to \mu^+\mu^-$ event. Moreover both muons very often saturates the dynamic p_T range of the L0, fixed at 5.15 GeV/c. At L1 the two muons arrive with the same p_T value and are rejected as clones. This unexpected feature of the clone-checking algorithm of the L1 had never been exploited before, and the study of $Z^0 \to \mu^+\mu^-$ process has been decisively to discover it. It has now been fixed by checking the hit tiles in M1, as well. What actually helps in increasing the L1 efficiency is that a bonus is foreseen for muon pairs with large invariant mass, which can override the algorithm decision. At the end the result is comparable for instance with that of $J/\psi \to \mu^+\mu^-$.

4.9 Annual yield

Once the total efficiency is known, the annual signal yield is computed as

$$S = \mathcal{L}_{int} \times \sigma_{Z^0} \times B_{\mu\mu} \times \epsilon_{tot} \tag{4.3}$$

where $\mathcal{L}_{int} = 2$ fb^{-1} is the annual integrated luminosity, assuming 10^7 s as one year of data taking and $\mathcal{L} = 2 \times 10^{32}$ cm^{-2} s^{-1} as nominal average luminosity; $\sigma_{Z^0} \approx 55$ nb is the Z^0 production cross-section expected at 14 TeV; $B_{\mu\mu} \approx 3.4\%$ is the branching ratio of the Z^0 decay in $\mu^+\mu^-$.

The number of events produced in the solid angle, filtered by the off-line selection and by the trigger are reported in Table 4.3. The final annual yield

Table 4.3: Annual yield for $Z^0 \to \mu^+\mu^-$.

Produced in 4π	Off-line selected	L0+L1
(3.6 $\pm$ 0.1) M	(483 $\pm$ 4) k	(293 $\pm$ 3) k

of 293 hundreds events per year means a bandwidth of 29 mHz, or 1 $Z^0 \to \mu^+\mu^-$ event every 34 s. As a comparison, the total number of $Z^0 \to \mu^+\mu^-$ collected by the Aleph experiment was about 200k in 5 years of data taking (1990–1995) at $\sqrt{s} \simeq 91$ GeV [69].

4.10 Single muon distributions

Single muons distributions are reported in the following figures, both for reconstructed and selected tracks.

The momentum distributions are shown in Figure 4.13. The high peak at very small momenta is due to the combinatorial background and is efficiently cut out with minor loosing of events in the high momenta region. It is interesting to note how the tail of the distribution reaches very high values, up to 2 TeV/c. This will result rather useful for calibration purposes.

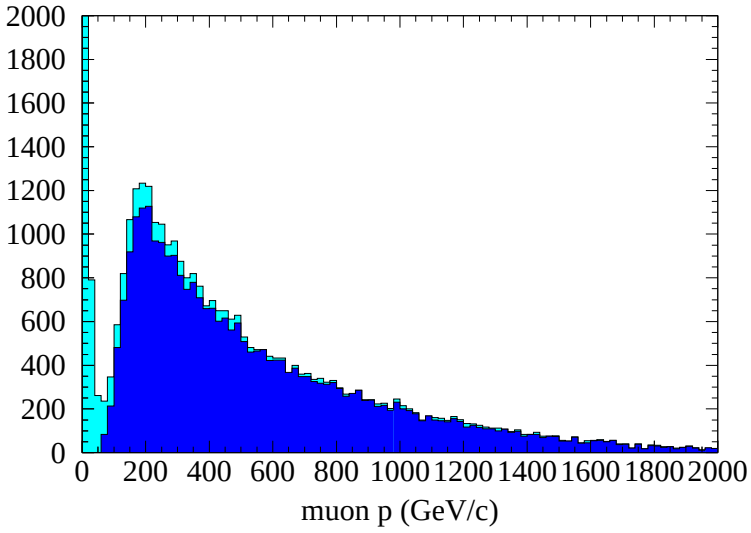

Figure 4.13: Momentum spectra of the reconstructed (light) and selected (dark) muons tracks.

The single muons transverse momentum spectra (Figure 4.14) shows a peak value at half the Z^0 boson mass, as expected. Again the reconstructed tracks with very low p_T are due to the combinatorial background. Note how the clear separation between the Z^0 decaying muons population and the low-p_T tracks population provides an easy and well optimized selection cut. This is peculiar of the low-angle tracks and represents a major difference respect to the 4π experiments, which predominantly collect particles at high angles.

Also the polar angle θ distribution (Figure 4.15), and consequently the pseudorapidity $\eta = -\ln \tan(\theta/2)$ distribution (Figure 4.16), are mostly affected by the p_T cut, which rather depopulates the zone with $\theta < 0.1$ rad and $\eta > 3$, where the low-p_T background is present. In Figure 4.16 the 4π expected distribution has been superimposed as well, in order to appreciate the pseudorapidity acceptance of the LHCb detector. Note the cuts at very low polar angle ($\theta < 20$ mrad) and very high pseudorapidity ($\eta > 5$), indicating that muons escape from the detector acceptance as they enter the hole left for the beam-pipe, which has a coverage of about 20 mrad in x plane and 15 mrad in y plane.

The impact parameter significance respect to the primary vertex is shown in Figure 4.17. As foreseen most of the tracks have an impact parameter within 2 standard deviations from zero. For a comparison, a typical corresponding cut for $B^0 \to \pi^+\pi^-$ is between 5 and 10. Of course in that case the cut is on the lower values.

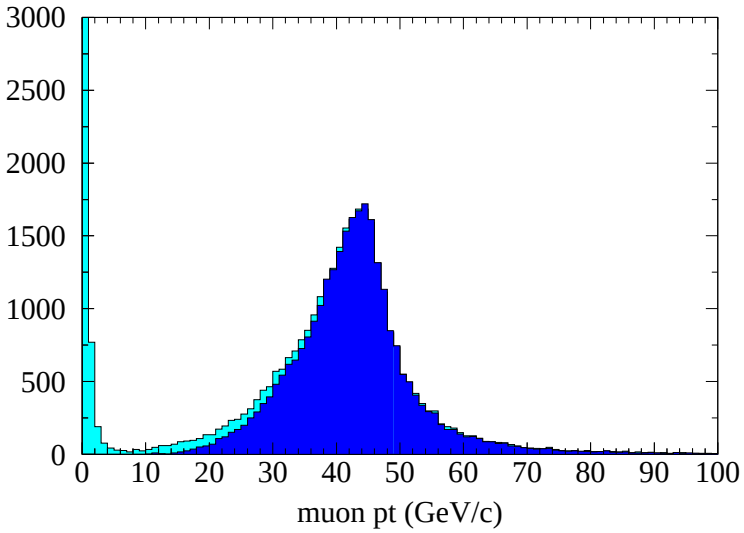

Figure 4.14: Transverse momentum spectra of the reconstructed (light) and selected (dark) muons tracks.

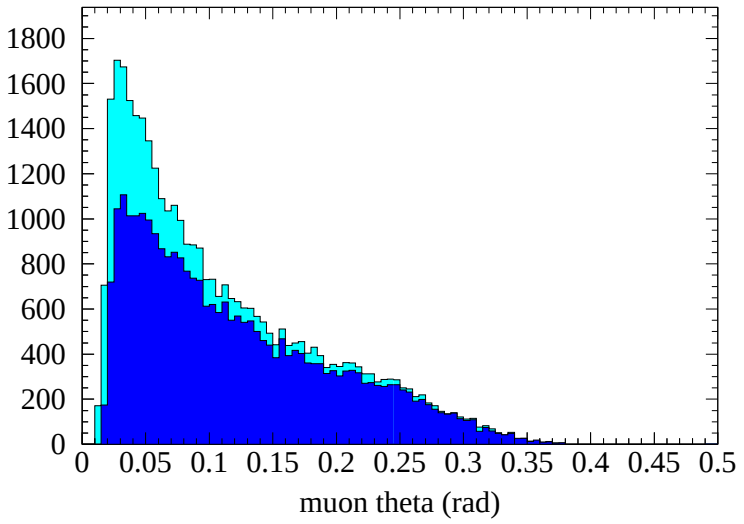

Figure 4.15: Polar angle distributions of the reconstructed (light) and selected (dark) muons tracks.

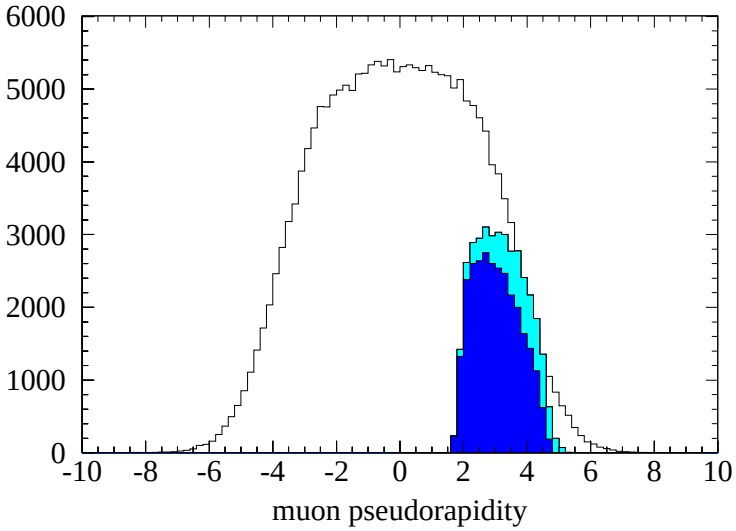

Figure 4.16: Pseudorapidity distributions of the reconstructed (light) and selected (dark) muons tracks. In white the predicted pseudorapidity distribution of muon in 4π.

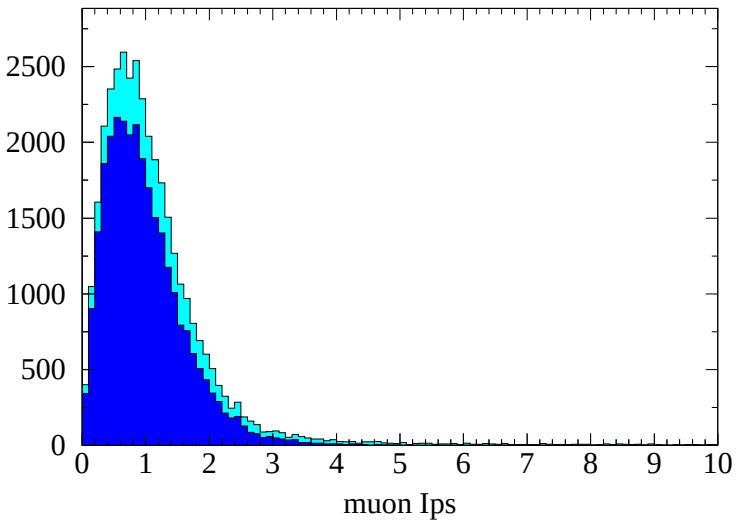

Figure 4.17: Impact parameter significance distributions of the reconstructed (light) and selected (dark) muons tracks.

4.11 Invariant mass and Z^0 distributions

The di-muons invariant mass is plotted in Figure 4.18. The spectrum has been

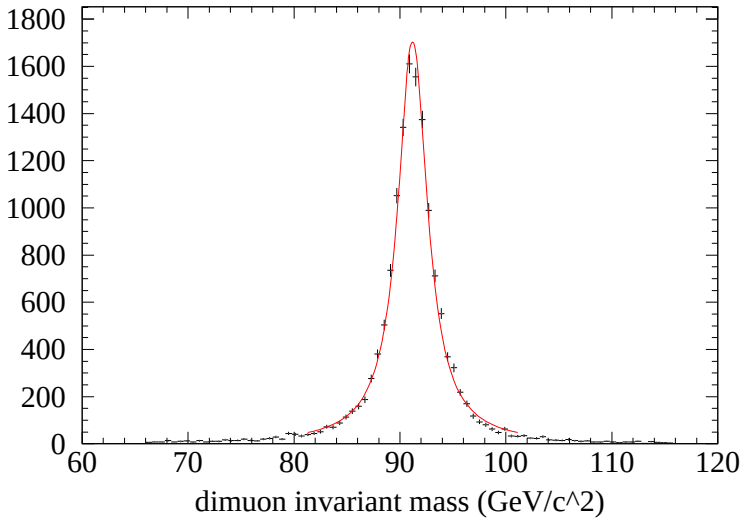

Figure 4.18: Invariant mass spectrum of the di-muons fitted with a Breit-Wigner function.

fitted with the usual Breit-Wigner function

$$\sigma_{BW}(M) = N\frac{\Gamma_{tot}^2}{(M - M_R)^2 + \Gamma_{tot}^2/4}$$

and the fit results for Z^0 mass and width are reported in Table 4.4 with the analogous PDG [56] published values. The mass of the Z^0 is determined with a relative

Table 4.4: Z^0 boson properties as fitted from di-muon invariant mass and as published on PDG 2000.

	Z^0 Mass M_R (GeV/c^2)	Z^0 Full width Γ_{tot}
Fit	91.19 ± 0.02	3.35 ± 0.04
PDG	91.882 ± 0.0022	2.4952 ± 0.0026

error of $\Delta M/M \approx 2 \times 10^{-4}$ and it is perfectly compatible with the PDG value. The full width of the resonance results a $\sim$ 30% wider respect to the PDG value. This broadening is the effect of the momentum resolution of LHCb spectrometer, not optimized to measure such high values. Moreover the relative error on the momentum measurement increases with the momentum itself, because higher

momentum tracks are less bent by the magnet, and have smaller sagitta. For LHCb the relation is

$$\frac{\Delta p}{p} = 3.6 \times 10^{-5}\,\mathrm{GeV/c}^{-1}\; p$$

which means for instance that a momentum of 750 GeV/c, corresponding to the mean value of Z^0 decaying muons distribution, is determined with a 3% error, and a momentum of 2 TeV/c with a 7% error.

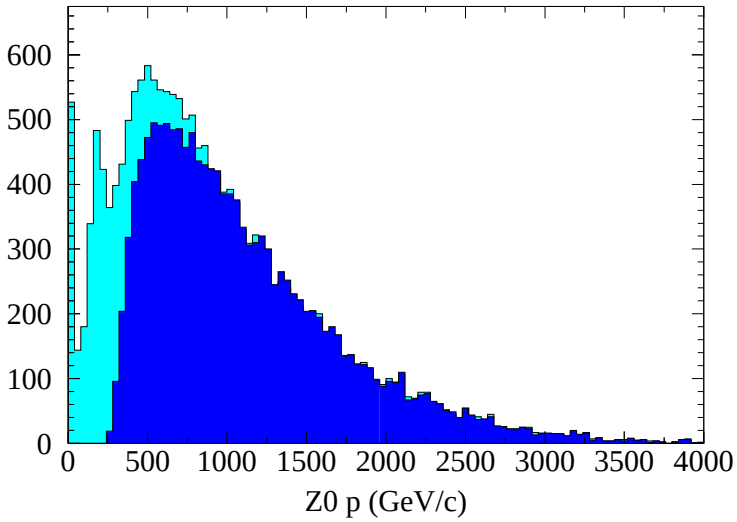

Figure 4.19: Momentum spectrum of the reconstructed (light) and selected (dark) Z^0 boson.

Figure 4.19 represents the Z^0 candidates momentum spectrum. Note how although none direct cut is applied on this quantity, only particles with more than 250 GeV/c momenta are selected.

The transverse momentum distribution is plotted in Figure 4.20. The bump at $\sim$ 40 GeV/c, cut out by the selection, is due to fake Z^0 candidates formed by a true Z^0 decaying muon, with a most probable p_{T} near to half the Z^0 mass, and a low-p_{T} background muon arising from the interaction point.

Figure 4.21 shows the pseudorapidity distribution of the Z^0 candidates. It is clear how the selection criteria cut the bosons with low pseudorapidity, as they have a great probability to have a decaying muon out of the detector acceptance.

The impact parameter significance distribution of the Z^0 candidates (see Figure 4.22) looks very similar to the single muon distribution (Figure 4.17), confirming that both particles are likely to be produced in the primary interaction vertex.

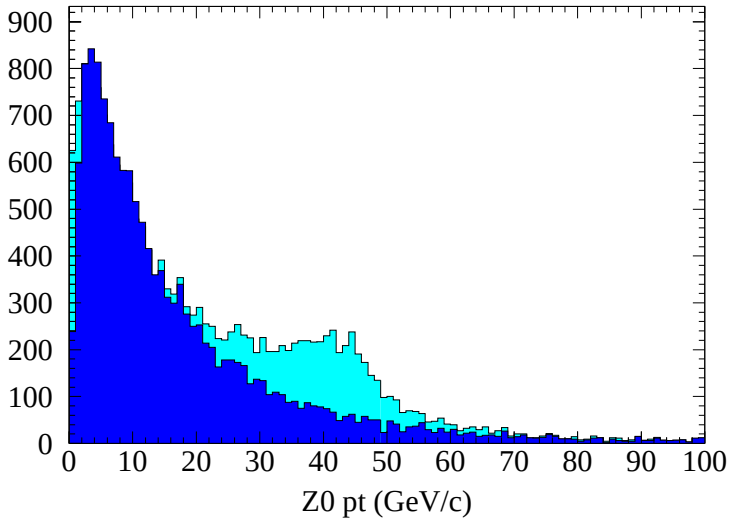

Figure 4.20: Transverse momentum spectrum of the reconstructed (light) and selected (dark) Z^0 boson.

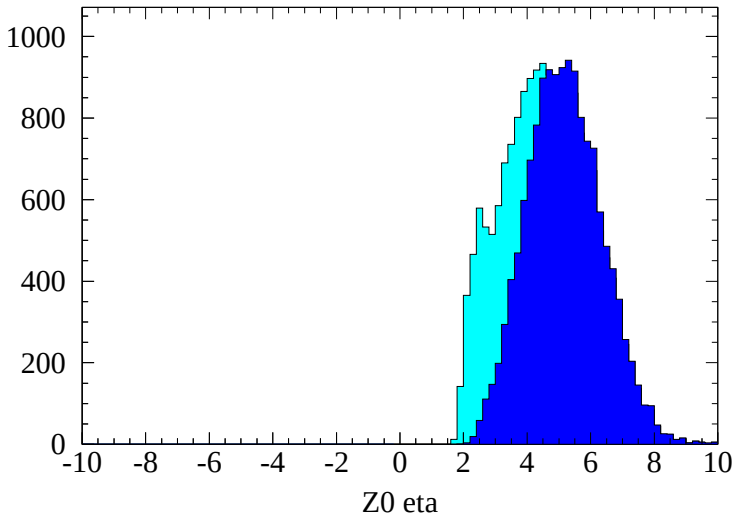

Figure 4.21: Pseudorapidity distribution of the reconstructed (light) and selected (dark) Z^0 boson.

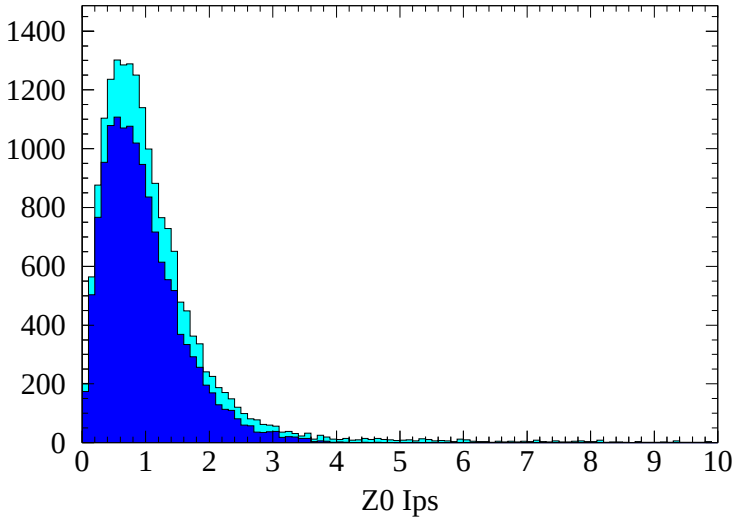

Figure 4.22: Impact parameter significance distribution of the reconstructed (light) and selected (dark) Z^0 boson.

4.12 Analysis results

The analysis has demonstrated that a useful number of $Z^0 \to \mu^+\mu^-$events will be detected at LHCb. Assuming an event rate of $\sim$ 30 mHz (from Table 4.3) the necessary statistics to perform an absolute luminosity measurement with an error below the theoretical limit of 4%, is collected in about 9 hours of data taking. However one is not obliged to collect 10^3 events every time an absolute luminosity measurement is needed. It is in fact straightforward to use this process to calibrate some relative luminosity monitor in order to achieve precise and instantaneous absolute luminosity informations.

As a result of the forwardness of LHCb, low polar angle and high pseudorapidity particles are selected. This means that the parton coming downstream the detector carries almost the whole amount of momentum, while the parton coming upstream the detector is essentially at the rest. Thus LHCb will have a great potential to study the parton structure function at high $Q^2 = M_Z^2 \sim 10^4$ and very low $x \sim 10^{-4}$, in a kinematic region not probed by the present experiments, as results from Figure 4.23.

Figure 4.24 shows the explored regions of the $Q^2 - x$ plane. LHCb will be able to confirm the Tevatron data at high Q^2 reducing the statistical error, and to extend the measurements to a very low x region.

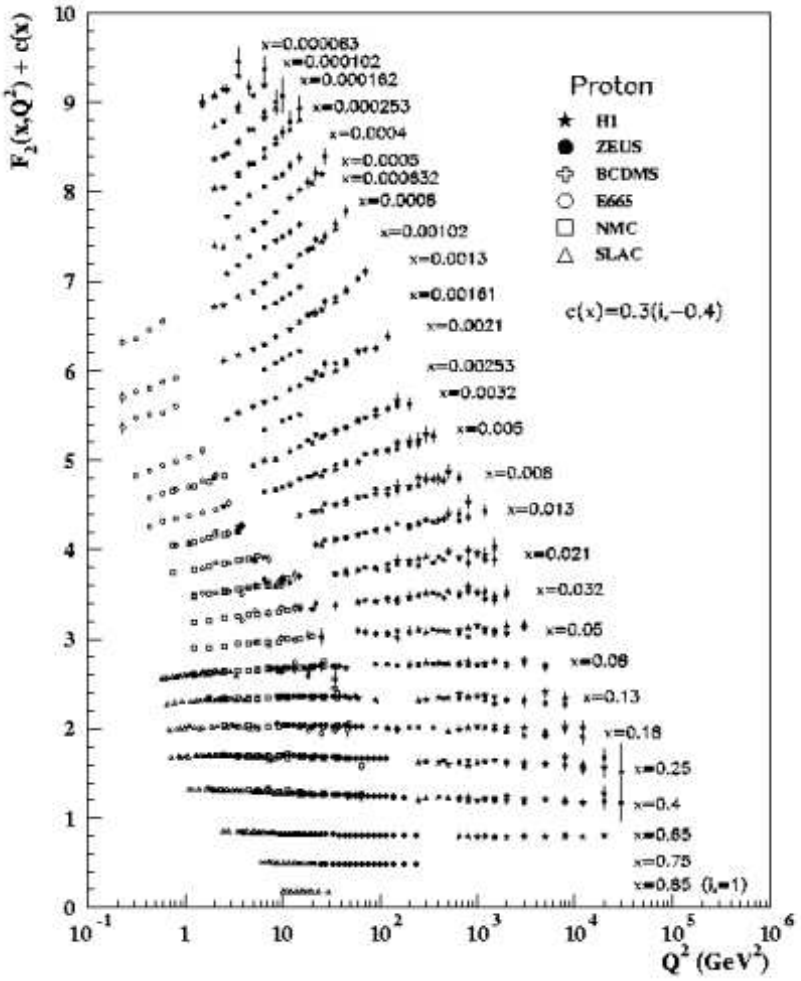

Figure 4.23: Experimental measurements of the proton structure functions. The data are plotted as a function of Q^2 in bins of fixed x [56].

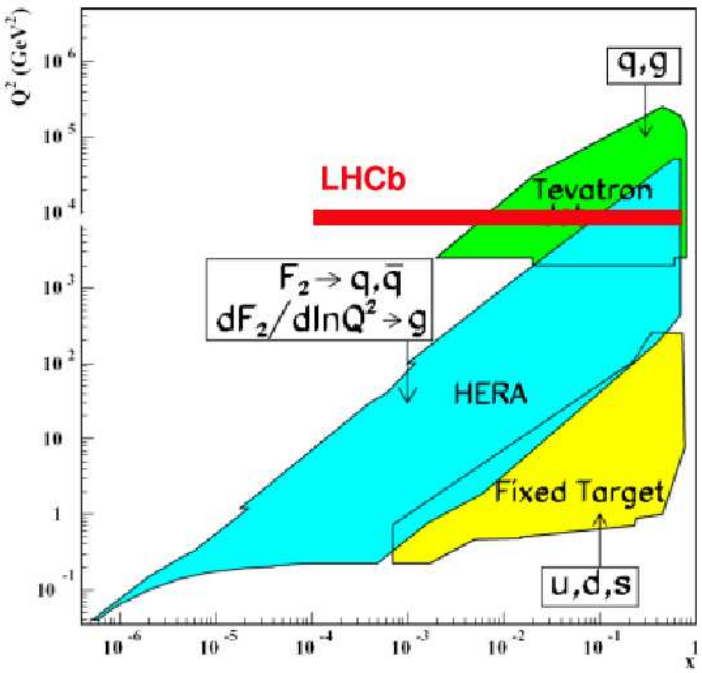

Figure 4.24: Kinematic domains in x and Q^2 probed by various experiments, shown together with the important constraints they make on the various parton distributions. LHCb will be able to explore the red region.

4.12.1 Low Q^2 region

The $Q^2 = M_Z^2$ bond can be removed extending the study to the Drell-Yan process $pp \to \gamma^* \to \mu^+\mu^-$, with an off-shell γ^* mass $< M_Z$. However the background rejection could represent a harder task at low-p_T , where more others physical channels are present, and the selection would not be as clean as for $Z^0 \to \mu^+\mu^-$. Moreover the mass spectrum of the process (see Figure 4.25) shows a very poor statistics in the region between the Z^0 resonance peak and masses as low as $\sim$ 35 GeV/c^2, providing a large uncertainty in the determination of $x_1\, x_2$ product.

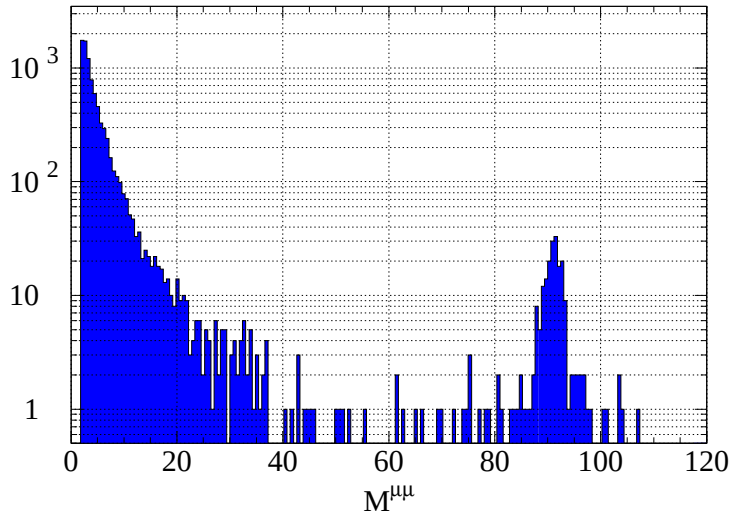

Figure 4.25: Invariant mass of the muons from the process $pp \to \gamma^*/Z^0 \to \mu^+\mu^-$ decaying in the LHCb angular acceptance.

A feasible channel to increase statistics and keep a detectable signal might be represented by $pp \to J/\psi \to \mu^+\mu^-$, allowing the study of the structure functions at $Q^2 \approx 10$ GeV^2 and fractional momenta as low as $x \sim 10^{-6}$, again in an unprobed kinematic region. The performances of LHCb respect to this channel are matter for a study beyond this thesis.

Conclusions

The work of this thesis concerned both the development of a suitable detector for the LHCb Muon system, and the study of physics performance of the LHCb experiment itself.

The Resistive Plate Chambers detectors had been proposed to equip the outermost part of the Muon system, where the radiation flux does not exceed the value of 1 kHz/cm^2 . Several detector prototypes have been built and tested, demonstrating how the LHCb requirements about efficiency, time resolution and spatial resolution were completely fulfilled. The efforts have then focused on the aging properties, to verify whether the requested performances could be maintained for 10 years of operation.

An exhaustive test has been performed at CERN, by means of the Gamma Irradiation Facility, a very intense photon source reproducing the high background environment foreseen at LHCb. The peculiar characteristics presented by RPCs, when exposed to high irradiation have been explained within a simple phenomenological model, which provides as well a practical method to measure the bulk resistivity of the electrodes in a non-destructive way, during the chamber operation. This method was used to monitor the resistivity during almost three years of the test, at the end of which the RPCs have undoubtedly shown to suffer aging effect. The resistivity is in fact increased by two orders of magnitude, from 10^{10} Ωcm, to 10^{12} Ωcm. The most affected property by this change has been, as expected, the rate capability of the detectors, dropped from few kHz/cm^2 to 200 Hz/cm^2 .

The aging effects seem to be predominantly "timing" spontaneous effects, basically independent from the accumulated charge, although probably enhanced by intense irradiation. The responsible has been found in the water content of the phenolic resin composing the electrodes, which decreases as dry gas is fluxed inside the detector, increasing as a consequence the resistivity. The method of flowing humid gas has been tried, and considered not suitable to permanently recover the original performances of the chambers.

The results of the aging test have forced the LHCb collaboration to abandone the RPC as a practicable technology for the Muon system. They have been replaced by safer Multiwire Proportional Chambers.

In the second part of the thesis the process $pp \to \mathrm{Z}^0 \to \mu^+\mu^-$ has been analysed. The theoretical cross-section for this process has recently been calculated at NNLO, and at LHC energy (14 TeV) is foresee to be $\sigma_{\mathrm{Z}\to\mu\mu} \simeq 1.9$ nb, sufficiently high to detect a large number of Z^0 bosons also at LHCb, in spite of the limited angular acceptance and the optimization for the B-physics.

A sample of 50000 events have been generated and the detection efficiency of the apparatus have been extensively simulated, including the reconstruction, the off-line selection and the trigger selection. The annual yield found ($\sim$ 290k) allows to use the channel to perform profitable physics studies.

A precise and extensive calibration of the spectrometer is achievable thanks to the very high momenta reached by the decaying muons, up to 2 TeV/c.

An absolute luminosity measurement can be obtainable in a straightforward way, due to the accuracy of the theoretical value of the cross-section.

Finally an interesting program of hadron physics is possible by studying the pseudorapidity distribution of the muons, which are related to the fractional momenta x of the partons entering the Z^0 production process. The forwardness of LHCb is peculiar to select very high pseudorapidity Z^0 bosons, allowing to extract the proton structure functions $f(x, Q^2)$ at very low x, down to $\sim 10^{-4}$, and high $Q^2 \sim 10^4 \mathrm{GeV}^2$, in a kinematic region not accessible by other experiments.

Bibliography

[1] P. Nason *et al.*, Bottom production. In *Proceedings of the 1999 Workshop on Standard Model Physics at the LHC*, volume CERN 2000–004. CERN, 1999, hep-ph/0003142.

[2] T. Nakada and O. Schneider, LHCb Trigger. In *Proceedings of the 4th International Workshop on B Physics and CP Violation, February 19-23, 001 Ise-Shima (Japan)*. IPHE 2001.

[3] LHCb Collaboration, "LHCb Reoptimized Detector Design and Performance Technical Design Report". CERN/LHCC/2003–030.

[4] LHCb Collaboration, "LHCb VELO Technical Design Report". CERN/LHCC/2001–0011.

[5] LHCb Collaboration, "LHCb Technical Proposal". CERN/LHCC/98–4.

[6] LHCb Collaboration, "LHCb RICH Technical Design Report". CERN/LHCC/2000–0037.

[7] LHCb Collaboration, "LHCb Magnet Technical Design Report". CERN/LHCC/2000–007.

[8] LHCb Collaboration, "LHCb Outer Tracker Technical Design Report". CERN/LHCC/2001–026.

[9] LHCb Collaboration, "LHCb Inner Tracker Technical Design Report". CERN/LHCC/2002–029.

[10] LHCb Collaboration, "LHCb Calorimeters Technical Design Report". CERN/LHCC/2000–036.

[11] LHCb Collaboration, "LHCb Muon System Technical Design Report". CERN/LHCC/2001–010.

[12] LHCb Collaboration, "LHCb Online System Technical Design Report". CERN/LHCC/2001–040.

[13] LHCb Collaboration, "LHCb Trigger System Technical Design Report". CERN/LHCC/2003–031.

[14] LHCb Collaboration, GAUDI Project, http://lhcb-comp.web.cern.ch/lhcb-comp/Frameworks/Gaudi.

[15] LHCb Collaboration, GAUSS – The LHCb Simulation Program, http://lhcb-comp.web.cern.ch/lhcb-comp/Simulation.

[16] S. Agostinelli *et al.*, "GEANT4 - a simulation toolkit", Nucl. Instr. and Meth. in Phys. Res. A506 (2003) 250.

[17] LHCb Collaboration, SICBMC – The LHCb GEANT3 based Simulation Program, http://lhcb-comp.web.cern.ch/lhcb-comp/SICB.

[18] "GEANT – Detector Description and Simulation Tool". CERN Program Library Long Writeup W5013.

[19] T. Sjostrand, "High-energy physics event generation with PYTHIA 5.7 and JETSET 7.4. Comput. Phys. Commun., 82:74-90. 1994

[20] "QQ – The CLEO Event Generator". http://www.lns.cornell.edu/public/CLEO/soft/QQ.

[21] LHCb Collaboration, BOOLE – The LHCb Digitization Program, http://lhcb-comp.web.cern.ch/lhcb-comp/Digitization.

[22] LHCb Collaboration, BRUNEL – The LHCb Reconstruction Program, http://lhcb-comp.web.cern.ch/lhcb-comp/Reconstruction.

[23] LHCb Collaboration, DAVINCI – The LHCb Analysys Program, http://lhcb-comp.web.cern.ch/lhcb-comp/Analysys.

[24] BABAR Collaboration, B. Aubert *et al.*, Phys. Rev. Lett. 89 (2002) 201802; BELLE Collaboration, K. Abe *et al.*, Phys. Rev. D66 (2002) 071102.

[25] M. Battaglia *et al.*, "The CKM matrix and the Unitarity Triangle", hep-ph/0304132.

[26] N. Tuning, "Efficient triggering with the LHCb detector for precise CP measurements", LHCb Note 2003–136 Trig.

[27] The ATLAS Collaboration, "ATLAS Muon Spectrometer Technical Design Report", CERN/LHCC 97–22.

[28] The CMS Collaboration, "CMS Muon Technical Design Report", CERN/LHCC 97–32.

[29] C. Zeitnitz and T.A. Gabriel, The Geant-Calor interface User's Guide (1999), http://www.physik.uni-mainz.de/zeitnitz/gcalor/gcalor.html

[30] I. Azhgirey, I. Kurochkin and V. Talanov, "Development of MARS Code Package for Radiation Problems Solution of Electro-Nuclear Installation Design", in *Proceedings of XV Conference on Charged Particles Accelerators, Protvino, October 22-24 (1996)*

[31] N. Saguidova *et al.* "GCALOR Studies of Backgrond in the LHCb Muon chambers", LHCb Note 1998–059 Expt;
A. Tsaregorodtsev, "Muon System parameterised background – algorithm and implementation", LHCb Note 2000–011 Muon.

[32] P. Colrain, "Upgrade of the Muon System background parameterisation", LHCb Note 2001–029 Muon.

[33] D. Domenici, "Gli RPC per il rivelatore di muoni di LHCb",
University of Rome "Tor Vergata", Graduate Thesis, 2000.

[34] R. Santonico and R. Cardarelli, Nucl. Instr. and Meth. in Phys. Res. A 187 (1981) 377.

[35] R. Cardarelli, A. Di Ciaccio and R. Santonico, Nucl. Instr. and Meth. in Phys. Res. A333 (1993) 399.

[36] C. Bacci *et al.*, Nucl. Instr. and Meth. in Phys. Res. A352 (1995) 552.

[37] R. Cardarelli, V. Makeev, R. Santonico, Nucl. Instr. and Meth. in Phys. Res. A382 (1996) 470.

[38] R. Cardarelli, Scientifica Acta VIII (Univ. Pavia), 3 (1993) 159.

[39] M. Adinolfi *et al.*, Nucl. Instr. and Meth. in Phys. Res. A456 (2000) 95.

[40] R. Arnaldi *et al.*, Nucl. Instr. and Meth. in Phys. Res. A456 (2000) 72.

[41] R. Arnaldi *et al.*, Nucl. Instr. and Meth. in Phys. Res. A456 (2000) 140.

[42] I. Crotty *et al.*, Nucl. Instr. and Meth. in Phys. Res. A346 (1994) 107.

[43] G. Aielli *et al.*, Nucl. Instr. and Meth. in Phys. Res. A508 (2003) 6.

[44] P. Camarri *et al.*, Nucl. Instr. and Meth. in Phys. Res. A414 (1998) 317.

[45] S. Agosteo *et al.*, Nucl. Instr. and Meth. in Phys. Res. A452 (2000) 94.

[46] J. F. Briestmeister, MCNP – A General Monte Carlo N-Particle Transport Code, LA-12625-M Version 4B, Los Alamos, NEw Mexico (1997).

[47] S. De Capua, "Studio di rivelatori di particelle RPC per l'esperimento LHCb", University of Rome "Tor Vergata", Graduate Thesis, 2001.

[48] Korea Atomic Energy Research Institute.
`http://atom.kaeri.re.kr`

[49] M. Adinolfi *et al.*, "Peformance of low-resistivity single and dual-gap RPCs for LHCb", LHCb Note 1999–049 Muon.

[50] G. Carboni *et al.*, Nucl. Instr. and Meth. in Phys. Res. A498 (2003) 135.

[51] A. Bizzeti *et al.*, Nucl. Instr. and Meth. in Phys. Res. A508 (2003) 166.

[52] G. Aielli *et al.*, Nucl. Instr. and Meth. in Phys. Res. A456 (2000) 82.

[53] G. Carboni *et al.*, Nucl. Phys. B (Proc. Suppl.) 125 (2003) 374.

[54] P. D. B. Collins & A. D. Martin, "Hadron Interactions" ADAM HILGER LTD, BRISTOL.

[55] T. Dorigo, "W and Z Cross Sections at the Tevatron", hep-ex/0306008 (2003).

[56] K. Hagiwara *et al.*, Phys. Rev. D66 (2002) 010001. `http://pdg.lbl.gov`

[57] V. A. Khoze *et al.*, Eur. Phys. J. C19 (2001) 313.

[58] The ATLAS Collaboration, "ATLAS High-Level Trigger, Data Acquisition and Controls Technical Design Report", CERN/LHCC 2003–022.

[59] TOTEM Collaboration, Technical Proposal, CERN/LHCC/99–7.

[60] A. Maslennikov, "Photon Physics in Novosibirsk", Workshop on Photon Interactions and Photon Structure, Lund (1998) 347.

[61] K. Piotrzkowski, ATLAS Physics Note ATL-PHYS-96-077 (1996).

[62] A. D. Martin, R. G. Roberts, W. J. Stirling and R. S. Thorne, Eur. Phys. J. C18 (2000) 117.

[63] W. L. van Neerven and A. Vogt, Nucl. Phys. B382 (2000) 11.

[64] A. D. Martin, R. G. Roberts, W. J. Stirling and R. S. Thorne, Eur. Phys. J. C14 (2000) 133.

[65] H. Plothow-Besch, PDFLIB: Proton, Pion and Photon Parton Density Functions, Parton Density Functions of the Nucleus and α_s Calculations, User's Manual - Version 8.04, W5051 PDFLIB, 2000.04.17, CERN_PPE.

[66] See for example P. N. Harriman *et al.*, Phys. Rev. D42 (1990) 798 and A. D. Martin *et al.*, Phys. Rev. D50 (1994) 6734.

[67] CTEQ Collaboration, Phys. Rev. D55 (1997) 1280.

[68] `http://plus.web.cern.ch/plus/` `http://batch.web.cern.ch/batch/`

[69] The Aleph Collaboration, "Measurement of the Z Resonance Parameters at LEP", Eur. Phys. J. C14 (2000) 1.